LUDWIG-MAXIMILIANS-UNIVERSITÄT MÜNCHEN

FAKULTÄT FÜR GEOWISSENSCHAFTEN

In Kooperation mit dem Deutschen Zentrum für Luft- und Raumfahrt in Oberpfaffenhofen

MASTERARBEIT
Umweltsysteme und Nachhaltigkeit
Monitoring, Modellierung und Management

Wissenschaftliche Arbeit zur Erlangung des akademischen Grades Master of Science

eingereicht am Department für Geographie

Derivation of urban mass concentrations from TanDEM-X data for the analysis of polycentric urban structures in the USA and Germany

Ableitung von Baumassenkonzentrationen aus TanDEM-X Daten für die Analyse polyzentrischer Stadtstrukturen in den USA und Deutschland

Verfasserin:
Marlene Kühnl
marlene.kuehnl@gmx.de
Matrikelnummer: 11624582

Betreuer LMU:
Prof. Dr. Wolfram Mauser
PD Dr. Tobias Benedikt Hank
Betreuer DLR:
Dr. Hannes Taubenböck
Dipl.-Ing. Ines Standfuß

Abgabefrist: 19.06.2019

Acknowledgement

In the winter term 2015/2016 I wrote my Bachelor thesis in the team 'City and Society' of the 'Georisks and Civil Security' department at the *Deutsches Fernerkundungsdatenzentrum* (DFD) of the German Aerospace Center in Oberpfaffenhofen. The experience of spending some time in this research institution has had a lasting influence on my academic career. My work at this place and the people I met, have led me to the decision to select my postgraduate studies according to remote sensing subjects as well as possibilities to expand my methodological skills in this area. Now I am at the end of my Master studies and I have returned to the place that has shaped me in my fascination and enthusiasm for remote sensing to write my thesis. Before addressing the actual topic, I would like to express my gratitude to the following persons.

I want to thank Dr. Hannes Taubenböck, leader of the team 'City and Society', and Dipl.-Ing. Ines Standfuß, for welcoming me with open arms. During the six-month processing period, they were always there to support and supervise me. Without their help I would not have been able to make this journey.

Furthermore, I want to thank Dr. Tobias Hank, habilitated lecturer at the Ludwig-Maximilians-University Munich and supervisor of my thesis, with whom I share the interest for the topic of this thesis. He supported the research subject from the very first moment and always took his time to reflect my work critically.

In addition, I want to thank Dr. Wolfram Mauser. During his lectures he frequently illustrated the need for a combination of social sciences and remote sensing. His words also encouraged me in my decision to write my master thesis at the German Aerospace Center in the team 'City and Society'.

Finally, I want to thank Thomas Esch for providing me with the Global Urban Footprint data. Only by the free provision of the data set I was able to accomplish this thesis.

Abstract

The urban areas around the world are growing and constantly changing. One of the developments that can be observed alongside, especially in the Global North, is the formation of several densification patterns, so-called (sub-)centers, in addition to the traditional center. This phenomenon, known under the scientific term *polycentricity*, has so far mainly been analysed based on socioeconomic data on employees, population or human activity data, to name a few. These approaches, however, are reaching their limits. Due to data heterogeneity, limited data availability and diverse methodological strategies to identify center structures, comparisons between cities or regions are difficult. Since remote sensing enables to compute the urban morphology on large scale, it has the potential to support the social sciences.

Against this background, within this thesis I used remotely sensed data to calculate urban mass concentrations, defined as volume per processing unit, in four German cities and four cities in the USA. The outcome is a morphological 3D characterization of the urban structure. In the scope of this thesis the approach used to generate these urban mass concentrations is applied for the first time to cities in the USA. Originating from the results, in a next step, high urban mass concentrations interpreted as (sub-)centers are identified by applying a threshold method. Based on the identified (sub-)centers a polycentricity analysis is finally carried out to compare the distribution of (sub-)centers within Germany and the USA as well as between Germany and the USA.

Concluding, the thesis investigates the phenomenon of polycentricity from a morphological perspective in order to contribute to the understanding of the changes happening in today's urban environments of the Global North. At the same time, it is a contribution to the further development of polycentricity analyses.

Table of contents

List of Figures

List of Tables

List of Equations

List of Abbreviations

ABF	Austin Building Footprint
BE	Bare Earth
BF	Building Footprint
CBD	Central Business District
DEM	Digital Elevation Model
DFG	Deutsche Forschungsgemeinschaft
DLR	Deutsches Zentrum für Luft- und Raumfahrt
DSM	Digital Surface Model
DTM	Digital Elevation Model
EO	Earth Observation
ESA	European Space Agency
GDP	Gross Domestic Product
GIS	Geographic Information System
GUF	Global Urban Footprint
hUMC	High urban mass concentration
INSPIRE	Infrastructure for Spatial Information in the European Community
LoD1	Level of Detail 1
LPI	Largest patch index
LWR	Locally-weighted regression
MBF	Microsoft Building Footprint
MF	Morphological Filter
NDVI	Normalized Different Vegetation Index
NIR	Near infrared
OBIA	Object-based image analysis
OBJ	Nonground object
PBF	Portland Building Footprint

PHBF	Philadelphia Building Footprint
PMF	Progressive Morphological Filter
pnDSM	Preliminary normalized Digital Surface Model
potOBJ	Potential nonground object
RPMF-SOBV	Selective object-based & region-growing-based PMF
SAR	Synthetic Aperture Radar
SD	Standard deviation
SE	Structuring element
SOBV	Selective object-based voting
SWIR	Short wave infrared
TDX	TanDEM-X
TSX	TerraSAR-X
UA	Urban Area
UMC	Urban mass concentration
UMZ	Urban Morphological Zone
UCP	Urban containment policies

1 Introduction

Urban settlement structures in the Global North are undergoing an evolution from formerly ‚mono-centered' to ‚poly-centered' cities with several densification patterns in addition to the Central Business District (CBD; e.g. Greene 1980, 29; Vasanen 2012, 3628; McDonald & Prather 1994, 201; Anas et al. 1998, 1427; Krehl 2018, 79). The monocentric model pictures a continuing decrease of density away from the center. But this well-known trend doesn't seem to reflect today's urban structure properly any more (Taubenböck et al. 2017aa, 42). Dispersion and sprawl of population and activities have led to fundamental changes in the last two centuries and consequently to a modification of the traditional theoretic monocentric city model. But the transition seen in today's urban structure can also not clearly assigned only to these two development patterns alone (Krehl 2018, 79f.; Zhong et al. 2015, 438; Riguelle et al. 2007, 194). The shift is rather a complete rearrangement of urban spatial structure existing of deconcentration processes - dispersion and sprawl - on the one hand and concentration processes - subcenter formation and reurbanization - on the other hand (Krehl 2018, 80). This overlap then leads to the spatial configuration of 'polycentricity' with a diminishing regional primacy of the CBD and several co-existing subcenters (Taubenböck et al. 2017a, 42).

One central element used in literature for the identification and description of CBDs and (sub-)centers is employment densification, which is in mutual influence with the density of built structures. Morphological compactness is a precondition for spatial proximity of individuals and actors such as residents, employees or entrepreneurs and this gathering on the other hand has an impact on economic and social interactions like face to face contacts or sharing of resources (Krehl 2018, 80; Krehl et al. 2016a, 1; Agarwal et al. 2012, 435). Therefore, polycentricity is assessable by means of different spatial and socioeconomic indicators. A common approach is the use of (socio-) economic variables such as employee-, population- or firm-counts to identify centers of densification of those quantities in the urban area (e.g. Greene 1980, McDonald 1987, Giuliano & Small 1991, Roca Cladera 2009, Agarwal et al. 2012). Besides, there are also attempts to use the built environment as an indicator for (sub-)centers (e.g. Schneider et al. 2015; Taubenböck et al. 2013). Two-dimensional approaches employ the build-up area (e.g. Yue et al. 2010) whereas three-dimensional efforts include the build-up volume as well to detect center structures (e.g. Wurm et al. 2014; Geiß et al. 2017). In addition, polycentricity was examined in the context of urban geography and planning with studies mainly focused on North America (Krehl 2018, 80). However, polycentric development is not limited to that geographic region but can also be observed in Europe (Taubenböck et al. 2017a, 42; Garcia-López & Muñiz 2010, 3051; Riguelle et al. 2007, 211).

1.1 Scientific discourse of polycentricity

Although 'polycentric development' has been a much discussed topic in the academic and political literature for the last two decades, 'polycentricity' itself still remains a 'fuzzy' concept (Burger & Meijers 2011, 1127). In general, it can be understood as "*phenomenon or process which possesses two or more alternative meanings and thus cannot be reliably identified or applied by different readers or scholars*" (Markusen 1999, 870). But this results in a fundamental problem. Whereupon should a well-founded polycentricity analysis be based on, if the theoretical foundation depends on the researcher's perspective (Vasanen 2012, 3628, Riguelle et al. 2007, 195)?

From a morphological point of view polycentricity refers to the distribution of objects (here buildings) within a given area. If there is a significant spatial horizontal and vertical densification of those objects in comparison to their surroundings, they get treated as centers (Taubenböck et al. 2017a, 43). Therefore, a polycentric city is an urban region with several compression clusters of buildings (Kloosterman & Lambregts 2001, 718f). The morphology describes the size and spatial distribution of those clusters. The functional dimension in contrast deals with connections between them like commuting flows or economic and social network linkages (Zhong et al. 2015, 438). Hence, functional polycentricity can be seen as network of places (Taubenböck et al. 2017a, 43), whose individual connections contribute to the entire polycentric urban system (Vasanen 2012, 3628f.).

The linkages, regardless of whether they are morphological or functional, can occur between subcenters or several cities and they may be a major component of the wellbeing of the urban system as a whole (Burger & Meijers 2011, 1128). Therefore, polycentricity can appear at different dimensions and subsequently is of multi-scalar nature. The first one is called 'intra-urban' polycentricity dealing with centers within individual cities like Los Angeles or London. Another option is the 'inter-urban' pattern of clustering, examples are urban hubs with larger regional spatial entities as the Dutch Randstad or the Rhine-Main region in Germany (for an overview of inter-urban polycentric development in Europe see Hall & Pain 2006; Krehl et al. 2016b, 3f.; Riguelle et al. 2007, 195). Moreover, exists the 'inter-regional' or 'inter-national' interdependency among urban nodes, an example is the so called 'Pentagon', used by the EU to identify a polycentric region that includes Paris, Milan, Hamburg, Munich and London (Veneri & Burgalassi 2012, 1019f.)

The confusion is exacerbated by the chosen reference parameter (e.g. employment or population) and its discrimination value differentiating between (sub-)centers and surroundings. These are determined by the scientist and thus cannot be regarded as objective. Moreover, the identification of polycentricity is highly scale-dependent in the context of the size of the research area. A city

which may indicate a polycentric development on one scale may show monocentrism when evaluated at another, even when the same value is applied to separate (sub-)centers from other city structures (Vasanen 2012, 3628; Zhong et al. 2015, 438f.).
These different characteristics make it possible to determine polycentric development as a spatial process, but a quantitative measurement still remains inconsistent. Even after many years of research, there are no exact values indicating when a city is polycentric or only shows tendencies towards it.

Historically, the theory of polycentricity grew out of a monocentric city model. The latter finds its origin in the work of Alonso (1964), Mills (1967) and Muth (1969), whom founded the scientific field of urban economics. They have been the first to combine city transport, land use and population issues under the term 'monocentricity'. This relatively simple model claims that production and consumption only take place in the dense core city (CBD; Duranton & Puga 2015, 472f. & 484) surrounded by a less dense hinterland. The highest land value occurs in the CBD and originating from it results a concentric distance-based negative rent gradient (Taubenböck et al. 2017a, 43; Anas & Kim 1999, 251). This primacy occurs due to so called agglomeration economies, advantages because of an enormous concentration of values, infrastructure, employment and money flows, which give an explanation why cities form in the first place (Taubenböck et al. 2013, 386; Duranton & Puga 2014, 807ff.). Over time costs for housing and commuting rise, the agglomeration economies turn into diseconomies and people tend to migrate into the less dense hinterland (Duranton & Puga 2014, 807ff.). This migration will either lead to a densified extended core or to a formation of new centers in the area surrounding the CBD. In this case, a polycentric development has started (Taubenböck et al. 2017a, 43).
In addition, however, it must also be noted that polycentric development can also be tracked back to urban planning events. Since the 1960s many cities have adopted urban containment policies (UCPs) to manage urban growth pressures and urban sprawl as well as to protect open space (Siedentop et al. 2016, 71; Begngston & Youn 2006, 1f.; Anthony 2004, 378). Research on this topic has already been carried out in America, Europe and Asia (e.g. Siedentop et al. 2016; Landis 2006; Bengston & Youn 2006, Dieleman et al. 1999) and some results show, that state-wide management strategies can promote a polycentric spatial urban structure while preventing urban sprawl (Woo & Guldman 2014, 6). UCPs such as growth boundaries or greenbelts (for a deeper definition and explanation see e.g. Siedentop et al. 2016 or Woo & Guldman 2014) often result in a spatial concentration of development in CBDs and surrounding higher density patterns (Siedentop et al. 2016, 72.).
Taking these approaches into account, it can be said, that polycentricity refers to a spatial

configuration between monocentrism and urban sprawl. It can develop by reasons of agglomeration economies turning into diseconomies or as physical manifestation of UCPs. As a consequence, polycentricity must be seen as both. It is the historical legacy of urban planning events as well as the outcome of economic migration movements away from the CBD (Taubenböck et al. 2017a, 43).

As already briefly mentioned above, for the identification and examination of morphological polycentricity traditional approaches mostly use employees as parameter of interest (e.g. Roca Cladera 2009, McDonald 1987, Gordon et al. 1986). These are linked to agglomeration economies (Taubenböck et al. 2017a, 43), as it is assumed that the CBD holds the highest density of employment due to the described advantages (Krehl 2018, 83). In the wake of emerging benefits in the forming centers in the hinterland like less rent/traffic and at the same time density of economics as well as face-to-face contacts, which lets them become alternatives to the CBD (Riguelle et al. 2007, 195), employees seem the most obvious variable to analyze polycentricity (Taubenböck et al. 2017a, 43). Meanwhile the relationship between physical shapes and socioeconomic activities is better understood and therefore morphological characteristics like built-up height and density gain importance. As a result, morphological variables are now included in addition to socioeconomic parameters, or the latter are even omitted and analyses are only carried out using the physical structure (e.g. Schneider et al. 2015, Taubenböck et al. 2013, Yue et al. 2010; Taubenböck et al. 2017a, 43; Krehl 2018, 1).

In the course of attempting to find a definition, 'polycentricity' is seen as a number of co-existing centers in one urban region (Klosterman & Lambregts 2001, 718f.) developing through a spatial process where socioeconomic functions of traditional CBDs diffuse from one major center to an undefined number of subcenters (Zhong et al. 2015, 438f.). Through influences on land values, housing prices and travel patterns, this evolving spatial structure has a large influence on people's daily life, the economic growth, the social equity and the sustainable urban development (Zhong et al. 2015, 438; McDonald 1987, 242). For the implementation of adequate planning strategies, it is therefore a crucial task to understand this polycentric evolution in urban organization forms. Thus, it is not surprising that in recent years the quantitative characterization of urban structure has gained much attention in a wide range of scientific fields like e.g. urban geography, urban economics or spatial planning (Zhong et al. 2015, 438).

1.2 State of research

To exemplify how polycentricity is investigated, the following explanations display how morphological urban characterization and/or subcenter detection has been addressed in the literature so far. Starting with more conventional approaches, the main focus is on newer analyses, which tend to use the physical appearance as parameter of investigation. In order to also show the differences in America and Europe, scientific findings in the field of spatial urban development are outlined later on.

1.2.1 Means of subcenter identification and the role of remote sensing in urban investigation

A first step in evaluating the effects of subcenters on urban spatial structures is their identification (McMillen 2001, 448). Throughout the last decades a broad spectrum of different methodologies, using diverse parameters of interest, to identify the local spatial densification patterns has evolved in the research community (Krehl 2018, 80).

Morphological polycentricity is related to the spatial distribution of economic activity. Therefore, as briefly described above, employment is the most frequently used variable to identify center structures. But also, population or firm counts have been used in the past (e.g. Garcia-López & Muñiz 2010; Riguelle et al. 2007; Redfearn 2007; Craig & Ng 2000; McDonald 1987).

In order to measure the degree of functional polycentricity the research community uses mostly flow data. Hence, commuting or shopping trips are deployed as analyzing parameters (e.g. Burger & Meijers 2012; Veneri & Burgalassi 2012, 1022f.). However, this data is not sufficient to capture the actual use of urban space. Employees or students working from home and not in offices or libraries are not recorded at all amongst others. Therefore, newer approaches also include human activity data (Zhong et al. 2015, 439). Roth et al. (2011) for example use the electronical subway ticket system in London, which stores the individual person's movements, to identify polycentricity in the city (Roth et al. 2011, 1) or Zhong et al. (2015), whom use travel survey data with direct information on human activities to quantify the centrality of a given location (Zhong et al. 2015, 440f.).

In summary, there is not a typical parameter with which polycentricity, whether of morphological or functional nature, can be quantitatively investigated – different approaches use different parameters. In addition, the data used are not collected by applying one universal method and no area-wide availability is guaranteed. Therefore, the objective of comparability is already fundamentally undermined. In terms of morphological polycentricity for example, census data, where the survey was subject to the individual countries, are mostly deployed (e.g. Lv et al. 2017; Redfearn 2007; Hall & Pain 2006). Moreover, the data basis consists frequently only of

aggregated numbers added up to investigation units, rather than actual truths (e.g. Giuliano & Small 1991). Since the location of these units is also influenced by the data collection method, they differ from city to city and also over time. This influences the number of identified (sub-)centers considerably (e.g. Redfearn 2007; Lee 2007; Giuliano & Small 1991).

Similarly, the examination on different analysis schemes contributes to the fuzziness of polycentricity. Already mentioned in the previous section, the range goes from one individual city to trans-national urban connections, whereby polycentricity is always understood to mean something different in context of the analysis entity (e.g. Garcia-López & Muñiz 2010; Hall & Pain 2006; Kloosterman & Lambregts 2001; Waterhout et al. 2005).

The application of various methods for the investigation of polycentricity must also be considered. The approaches range from comparatively simple techniques like density maps or gradients to discover employment densifications (e.g. Gordon et al. 1986, Anas & Kim 1996, Kim 2007; Krehl 2018, 80) to cutoff ('threshold') methods, where *a priori* defined density values differentiate (sub-)centers from their surroundings (e.g. Green 1980, Giuliano & Small 1991, Anderson & Bogart 2001, Gaschet 2002, García-López & Muñiz 2007, Kim et al. 2014; Krehl 2018, 82). Additionally, advanced analytical procedures like exploratory methods working with indices (e.g. Riguelle et al. 2007, Guillain & Le Gallo 2010, Krehl 2015a; Krehl 2018, 82; Riguelle et al. 2007, 199), regression-based parametric analyses (e.g. McDonald 1987, McDonald & McMillen 1990, McDonald & Prather 1994, Roca Cladera et al. 2009) and non-parametric locally-weighted regression concepts (LWR) are often deployed (e.g. McMillen 2001, Craig & Ng 2001, Readfearn 2007, Krehl 2018; for a good summarized overview, see Roca Cladera et al. 2009). This demonstrates how diverse the approaches in polycentricity analysis are and how this feature indicates how difficult it is to compare the results. Even detected (sub-)centers within one area of investigation, which were calculated with the same approach and parameter, vary in number, size and location within the study region (Taubenböck et al. 2017a, 44; Agarwal et al. 2012, 441). This is also due to the fact that the data basis, analysis unit and the underlying definition of a center - 'When is a center a center?' - have a considerable influence on the outcome. Agarwal et al. (2012) exemplify this for the city of Los Angeles, USA. Through the comparison of six studies using either different threshold approaches (4) or LWR (2), they address this problem scientifically. Giuliano et al. (2007) are with 13 identified centers in 1990 at the lowest end of the spectrum. In contrast Forestall and Greene (1997) score the highest number by identifying 120 centers for the same year, while the remaining results of the compared studies are somewhere in between. This exemplifies that the outcomes vary significantly depending on the method used and the discrimination value between (sub-)centers and surroundings (Agarwal et al. 2012, 441). All in all there is a unity throughout the research community about the existence of polycentricity. But at

the same time the fuzziness of the concept means that traditional methods and parameters discussed above are no longer satisfying for comparable research approaches (Taubenböck et al. 2017a, 44; Maktav et al. 2005, 655). In order to attain comparability between different regions, reproductivity and the ability to investigate large areas instead of being restricted by data availability and its units of analysis the scientific community has to refer to other techniques (Maktav et al.2005, 655) and parameters of investigation.

Earth Observation (EO) as well as Geographic Information Systems (GIS) can help to solve problems encountered with conventional methods (Maktav et al. 2005, 655). Even though remotely sensed data cannot completely solve the mathematical problems, they form a uniform, timely and spatially continuous data basis (Geiß et al. 2017, 1).

With the advent of third generation commercial satellite programs with very high resolution such as IKONOS (4m resolution), Quickbird (2.4m resolution) or WorldView (1.85m resolution) - multispectral data (ca. 5 to 10 bands with approximately 70-400nm each) - Remote Sensing applications are now suitable for urban analyses as well (Geiß et al.2017, 1; Klotz et al. 2015, 35; Shafri et al. 2012, 1557; Ehlers 2006, 357f.; Maktav et al. 2005, 656). Besides, also hyperspectral data (100 to 200 bands with approximately 5-10nm each) have a great potential to contribute to the analysis of the urban environment, although the applications are still rare (e.g. Heiden et al. 2012; Fauvel et al. 2007). The data is acquired mostly exclusively from airborne platforms and the best results for urban applications such as roof type mapping or urban heat islands are given in combination with different sensors like Light Detection and Ranging (LiDAR; Shafri et al. 2012, 1557ff.). However, the future spaceborne hyperspectral satellite mission EnMAP (launch planned for 2020; DLR 2019) is expected, although limited to a resolution of 30m, to advance urban analysis (Heldens et al. 2011 1831ff.). First researches have already been carried out with simulated EnMap recordings (e.g. Rosentreter et al. 2017).

In general, currently available geometric resolutions enable to distinguish comparable small objects like buildings. The radiometric resolution further allows to discriminate the urban areas thematically and the temporal resolution to detect their changes throughout time (Maktav et al. 2005, 656). But it still remains a complex challenge due to the different materials present in urban features and its variety in size and shape, which can lead to several forms within one pixel (Schneider et al. 2015, 48). Already common applications such as the derivation of spatial extent and location of urban areas, land use classifications and their spatial distribution, detection of infrastructure networks and the monitoring of change in land cover and use over time predominantly represent the cityscape in horizontal-space and over time (Klotz et al. 2015, 34.; De Paul 2007, 2268).

But only by including the third dimension - the height - a far-reaching physiognomic analysis can

be achieved. The combination of building heights, derived for example from Digital Surface Models (DSM; e.g. Wurm et al. 2014), with an extensive landcover classification allows to investigate the structural framework of urban space in addition to a detailed characterization in thematic classes (Klotz et al. 2015, 34ff.). Possible applications are vulnerability assessments (e.g. Geiß et al. 2015a) or a detailed building topology through different spectral signatures of the roof materials (e.g. Heiden et al. 2007). Furthermore, an interdisciplinary intersection with socioeconomic or demographic data allows recognizing spatial patterns of distribution of e.g. population or employees (e.g. Krehl 2015b).

Urban Remote Sensing is therefore already being used in a wide variety of areas, including the analysis of densification patterns. Compared to traditional methods for the detection of (sub-)centers to analyze polycentricity, the use of remotely sensed data in this research interest is a relatively new concept and only a few approaches, as the following will show, exist so far. Schneider et al. (2015) for example use a combined approach based on satellite (land cover change maps) and socioeconomic (total population) data. They assess e.g. the changes visible during different periods in the amount of built-up land and the ratio of urban land to population. Their study shows a transition from a monocentric to polycentric urban form in their study region in Western China (Schneider et al. 2015, 47ff.). A similar approach has been conducted by Yue et al. (2010), who also implemented an urban-rural gradient analysis to understand the development of polycentricity over time in their study area Hangzhou in China (Yue et al. 2010, 565ff.). A further example, exploiting large-area intra-polycentric structures, is deducted by Taubenböck et al. (2017b). Through the use of EO data they identified so-called 'urban nodes' in Europe as well as their degree of connectivity (Taubenböck et al. 2017b, 1 & 10ff.).

The described examples display typical two-dimensional as well as mostly regional attempts. Moreover, socioeconomic data is often part of the analyses. Taubenböck et al. (2017a) see the reason for this development in the elusive conceptual differentiation of built densities as well as in a lack of very high resolution data with the needed spatial detail (Taubenböck et al. 2017a, 44). Availability, data costs and processing requirements of very high resolution images prevent spatially continuous and consistent approaches for very large areas (Geiß et al. 2017, 1). But that is exactly what a comprehensive analysis of the morphology of urban settlements and following derivation of polycentric structures would require for better understanding the 'polycentricity' construct, to establish comparability as well as to be reproducable and thus draw wide-ranging conclusions. Especially in areas where necessary statistics on employment are not available or only partially, the solely use of Remote Sensing data can serve as an alternative indicator for the analysis of polycentric development (Yue et al. 2010, 575).

To overcome the abovementioned constraints, newer approaches to characterize urban structures

morphologically build a trade-off between quite high spatial resolution and large-area coverage and also include the third dimension to achieve the goal of a far-reaching physiognomic analysis. Examples in European cities have been performed by Taubenböck et al. (2013), Wurm et al. (2014) and Geiß et al. (2017). Their studies overcome the limitations by using Cartosat-1 and TanDEM-X DSMs, which build a trade-off between large-scale analysis and very high spatial resolution. Comparable less resolution enables them to cover a larger area. The inclusion of the height allows them to create a three-dimensional classification in urban mass concentrations (UMCs). They are defined as accumulated built-up volume (m3) per reference unit (m^2) (Geiß et al. 2017, 1ff.; Wurm et al.2014, 4139; Taubenböck et al. 2013, 387ff.). Beyond that, the newest attempt from Geiß et al. (2017) does not include prior knowledge, which makes a more objective statistical description possible, as they make sure that the characterization is not based on previous accepted classes such as e.g. residents, firms, etc. (Geiß et al. 2017, 1). Using the resulting consistent and large area 3D building models with high geometrical accuracies from Wurm et al. (2014), Taubenböck et al. (2017a) carry out the latest approach to polycentric analysis. They apply different threshold approaches and identify (sub-)centers as high urban mass concentrations (hUMC) in four German city regions. Therefore, it is the first approach using solely built-up volume as object of investigation instead of socioeconomic parameters like employees (Taubenböck et al. 2017a, 44). They try to evaluate a suitable method in order to identify (sub-)centers and therefore analyze polycentricity more objectively. They can prove that UMCs are a good approximation for economic activity in urban regions, but the question of comparability and reproducibility between and in different regions still remains (Taubenböck et al. 2017a, 44 & 47ff.; Krehl et al. 2016a, 16f.).

1.2.2 Urban configurations in Germany and the USA

"With its limited reach, it is fair to say that US urban policy cannot even faintly 'Europeanize' the shape of American cities" (Nivola 1999, 52).

Although this quotation suggests a different shape for European and North-American cities, previous research has also revealed common developments such as polycentricity (see section 1.2.1). It should also be noted that form is not only influenced by political planning policies, of course. Historical situations and land use patterns amongst others are also reflected in today's settlement structures (Krehl 2018, 83).

Gordon & Cox (2012) conducted a comparison between cities in Western Europe and the United States by examining different variables. They found both similarities as well as differences. But especially for the development of city structures related trends seem to occur (keyword 'urban sprawl'; Gordon & Cox 2012, 7ff.). Richardson & Bae (2016) and Bruegmann (2005) as well

come to similar conclusions. They state that cities and suburbs in Western Europe and the US show an increasing convergence in their development since the 1970s (Richardson & Bae 2016, 1; Bruegmann 2005, 92). Although various initial conditions such as amount of space for settlement expansion have led to more compact and dense urban environments in Germany compared to US metro regions, resulting in lower average densities, the cities seem to be embracing the same development trends (Krehl 2018, 84; Nivola 1998, 18). This can be partly explained by a contrary movement. An increasing number of US cities are becoming comparably denser, while in Europe dispersion is continuing (Bruegmann 2005, 92). But even though the polycentric development trend is present in both (see e.g. Knapp & Volgmann 2011, Roca Cladera et al. 2009), the urban spatial structure in Germany (or in general Europe) and North-America is not the same. Centers and subcenters differ in terms of size and location, their functional meaning as well as their significance for the urban spatial network, even within countries (see e.g. Krehl 2018, Krehl 2015a, Shearmur & Coffey 2002; Krehl 2018, 83).

To this day there are only a few studies that compare polycentricity in different regions. If they do, then they exist within countries with a large surface area or within a nation (e.g. Shearmur & Coffey 2002) and not between area-poor and area-rich countries. Krehl (2018) makes a first attempt to compare polycentricity in Germany with cities in the USA. The data for the latter is calculated via LWR, while North-America's is literature-based and originates from previous studies. She finds out what is already described above: (sub-)centers exist, but there is a spatial difference between the dense urban structures of both countries. In her work Krehl (2018) discusses several reasons for this result but argues that they are still hypothetical and further in-depth research need to be done to make reliable statements (Krehl 2018, 84 & 99ff.).

1.3 Aim of work

Be it the definition of the concept, possible parameters of investigation as well as the diverse methods to identify (sub-)centers or the pursuit of using region-independent data, the previous sections have shown that a lot of challenges remain in polycentric research. Especially the use of remotely sensed data in the context of urban structural characterization and subsequent polycentricity analysis is a quite new concept offering a lot of room for further investigations (see 1.2.1). There is also still a major gap in the research of polycentricity in the transcontinental context in order to compare polycentric developments of the most diverse regions. So far only one study has been carried out in this relation (see 1.2.2).

Against this background, a large scale processing and validation of UMCs (urban mass concentrations) as well as a subsequent analysis of polycentricity of different urban areas in North America (USA) and Europe (Germany) is performed in the scope of this thesis.

In a first step, a *generation of UMCs* in the study regions is carried out. The approach relies on the methodology developed by Geiß et al. (2015c, 2017) for large-scale physical classification of urban regions in terms of building density and height, based on TanDEM-X and Sentinel-2 satellite data. This method has already been successfully applied and validated for selected German metro regions (Geiß et al. 2017, 1ff.). In the context of this thesis, the method is implemented for the first time to urban structures in the USA to review cross-continental transferability.

Based on the assumption that the UMCs are correct for the German cities (see Geiß et al. 2017), a *validation* exclusively for the UMCs in the USA follows. For this purpose, existing 3D models of the investigated North-American urban regions are used. Thus, the resulting morphological classifications of step one can be compared with high detailed building information to validate the outcome.

In the third part of the study follows a *polycentricity analysis* based on the approach developed by Taubenböck et al. (2017a). The UMCs serve as input, from which 3D city models can be created. A threshold analysis is then used to identify (sub-)centers. Finally, the results of the identification of the individual urban regions in America and Germany are compared in order to present morphological polycentricity transcontinental.

The aim of this thesis is to further investigate the potential of the morphological classification developed by Geiß et al. (2017) for the analysis of morphological polycentricity. Furthermore, the thesis seeks to identify differences and similarities in urban morphologies with particular focus on urban centers in Germany and the USA. The corresponding research questions that are going to be answered in the scope of this thesis are listed in Table 1.

The remainder of this thesis is organized as follows. Section 2 begins with the presentation of the data used for the morphological characterization and the following validation of the resulting UMC classification. Subsequently the study regions are described in detail by categorizing them geographically and presenting the criteria for their selection. The third part of this section gives a detailed description of the methods used for the generation of the UMCs, the validation and the following polycentricity analysis. The results are presented in chapter 3 before they get interpreted and critically discussed in section 4. Chapter 5 completes the thesis with answering the research questions and outlook on needed future work.

Table 1: Summary of the research questions that are going to be answered in the scope of the thesis. They are listed according to their affiliation to the individual sections of the study (own Table).

STUDY SECTION	*RESEARCH QUESTIONS*
MORPHOLOGICAL CHARACTERIZATION	Do the UMCs derived from TanDEM-X data by using the approach developed by Geiß et al. (2015c, 2017) render the urban morphology of cities in the USA?
POLYCENTRICITY ANALYSIS	Which differences and similarities in urban center distributions based on UMCs can be found between US and German cities?
POLYCENTRICITY ANALYSIS	Can the assumptions about similar development of urban structures in US and German cities (see chapter 1.2.2) be confirmed?

2 Material and Methods

In this part of the work, the areas of investigation (2.1) and the data used (2.2) are presented. Subsequently, the methodical procedure (2.3) of the morphological characterization, the validation of the UMC classification and the polycentricity analysis will be explained in detail.

2.1 Study regions

This thesis is a contribution to the project *'Where are the jobs? Stadtregionale Zentrenstrukturen im internationalen Vergleich'* (engl. 'Where are the jobs? International comparison of urban-regional center structures') of the *Deutsche Forschungsgemeinschaft* (DFG), which has been funded since 2018 (for more information see DFG 2019). The selection of the cities to be examined in the context of this thesis was made by the project committee based on the following criteria:

1. *monocentric region (focus on intra-polycentricity)*
2. *different governance structures and planning policies*
3. *no strongly shrinking region: moderate to strong growth.*

In line with these criteria Portland, Oregon, Austin, Texas, Atlanta, Georgia and Philadelphia, Pennsylvania in the USA (location of each city is presented in Figure 2a in chapter 2.2) and Hamburg, Hanover, Berlin and Nuremberg in Germany (location of each city is presented in Figure 2b in chapter 2.2) were selected as study regions.

Portland, Oregon covers an area of 337km^2 (2017) 68km west of the pacific coast in the Willamette River valley between two mountain ranges, the Cascade Range to the east and the lower Coast Range to the west. The Willamette River flows through the city and merges into the Columbia River at the northern edge of the city. The marine air keeps temperatures moderate with mild summers and mild, very rainy winters. Precipitation in general is comparatively high with an average annual total of 890mm. The city has a population count of 667,589, a density value of 1,980/km^2 (2019) and a growth rate of +1.40% (Advameg, Inc. 2019a; Socrata 2019a; World Population Review 2018a; US Climate Data 2019a; Klimatabelle.Info 2019). With these numbers Portland is the largest city of the state Oregon and the second largest after Seattle, Washington in the Pacific North-West area of the USA (World Population Review 2018a & b). The city is also showing continuous growth in its economy. At +2.69% (2018), the increase in employment is higher than the national average (+1.6%; Sperling's Best Places 2019; Portland State University et al. 2018, 10). According to a ranking conducted by the finance website *WalletHub*, which makes a statement about the speed of growth of cities in the USA, Portland is on 24th place in the year 2018, considering the cities with more than 300,000 inhabitants (= total comparison of 66 cities).

The ranking was created under consideration of 15 different metrics such as job and population growth, poverty rate decrease as well as the number of business startups (McCann 2018).

Austin, Texas, the capital of Texas in the middle south of the United States, is located in south central Texas and spreads over an area of 669km^2. The Colorado River crossing the city separates the Texas Hill Country (also known as Edwards Plateau) in the west (hilly grassland) from the black-land prairies in the east (once a tallgrass prairie, now replaced by agriculture). The climate is subtropical with hot summers and mild winters. Most precipitation occurs in the form of rain in late spring and early autumn with an average annual total of 863mm (Advameg, Inc. 2019b & c; Texas Parks & Wildlife Foundation 2019; US Climate Data 2019b). The city has a population count of 1,001,104, a density value of 1,205 people per square kilometer and a population growth rate of +1.80%. After Houston, San Antonio and Dallas, Austin is the fourth biggest urban agglomeration in the state (World Population Review 2018a & c). In addition, Austin has been rated as the No. 1 fastest growing large city (more than 300,000 people) in the country in the year 2018 in the ranking of *WalletHub*. Solely the economic growth rate from 2011 to 2016 is rated at 6.1%, which is more than double the national as a whole (Patch Media 2019; McCann 2018). When considering the increase in jobs in 2018 alone, Austin almost ranks first in national comparison. With a growth rate of +3.9%, only Orlando, Florida recorded a higher score (Salazar 2018).

Atlanta, Georgia is the capital and the largest city of the state Georgia spreading over an area of 342km^2. Located in the foothills of the southern Appalachians in the north-central part of Georgia, the city is relatively close to the Gulf of Mexico and the Atlantic Ocean. The geographical location of the city leads to a mild climate with moderate summers and mild winters. Precipitation falls during the whole year. The average annual total with 1,244mm is very high (Advameg, Inc. 2019d & e; US Climate Data 2019c). In the year 2018 501,178 people lived in Atlanta. The density value is 1,450/km^2 and the population growth rate is +1.94% (World Population Review 2018a). According to the fastest growing large city ranking by *WalletHub* Atlanta is in 10th place (McCann 2018). At +2.9%, the recent job growth rate is higher than the national average (+1.6%; Sperling's Best Places 2019).

Philadelphia, Pennsylvania, located at the confluence of the Delaware River and Schuylkill River in the east of the state, has been in the nation's forefront for more than 300 years in regard to intellectual and economic as well as humanitarian development. With the Appalachian Mountains to the west and the Atlantic Ocean to the east the climate is not marked by extremes with mild and humid summers and moderate winters. Precipitation falls all year round and the average annual total is very high with 1,041mm. The city of 1,579,596 inhabitants spreads over an area of

350km², making it the most densely populated town (4,537 people per square kilometer) of the four American cities under investigation. The growth rate, on the other hand, with +0.18% is comparatively low (Advameg, Inc. 2019f & g; US Climate Data 2019d; World Population Review 2018a). Philadelphia is the biggest city of the state Pennsylvania and the only one with population numbers exceeding 1 million. Moreover, it is the sixth largest city in the whole USA (World Population Review 2018d). In the *WalletHub* ranking the city only is in 51st place out of the total 66 cities with more than 300,000 inhabitants (McCann 2018). Compared to the other study regions in the US the job growth rate is the lowest, even though it has risen with +1.5% in the year 2018. Nevertheless, this count is lower than the national average (+1.6%; U.S. Bureau of Labor Statistics 2019).

Hamburg, Hanover, Berlin and Nuremberg are four out of eleven metropolitan regions in Germany that were defined by the ministerial conference on spatial planning. These are growth and innovation centers with an international or large-scale impact (Marketingverein der Europäischen Metropolregion Nürnberg e.V. 2019, 1f.).

Nuremberg, Bavaria is the cultural as well as the economic center of Northern Bavaria. The urban area, comprising 186.4km², is located in the middle Franconian basin. The region features a warm temperate climate. Characteristic are four seasons and precipitation occurs during the whole year (on average 644mm). Compared to the rest of the region, however, there is less because the pronounced basin location keeps the moist air masses away (Wetter.de 2019; Climate-Data.org 2019a; Stadt Nürnberg 2019a; Bayerisches Landesamt für Umwelt 2011). With 532,194 (2017) inhabitants Nuremberg is the second largest city in Bavaria. The population is constantly increasing. From 2013 to 2018 the growth rate was +4.6%. The city's density value is 2,862 inhabitants per square kilometer (Stadt Nürnberg 2019b; Catcomm Kommunikation 2018). The city is also recording positive economic growth. From 2017 to 2018 the growth rate was +3.2%. This is above the national average of +1.5%. With a gross domestic product (GDP) of 27 billion euros, Nuremberg is also among the top ten of the twenty largest German cities (Stadt Nürnberg 2019c; Statistisches Bundesamt 2019; Catcomm Kommunikation 2018).

Berlin, Berlin is the capital of the Federal Republic of Germany and at the same time a city-state, i.e. one of the 16 federal states of Germany. The city is also the center of the Berlin/Brandenburg metropolitan region in the east of Germany. Moreover, with 891,1km², Berlin is the largest municipality in Germany (Amt für Statistik Berlin-Brandenburg 2019a; Astinus 2016, n.pag.). In the northeast the urban agglomeration lies on the plateau of the Barnim and in the southwest on the plateau of the Teltow, both glacial remains. The Spree flows through the city in an east-west direction and culminates into the Havel in the district of Spandau (Berlinstadtservice 2019,

Naturpark Barnim 2019, Astinus 2016, n.pag.). The climate is warm temperate in the transition zone from maritime to continental climate and is characterized by four seasons. Precipitation falls throughout the year with an average total of 591mm (Climate-Data.org 2019b; Climate Data 2019; Astinus 2016, n.pag.). The population of 3,634,069 million makes Berlin the most populated city in Germany and the numbers are constantly increasing. With 4,071 people per km² it is very dense at the same time. The growth rate in 2017 was +1.1% (compared to the previous year). The economy is also growing steadily. In 2017 the GDP, worth 136.6 billion euros, grew by +3.1%, surpassing the national average of +2.2%. In general, the economy grew by an average of +2.1% per year over the last ten years (Amt für Statistik Berlin-Brandenburg 2019a & b; Senatsverwaltung für Wirtschaft, Energie und Betriebe 2019).

Hanover, Lower Saxony is the state capital of Lower Saxony and at the same time a centrally located industrial and trade fair city in the center of Europe. The city with an area of 204,12km² is situated on the River Leine in the transition area between the North German lowlands and the Lower Saxon highlands. The climate is warm temperate with four seasons and high precipitation rates (total of 666mm; Hannover 2019a & b; Climate-Data.org 2019c). Hanover is located at the intersection of the traditionally highly frequented North-South and East-West axes. This transport advantage favoured the development into a modern big city (Hannover.de 2019a). Currently it has a population of 558,799 (2018) inhabitants, which has increased by +6.3% from 2007 to 2017 and a density value of 2,737 people per km². The growth rate has only slowed somewhat in the last two years. Statistics show a lower increase than in previous years, but growth can still be recorded (Hannover.de 2019c; Landeshauptstadt Hannover 2018, 1f.). In the economic sector, the Hanover region can also record growth. Compared to other densely populated areas, however, it shows slightly below-average growth, but still steady. In 2016, the GDP was 33 billion euros. And since 2010 an average of 10.000 new jobs has been created every year, which corresponds to an average growth of +2.2% (Hannover.de 2019d; Hannover.de 2016).

Hamburg, Hamburg is after Berlin the second largest city in Germany and at the same time, like Berlin, a city-state, i.e. one of the 16 federal states of Germany. The city is located in the North German lowlands at the confluence of the Alster River and the Bille River into the Elbe River. The latter culminates 104km west into the North Sea. Besides, Hamburg has one of the largest and busiest ports in Europe (Statista GmbH 2019a; Encyclopaedia Britannica 2019; Reinthaler 2019). The climate is classified as warm temperate. Due to the maritime influences, winters are milder, and summers are cooler compared to the regions east of the town. The precipitation rates are high with a total of 738mm and in winter storms are frequent (Climate-Data.org 2019d;

Encyclopaedia Britannica 2019). The city occupies an area of 755.1km² and has 1,830,669 (2017) inhabitants with a density value of 2,424 people per square kilometer. Since 1987 the number of inhabitants is steadily increasing (Hamburg.de GmbH & Co.KG 2019; Handelskammer Hamburg 2019). Growth can also be recorded in the economic sector. The GDP amounted in 2017 117.6 billion euros and increased in comparison to the previous year by +2.4%, which is higher than the national average of +2.2% (Dumrath & Fassnacht KG GmbH & Co. 2019; Statista GmbH 2019b; Senatsverwaltung für Wirtschaft, Energie und Betriebe 2019).

2.2 Data

In total, four different data sources are used to create the UMCs (urban mass concentrations) in the first part of this study and the subsequent validation of those. To produce the morphological characterization DSM tiles generated by the TanDEM-X mission, the Global Urban Footprint (GUF) and Sentinel-2 images are employed. As reference data for the validation LoD1 ('Level of Detail 1') building footprints (BF) from several data sources are integrated. The polycentricity analysis in part three in turn is based on the results of the morphological characterization with the resulting UMCs. For an initial overview, the data sources are summarized in Table 2.

Table 2: Summary of the data sources used in this thesis: TanDEM-X DSMs (Digital Surface Models) form the basis for the UMC (urban mass concentration) generation. Besides, the Global Urban Footprint and optical Sentinel-2 images are included in the algorithm. The Microsoft Building Footprint, the Portland Building Footprint, the Austin Building Footprint and the Philadelphia Building Footprint are used to validate the processed UMCs (own Table).

STUDY SECTION	***DATA SOURCE***
MORPHOLOGICAL CHARACTERIZATION OF URBAN AREAS	**DSM tiles** (generated by the TanDEM-X mission) **Global Urban Footprint** **Sentinel-2 images**
VALIDATION	**Microsoft Building Footprint (Release 2017)** **Portland Building Footprint** **Austin Building Footprint** **Philadelphia Building Footprint**

Morphological Characterization

The first data source to be mentioned is the *TanDEM-X* (TerraSAR-X add-on for Digital Elevation Measurement) mission (TDX) operating since 2010. It provides the basic data for the derivation of the UMCs (see chapter 2.3.3). While acting as a large single-pas Synthetic Aperture

Radar (SAR) interferometer, TDX flies in a close orbit configuration with TerraSAR-X (TSX), launched in 2007. They reach a height of 514.8km above the equator and have an orbit repeat cycle of 11 days. SAR interferometry is a further development of conventional radar systems and has the ability to map an area from two different positions without an impact of temporal decorrelation and atmospheric disturbances (AIRBUS 2015, 3; Zink et al. 2014, 10; Deutsches Zentrum für Luft- und Raumfahrt (DLR) e.V. 2009, 8; Krieger et al. 2007, 3317; Moreira et al. 2004, 1). Configuration-wise, TDX and TSX fly in the Helix satellite formation shown in Figure 1 on the right side. It combines a horizontal orbital displacement above the equator with a vertical separation above the poles. Thereby the satellite tracks never cross each other (Zink et al. 2014, 8ff.; DLR e.V. 2009, 8) and typical baseline values lie between 100m and 500m (Wessel 2018, 6).
The primary goal of the mission, the generation of a global, consistent, timely and high precision Digital Elevation Model (DEM) has been concluded, with a horizontal accuracy of 10m and a vertical accuracy of 2m, in January 2015 (Wessel 2018, 6 & 12; Zink et al. 2014, 8). The TDX DEM products, however, primarily present a DSM (Digital Surface Model), because elevated objects are indeed included, but the outcome might be affected by SAR inherent effects (of particular importance in forests, dry snow and ice, where the scattering center lies below the surface; Wessel 2018, 11; Krieger et al. 2007, 3317).
The bistatic InSAR Stripmap mode is used as standard mode for the generation of DEM products. Shown in Figure 1 on the left side, this mode uses either TSX or TDX as a transmitter to illuminate the Earth's surface and the scattered signal is then recorded by both satellites at the same time (for further explanation of other possible operational modes of the TDX mission see Krieger et al. 2007; Krieger et al. 2007, 3317f.). The standard scene size in this mode is 30km x 50km (width and length), but the acquisition length is extendable (AIRBUS 2015, 4ff.).
The unprecedented pixel spacing of 0.4 arcseconds (~12m) allows resolving objects in urban environments above ground such as buildings. Therefore, DEM tiles are used to include 3-D characteristics of the investigated urban areas into the spatial analysis in the frame of this thesis (Geiß et al. 2015c, 4348).
The tiles for the calculation of the UMCs have been created within the framework of the global DEM acquisition phase from December 2010 to January 2015 (Wessel 2018, 6). Thus, no information about the exact date of admission is available. Figure 2 shows the footprints of the tiles used for the four US (Philadelphia, Atlanta, Austin, Portland) and four German (Hamburg, Hanover, Berlin, Nuremberg) urban regions under investigation. Based on Figure 2 it becomes clear that the number of tiles used per city differs depending on the size and the location of the urban region in the global TDX tile coverage.

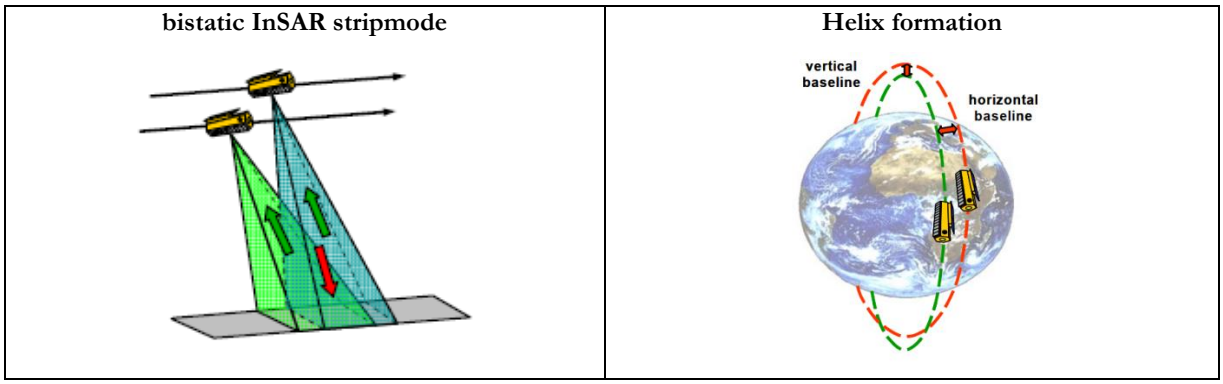

Figure 1: LEFT: Schematic representation of the bistatic InSAR stripmode used for the acquisition of DSM (Digital Surface Model) generation. The reflecting signal from the Earth's surface, either transmitted by TSX (TerraSAR-X) or TDX (TanDEM-X), is recorded by TSX and TDX (Krieger et al. 2007, 3318). RIGHT: Schematic representation of the Helix satellite formation used by TSX and TDX. Horizontal orbital displacement above the equator (=horizontal baseline) and vertical orbital displacement above the poles (= vertical baseline; Zink et al. 2014, 10).

In addition, as the second, the TDX and TSX also provide the data for the derivation of a settlement layer with global coverage: The *Global Urban Footprint* (GUF; Felbier et al. 2014, 4816). To discriminate urban from non-urban areas very high resolution SAR data from the first global coverage between 2011 and 2013 was used. (Esch et al. 2013, 1618). About 180,000 scenes, covering 90% of the world land surface, feed the so-called 'Urban Footprint Processor', a fully automated image classification procedure developed by the German Aerospace Center (Geiß et al. 2017, 2; Esch et al. 2013, 1621). The outcome is a binary built-up/non built-up layer with a spatial resolution of 12m (Klotz et al. 2016, 198). High classification accuracies between 65% and 90% could be obtained as tested for different case study areas (e.g. Klotz et al. 2016; Esch et al. 2013; Taubenböck et al. 2011). Therefore, a reliable separation between built-up/non built-up is assumed (Geiß et al. 2017, 2; Klotz et al. 2016, 198).

Third and last, optical *Sentinel-2 images* are included in the generation of the UMCs. The mission is part of the European Earth Observation program Copernicus. It consists of two polar-orbiting satellites, Sentinel-2A launched in 2015 and Sentinel-2B launched in 2017, phased at 180° to each other and placed in the same sun-synchronous orbit at a height of 786km (European Space Agency 2019c; Gascon et al. 2014, 1f.). The unique satellite constellation has a high temporal (five days at the equator under the same viewing conditions), a high spatial (10, 20 or 60m with regards to the band) and radiometric resolution (13 bands in the visible, near-infrared (NIR) and short-wave infrared (SWIR)) as well as a swath width of 290km. This allows optimal coverage and data delivery and therefore delivers unprecedented views of the Earth (European Space Agency 2019d; Gascon et al. 2014, 1f.). The main mission goal is to provide information for agricultural and forestry practices in form of land-cover maps or change-detection as well as for management of food security through the derivation of various plant indices (European Space

Agency 2019d, e) like the *Normalized Different Vegetation Index* (NDVI; Geiß et al. 2017, 3). In the scope of this thesis images have been selected depending on cloud cover (less than 30%) and date of admission (winter half year). The latter has special significance in this study. The data is used to calculate the NDVI to exclude urban vegetation (see chapter 2.3.3) and by including only winter images effects of photosynthetically active vegetation can be reduced (Geiß et al. 2017, 3).

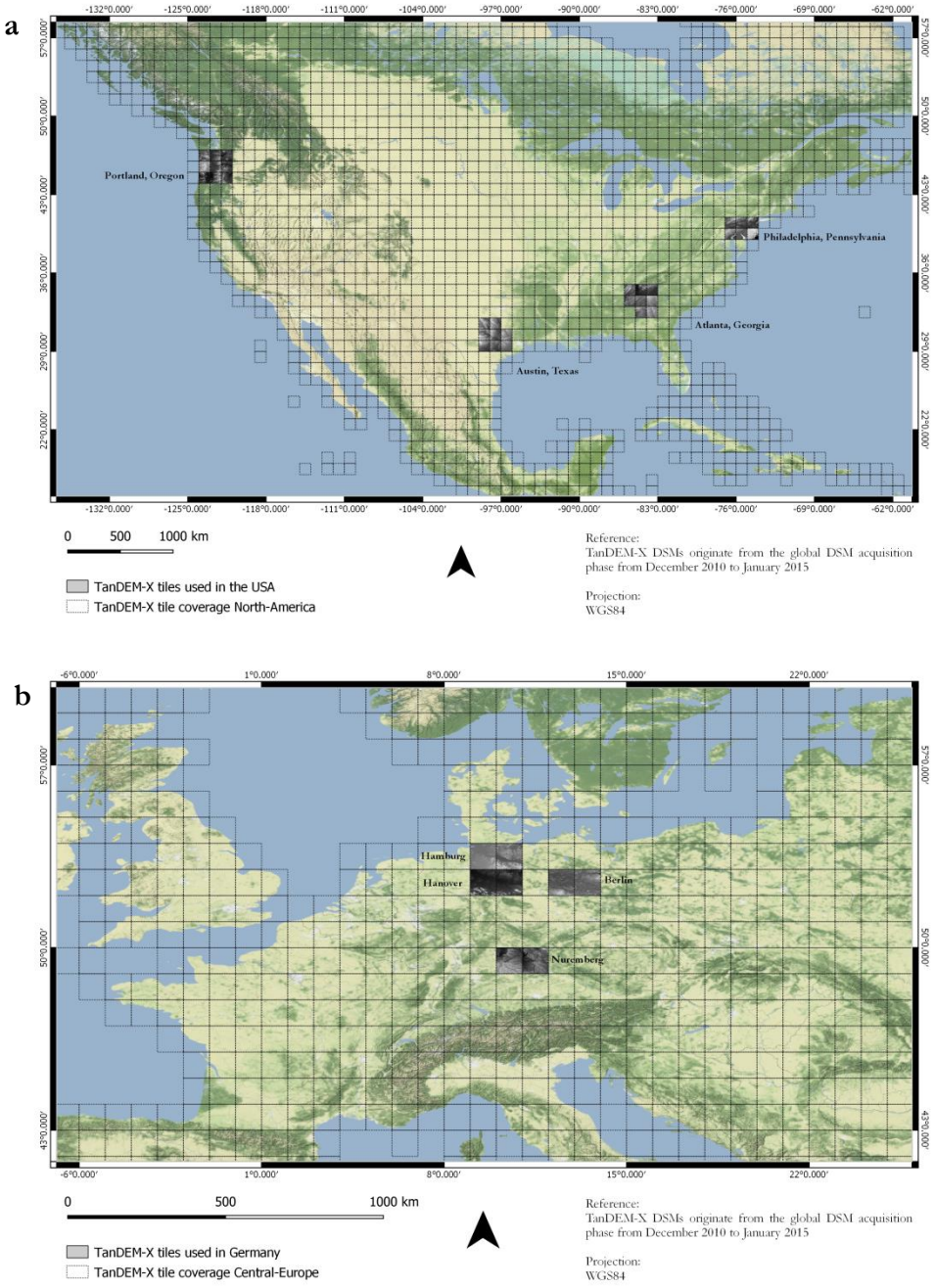

Figure 2: TDX DSM (TanDEM-X Digital Surface Model) tiles used in the United States (a) and Germany (b) to derive UMCs (urban mass concentrations) in the first part of this thesis. Depending on the size and location of the investigation area (four cities each in Germany and the USA), the number of tiles needed to cover the urban region varies: 9 tiles in Portland, 8 tiles each in Atlanta and Austin, 6 tiles in Philadelphia as well as 2 tiles per German city under investigation (own Figure).

Table 3 lists the images, downloaded via *USGS Earth Explorer*, used for each study region (full coverage of each area is only possible by using several images) as well as their dates of recording. In order to adapt the data to TDX/TSX data used in this study, as far as possible in terms of time, mainly recordings from October 2015 to March 2016 have been selected. If no image could be selected due to cloud coverage higher than 30%, records from October 2016 to March 2017 or even October 2017 to March 2018 had to be exploited.

Table 3: List of Sentinel-2 images used in this thesis to calculate the NDVI. The images, downloaded via *UCGS Earth Explorer*, are listed by study region and date of admission (own Table).

STUDY REGION	DATE OF ADMISSION
ATLANTA, GEORGIA, USA	20/10/2015: 3 images 23/10/2015: 1 image 10/02/2016: 1 image 28/03/2016: 1 image 26/11/2016: 4 images
PHILADELPHIA, PENNSYLVANIA, USA	21/10/2015: 1 image 13/11/2015: 2 images 23/11/2015: 2 images 10/12/2015: 1 image 20/12/2015: 1 image 02/01/2016: 1 image 02/03/2016: 1 image 12/03/2016: 2 images 17/11/2016: 1 image
AUSTIN, TEXAS, USA	04/12/2015: 3 images 17/12/2015: 5 images
PORTLAND, OREGON, USA	08/02/2016: 6 images 08/12/2016: 1 image
HANOVER, GERMANY	16/11/2018: 2 images
HAMBURG, GERMANY	09/03/2016: 1 image 26/03/2016: 1 image 09/02/2018: 1 image
BERLIN, GERMANY	28/03/2017: 4 images
NUREMBERG, GERMANY	28/03/2017: 2 images

Validation

Four different data sources are used to validate the calculated UMCs in the scope of this thesis. The first one is the *Microsoft Building Footprint* (MBF) licensed by *Microsoft* under the *Open Data Commons Open Database License* to support the *OpenStreetMap* community. The company released two different data sets; important for the validation of the generated UMC is the first release from 2017. The dataset contains approximately 9.8 million LoD1 building footprintss including the building height in meters for parts of metro regions in 44 US states. The data has been digitized based on very high resolution aerial images captured by Microsoft in 2014 and 2015. To interpolate the height a DTM has been derived from the same data. The footprints are freely available for download and are shared through *Microsoft OneDrive* (link: OpenStreetMap Wiki 2018). The LoD1 data is provided in the coordinate system WGS84 (OpenStrretMap Wiki 2018). In the context of this thesis the MBF for the city of Atlanta covering an area of approximately 13km x 12km is used to validate the 3D UMCs processed for this city.

Second, for Austin, the *Austin Building Footprint* (ABF) from the year 2013 is included in the validation procedure. The basis for the digitalization has been Orthoimagery from 2012 and 2013 as well as LiDAR data from 2012. The open source data can be downloaded from *the official City of Austin open data portal* (City of Austin 2019) in the projection WGS84. The LoD1 data contains the building height (City of Austin 2019), making it ideal for validating the calculated UMCs in Austin. With an area of ca. 75km x 65km the ABF allows an extensive validation of the urban region.

As the third, the *Portland Building Footprint* (PBF) generated by the *Bureau of Planning and Sustainability* is used to validate the generated UMCs for the city of Portland. Originally digitized from aerial images between 1987 and 1994, the data has been gradually extended and updated by using land-use review case information, 3D-Sketchup files provided by architects, aerial images between 1996 and 2007 as well as LiDAR data between 2004 and 2007 to include height information in feet. The data is freely available and can be downloaded from *Koordinates* (open data portal for geospatial applications; Koordinates 2019). The LoD1 data, projected in WGS84/Pseudo-Mercator, offers an almost area-wide coverage (ca. 139km x 70km) of Portland's urban region (Koordinates 2019).

Fourth and last, for Philadelphia, the *Philadelphia Building Footprint* (PHBF) from the year 2014 is used. It has been created by the city itself from the department *'Office of Innovation & Technology'*. The LoD1 data can be downloaded from the city's open data portal called *OpenDataPhilly* (OpenDataPhilly 2019) in the projection WGS84 (OpenDataPhilly 2019) covering an area of approximately 18.5km x 40km. Information regarding the underlying data sources and the method of compiling the PHBF are not available.

2.3 Method

As already described above, the methodology used in the scope of this thesis is divided into three parts. Figure 3 schematically shows this three-step process. First, the urban regions are morphologically characterized by calculating the so-called urban mass concentrations 'UMC' (see chapter 2.3.3). The urban areas of interest are covered with 1km x 1km single grid units and in the context of this thesis, the UMCs represent the building volume per processing unit. To estimate the quality of these calculations, the UMCs are validated subsequently for the USA (see chapter 2.3.4). As explained above, the generation methodology of the UMCs has already been validated for Germany. Finally, the polycentric structure of the case study cities is investigated based on the previously calculated UMCs and a concluding transcontinental comparison between the USA and Germany is drawn (see 2.3.5).

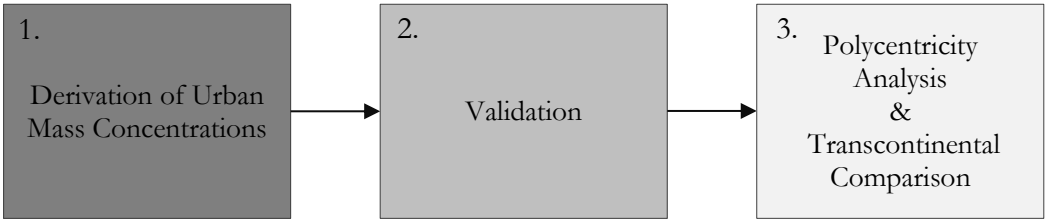

Figure 3: Workflow in the scope of this thesis, consisting of an Urban Mass Concentration generation, a subsequent validation and a concluding polycentricity analysis with an attached transcontinental comparison between the USA and Germany (own Figure).

2.3.1 Scale of investigation

Depending on the characteristics of the individual steps in the method (Figure 3), the extent of the study area varies in size. The different outlines of the examination units are presented in the following.

Morphological Characterization

For the outline of the individual survey area per city, the so-called *'Urban Area'* (UA), defined by the *United States Census Bureau*, is applied to the cities in the USA (example in Figure 4a; United States Census Bureau 2018). Simultaneously, the study region is defined in the German cities. Here, however, the definition of the *European Environment Agency* for *'Urban Morphological Zones'* (UMZ) is used to delimit the area of the German cities (example in Figure 4b; European Environment Agency 2018).

As the UAs differ from each other in terms of size as well as in relation to the UMZs, since the cities do not have the same extent of expansion, it is harder to make national or transcontinental comparisons based on these outlines. In addition, the boundaries of the UAs and UMZs are

subjectively defined by administrative instances, which may not reflect the reality. Furthermore, the available validation may reach in parts beyond the UAs. Therefore, starting from the center, a buffer with a radius of 100km for the USA (example in Figure 4a for the city of Atlanta) and 40km for Germany (example in Figure 4b for the city of Berlin) is additionally drawn around the cities. The center is uniformly determined by the coordinates representing the cities' midpoints in open source GIS like *Open Street Map* or *Google Maps*. The choice of the buffer size gets influenced by two characteristics. It must be chosen so that the UAs/UMZs lie within the buffer to ensure that the entire urban regions are included in the calculations. At the same time, due to the difference in the spatial extent of the cities between the USA and Germany, it is not possible to use the same radius for both countries. A radius of 100km in Germany would far exceed the city boundaries.

As both, the official border of the metropolitan regions and the area that goes beyond them are processed, it is possible to recreate the entire urban morphology as realistically as possible using this approach.

Within this extension the UMCs are calculated on a grid of 1km x 1km pixel size. This is done in coordination with the poylcentricity analysis approach based on Taubenböck et al. (2017a).

Validation

The areal extent of the validation depends on the availability of validation data. Therefore, only a small part of the UA can be validated in Atlanta (Figure 5a). Data availability for Philadelphia is already better, but still not enough to cover large amounts of the UA (Figure 5b). In the case of Austin and Portland, data availability is very good. As Figures 5c & d show, the data even exceeds the UA. In conclusion, the data quality is best for Austin and Portland.

Polycentricity Analysis

The polycentricity analysis is carried out based on the method of Taubenböck et al. (2017a). Therefore, the adjustment of the area-related expansion of this analysis is based on the designs of their approach, which is a 1km x 1km grid covering the underlying data to be analysed (USA: 100km radius around the city center; Germany: 40km radius around the city center). This size is in accordance with the European grid INSPIRE (I*nfrastructure for Spatial Information in the European Community*), which is the reason why this unit size was chosen in the first place (Taubenböck et al. 2017a, 45).

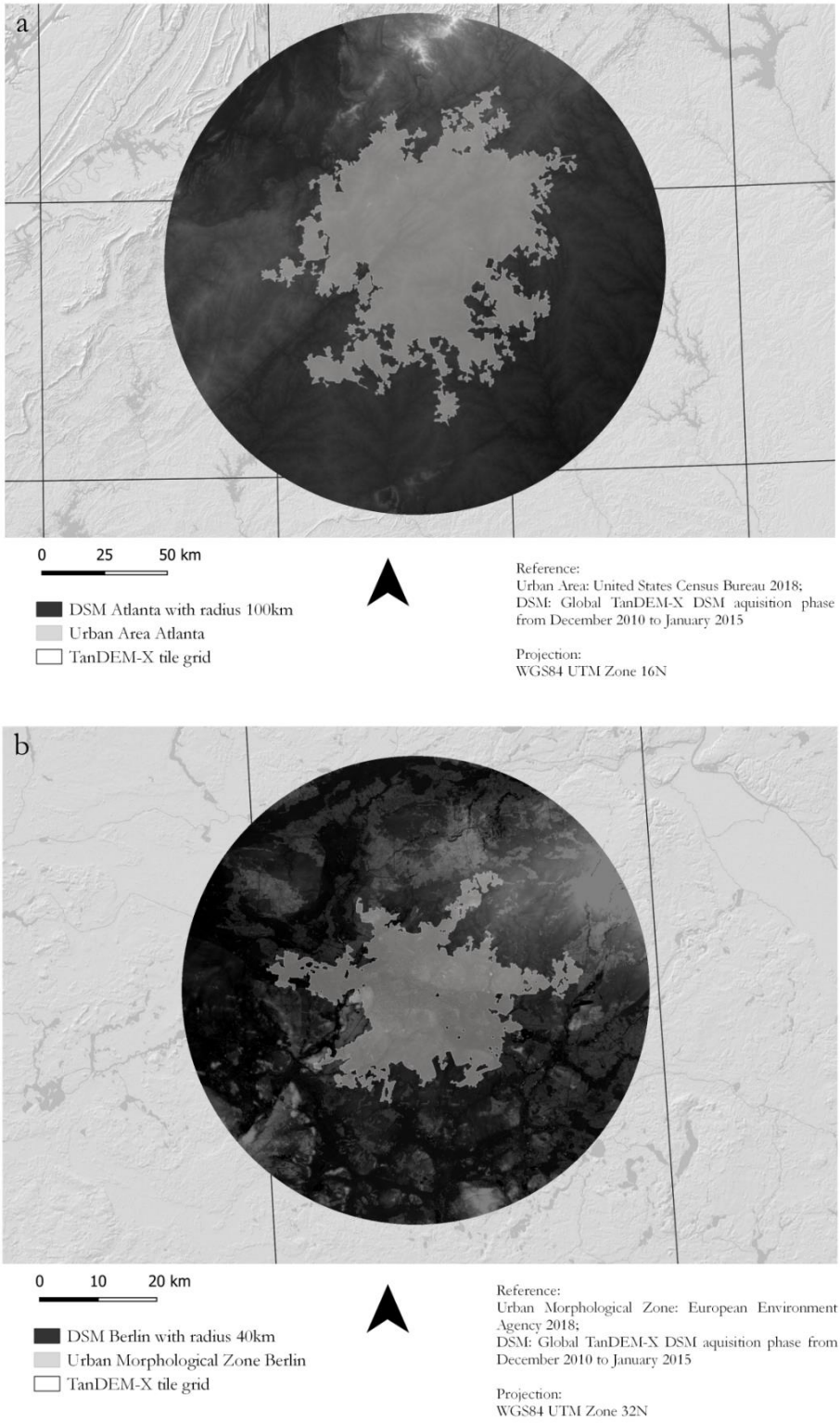

Figure 4: Illustrative presentation of the buffer zone with a radius of 100km around the city center of Atlanta, Georgia, USA and the outline of the Urban Area within (a) as well as of the buffer zone with a radius of 40km around the city center of Berlin, Germany and the outline of the Urban Morphological Zone within (b; own Figure).

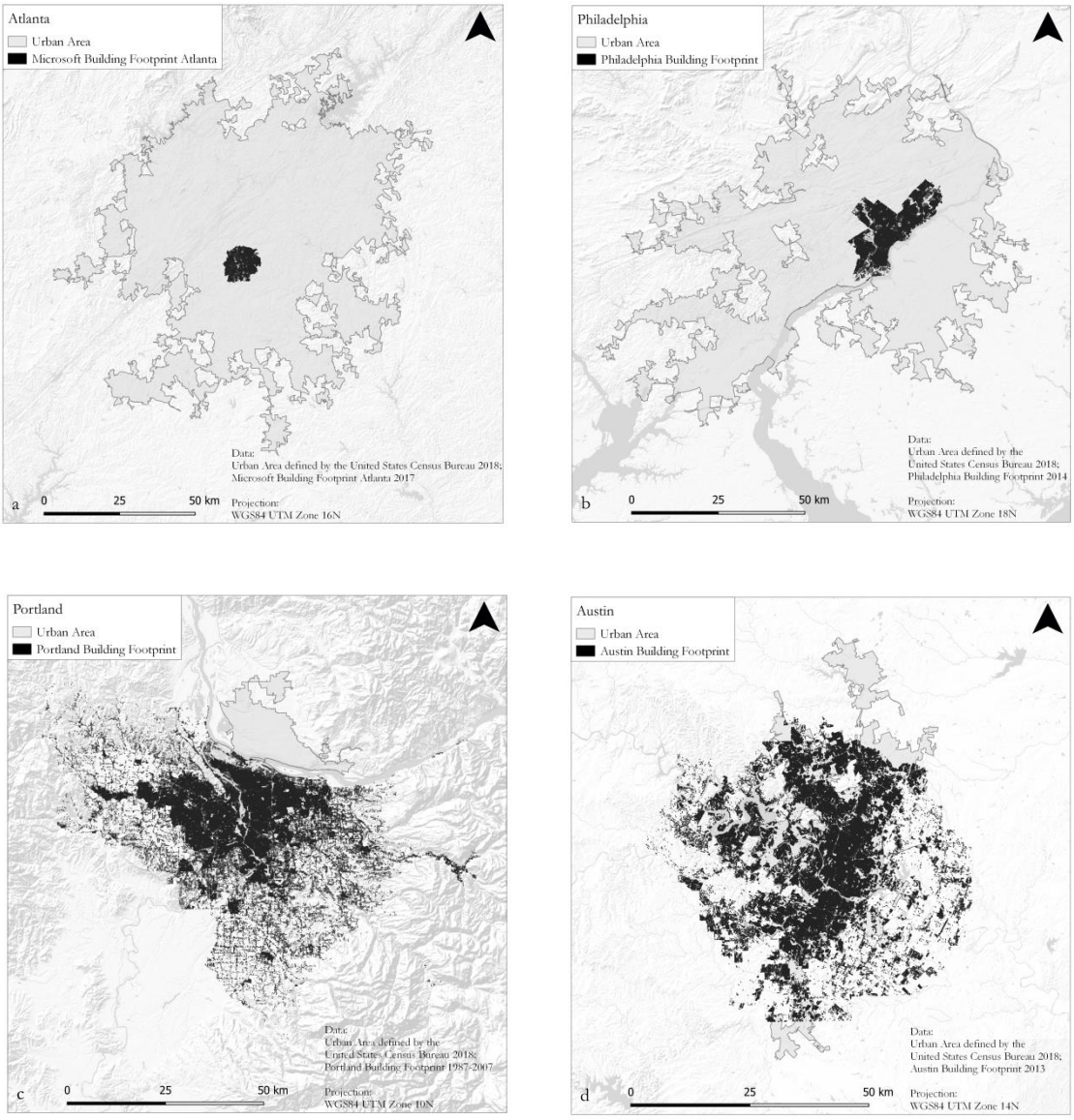

Figure 5: Coverage of the cities under investigation with validation data. In Atlanta (a) and Philadelphia (b) only a small part of the Urban Area is covered, whereas in Portland (c) and Austin (d) the data exceeds the Urban Area (own Figure).

2.3.2 Data preprocessing

Before the data can be utilized in the algorithm framework introduced by Geiß et al. (2015c, 2017) and used in the scope of this thesis, several preprocessing steps must be applied. This section provides information about necessary working steps that need to be carried out before the actual generation of UMCs (preprocessing Input data) and the validation (preprocessing reference data).

Data for UMC calculation

The extent of the investigation outline of the cities included in the survey cannot be covered with one TDX-Tile. Depending on the location within the global TDX-Tile coverage and the size of

the urban region, several tiles are required per city (see Figure 2). Therefore, they are mosaicked into one layer in order to obtain a consistent data set for each city as the basis for the investigation. The same applies to the Sentinel-2 images and the GUF, which are also tailored to the size of the urban regions of the different case study cities. Furthermore, the data is transformed from WGS84 into WGS 84 UTM with the respective corresponding zone (see Table 4).

Table 4: List of the used projection of each urban region in the scope of this thesis (own Table).

URBAN REGION	PROJECTION
PORTLAND	WGS84 UTM Zone 10N
AUSTIN	WGS84 UTM Zone 14N
ATLANTA	WGS84 UTM Zone 16N
PHILADELPHIA	WGS84 UTM Zone 18N
HAMBURG	WGS84 UTM Zone 32N
HANOVER	WGS84 UTM Zone 32N
BERLIN	WGS84 UTM Zone 33N
NUREMBERG	WGS84 UTM Zone 32N

The TDX data and the GUF represent finished data products - DSM and 'Built-up'/'non Built-up' layer -, which is why no further preprocessing steps are required. The Senintel-2 data, on the other hand, are subjected to an atmospheric correction within the Sentinel Application Platform (European Space Agency (ESA) 2019a) using the Sen2Cor module (ESA 2019b). This step is necessary to obtain level 2A products that contain the Bottom of Atmosphere- instead of the Top of Atmosphere - reflectance (Louis 2017, 10). After that, the NDVI is calculated. As described in 2.2, this index is used to exclude urban vegetation in the UMC generation. This is possible because the NDVI is an indicator for photosynthetically active vegetation (Meera Gandhi et al. 2015, 1201) and is defined as (Rouse et al. 1973, 43)

$$NDVI = \frac{n - r}{n + r}\,, \qquad \textbf{(Eq. 1)}$$

where n is NIR reflectance in the wavelength range 750nm - 1300nm and r is visible red reflectance in the wavelength range 600nm - 700nm. Green vegetation has a strong absorption in the red band as well as a high reflectance in the near infrared. Therefore, the ratio of these two bands provides an indicator for green vegetation (Rouse et al. 1973, 43; Alatorre & Begueria 2010, 8). Values of the NDVI range from -1 to +1, where negative values represent water bodies,

values of 0.1 and below correspond to barren areas of rock, sand or snow, values between 0.2 and 0.3 are considered as moderate and indicate e.g. grassland and NDVI values above 0.3 are considered as indicator for active vegetation (Meera Gandhi et al. 2015, 1202).

Data for UMC validation

In general, like it is the case for the input data, the reference data's projection is transformed into UTM with the respective zone (see Table 4). Afterwards, the area of the building polygons of the LoD1 building footprints needs to be calculated in order to generate the volume per reference unit for the subsequent comparison with the generated UMCs based on TDX DSM data (area of the TDX DSM = pixel size). Moreover, in the case of the PBF the height indication must also be converted into the unit meter to use it for the comparison with the calculated UMC for Portland.

2.3.3 Morphological Characterization

Previous EO studies mainly analysed urban environments based on adequate and properly encoded prior knowledge (e.g. Geiß et al. 2015c, 2016; Wurm et al. 2016). Geiß et al. (2017) introduced an approach to quantitatively characterize urban environments without the incorporation of previous knowledge (Geiß et al. 2017, 1). Based on this method the workflow to generate the UMCs in the scope of this thesis is introduced in Figure 6. The procedure, which is displayed simplified in the illustration will be explained in the following in more detail.

2.3.3.1 Normalized Digital Surface Model generation

To generate the nDSM (Figure 6 methodological step one) a Digital Terrain Model (DTM) must be derived from the TDX-DSM in the first place. The DTM contains elevation measurements of the Bare Earth (BE) without including natural and artificial objects above ground. In the next step, the elevation of the terrain (height of the DTM) must be removed from the elevation of the surface containing all objects above ground (height of the DSM) to calculate the nDSM (Geiß et al. 2015c, 4349):

$$nDSM = DSM - DTM. \qquad \textbf{(Eq. 2)}$$

Before the actual procedure to derive the DTM in this thesis, which is created using a *Selective Object-Based & Region-Growing-Based Progressive Morphological Filter* (RPMF-SOBV) approach introduced by Geiß et al. (2015c), basic clarifications regarding morphological filter procedures - *Classic Morphological Filtering & Progressive Morphological Filtering* - are made. They are necessary to understand the RPMF-SOBV approach as they are also part of it.

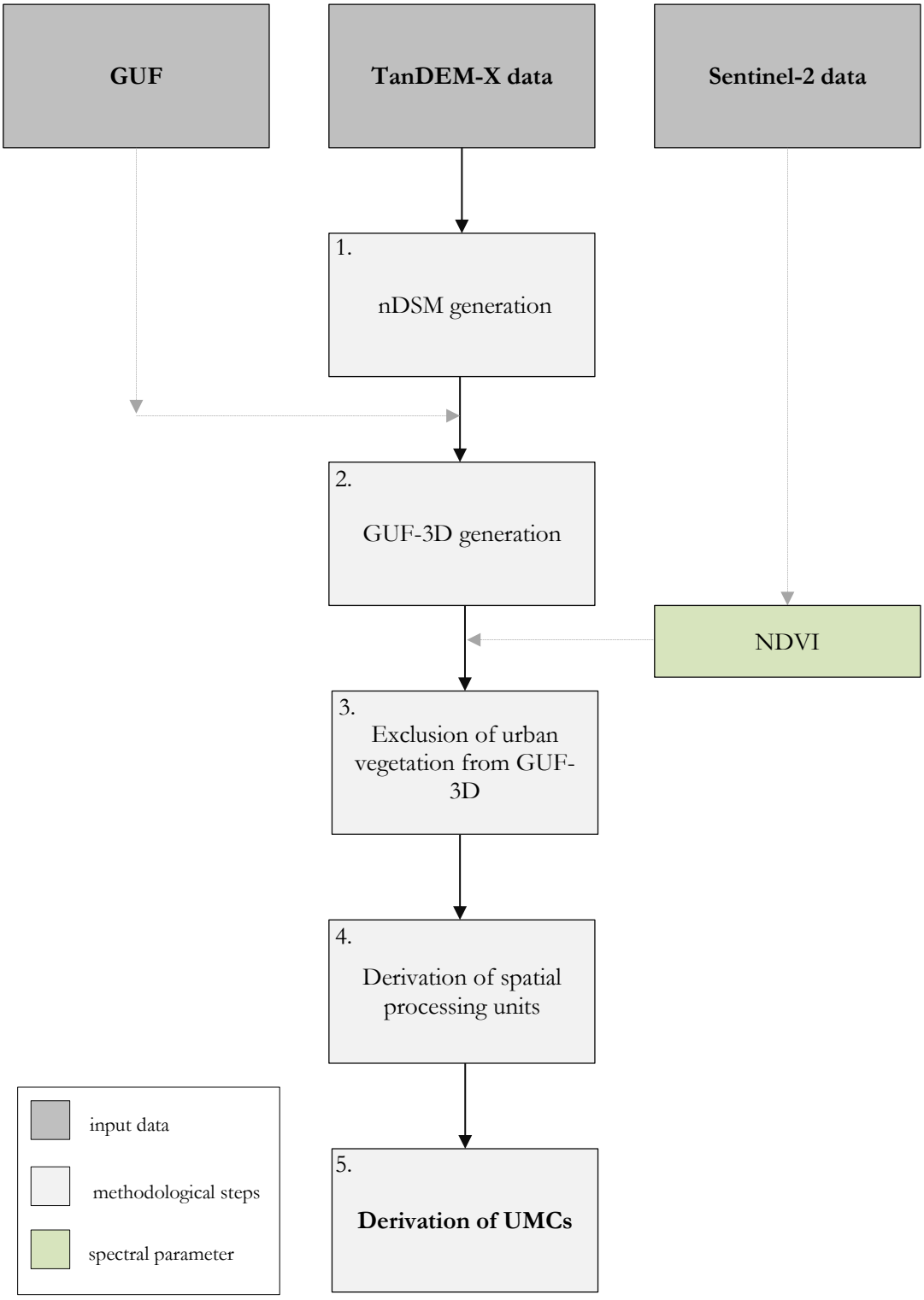

Figure 6: Schematic representation of the UMC (urban mass concentration) generation workflow. First an nDSM (normalised Digital Surface Model) indicating the height of features above ground is derived (methodological step 1). The nDSM is masked with the GUF (Global urban Footprint) and the NDVI in the following to only obtain urban building pixels (methodological step 2 & 3). The outcome is clipped with a 1km x 1km grid to calculate the UMC per processing unit (methodological step 4 & 5; own Figure).

The lower spatial resolution of the TDX-DSMs compared to DSMs conducted from stereoscopic optical acquisitions, interferometric SAR measurements or laser scanning (e.g. Sirmacek et al. 2012; Wurm et al. 2011; Gamba & Houshmand 2000) limits the use of many of the existing approaches to generate a DTM. Unlike with very high resolution DSMs, it is for example not possible to use the profound difference between the slope of terrain and that of nonground objects like buildings to derive the DTM (e.g. Vosselman 2000; Sithole 2001). Furthermore, the elevation measures of the TDX mission are converted into regular grayscale grid images. Therefore, only approaches that are also suitable for this type of images can be considered (Geiß et al. 2015c, 4348).

Classic Morphological Filtering

Due to the above-mentioned characteristics mathematical morphology-based filters - *Morphological Filters* (MF) - are suited for the DTM derivation. Mathematical morphology stems from set theory and in the case of image processing sets represent the spatial structures in the image, which are manifested as subgraph in grayscale or object in binary images. The use of these filters is relatively simple in accordance with good performance (Geiß et al. 2015c, 4348; Soille 2004, 1 & 66). For a MF a structuring element (SE) is needed in addition to the initial image, in the scope of this thesis the TDX DSM. In the case of an underlying grayscale image (here the DSM) the SE is a small grayscale image, and shape as well as size must be adopted to the geometric properties of the spatial structures in the image that is to be processed, e.g. hexagonal, diamond or square grids (for further explanations see Soille 2004). In the framework of this thesis the SE is a square window of size $a \times a$ (Geiß et al. 2015c, 4349; Ravi & Khan 2013, 17; Soille 2004, 64f.). By moving the SE over the entire DSM dataset, placing the origin/center of the SE at each pixel in the dataset, the values underlying the center of the SE get transformed (Erhardt 2008, 163). In dependence of the MF operation (e.g. erosion, dilation) this leads to shrinking or growing of image features such as removing bridges or to the filling of gaps and holes. In scientific terms this is donated as noise reduction and edge detection (Soille 2004, 4). In the scope of this thesis by using a MF BE pixels (corresponding to lower values = darker pixels = non-elevated) in the DSM get identified and potential nonground objects (OBJ) removed as the stay unclassified (corresponding to higher values = brighter pixels = elevated; Zhang et al. 2003, 873). The primary morphological operations are *dilation* and *erosion*. Erosion ε causes an image object to decrease in size (Ravi & Khan 2013, 18) and the transformation of the DSM Z by the SE B is defined as the minimum of the translations of Z by the vectors $-b$ of B (Soille 2004, 66ff.):

$$\varepsilon B\,(Z) = \bigwedge_{b\,\in B} Z_{-b.} \qquad \textbf{(Eq. 3)}$$

Analogously, dilation δ causes image objects to increase in size (Ravi & Khan 2013, 18) and is defined as the maximum of the translations of *Z* by the vectors *–b* of *B* (Soille 2004, 66ff.):

$$\delta B\ (Z) = \bigvee_{b\ \in B} Z_{-b.} \qquad \textbf{(Eq. 4)}$$

Originating from basic erosion and dilation operations more complex variations can be carried out (Amalorpavam et al. 2013, 146). Amongst them is the *morphological opening* γ. Applied on each measurement of the DSM it is possible to derive a DTM with this operation (e.g. Harlick et al. 1987; Weidner & Förstner 1995), which is created by a dilation executed on the result of an erosion (Soille 2004, 66ff.):

$$\gamma_B\ (Z) = \ \delta_B\ ^\circ\ \varepsilon_B\ (Z). \qquad \textbf{(Eq. 5)}$$

To fully eliminate the objects of interest (in the scope of this thesis: buildings) with an opening operation, the size of the SE must exceed the outline of the object of interest in every instance. Therefore, it is defined as 2 x d_{max} + 1, where d_{max} is the largest distance from the center of a building to the nearest BE point within the investigated area (Geiß et al. 2015c, 4349; Zhang et al. 2003, 875). The determination of d_{max} is carried out empirically by visual inspection of satellite images, e.g. in *Google Earth*. It is essential to understand that the largest distance between the center of a building and the next BE point can be found at the largest building within a scene, but it does not necessarily have to be found there. For a better understanding, this method is shown in Figure 7 exemplarily for one TDX DSM tile in the 100km radius extent of Atlanta.

In general, in the case of very high resolution DSMs (≠ TDX DSMs), the selection of a filtering window and the distribution of buildings and trees in a certain area are critical for the performance of the MF. In the case of a small SE most of the ground points will be preserved, but only small OBJ like cars or trees will be removed. A big SE calculated with d_{max}, on the other hand, leads to an overestimation in the final nDSM, because BE pixels get mistakenly treated as OBJ. At the same time, it is difficult to detect all OBJ of various sizes using only one fixed filtering window size as it is the case with *Classic Morphological Filtering*. Errors occur especially in steep terrains (e.g. Maguya et al. 2013; Meng et al. 2010; Geiß et al. 2015c, 4349f.; Zhang et al. 2003, 873f.).

Figure 7: Derivation of the SE (structuring element) exemplarily shown for one TDX DSM (TanDEM-X Digital Surface Model) tile in the 100km radius extent of Atlanta. The length of the measurement (yellow line in the optical satellite image) is divided by '2' to derive the distance from the center of the building to the nearest BE (bare earth) point (top right). Subsequently the result is divided by the pixel size of the DSM (deviating from standard 12m depending on the position in the global TDX grid) to generate d_{max} (middle right). The last step is the calculation of SE by inserting d_{max} in the equation 2 x d_{mx} +1 (bottom right; own Figure; image from *Google Earth 2018*).

Progressive Morphological Filtering

To overcome drawbacks related to MF another similar method - *Progressive Morphological Filter* (PMF) - has been introduced in the scientific community. BE pixels get separated from OBJ in a progressive procedure, where the size of different features above ground is considered. Figure 8 shows this advanced process of separating BE pixels schematically. An initial filtered surface is derived through an opening operation with an initial window size of the SE *B*. Thereby OBJ smaller than the SE are removed while large nonground features are preserved. The next step is the calculation of a preliminary nDSM (pnDSM; ΔZ) with the derived DTM. An elevation difference threshold θ is applied afterwards to identify the final OBJ pixel of this round. In a next iteration the opening operation is applied, with an increased size of the SE *B*, to the filtered surface of the previous round. This results in a further smoothed surface and identification of additional OBJ. The threshold can be varied in dependence of the size of the SE to identify features of differing magnitudes, e.g. low thresholds for small sizes of the SE to eliminate small objects like bushes or cars (note: this is the case for very high resolution DSMs, but mentioned here to explain the PMF in general) and larger thresholds for bigger sizes of the SE to remove

buildings. This procedure is reiterated until the maximum size of the moving window with d_{max} is reached. Subsequently all unclassified pixels (≠ OBJ) get considered as BE and will be used for the interpolation of a final DTM (Geiß et al. 2015c, 4350; Zhang et al. 2003, 874f.).

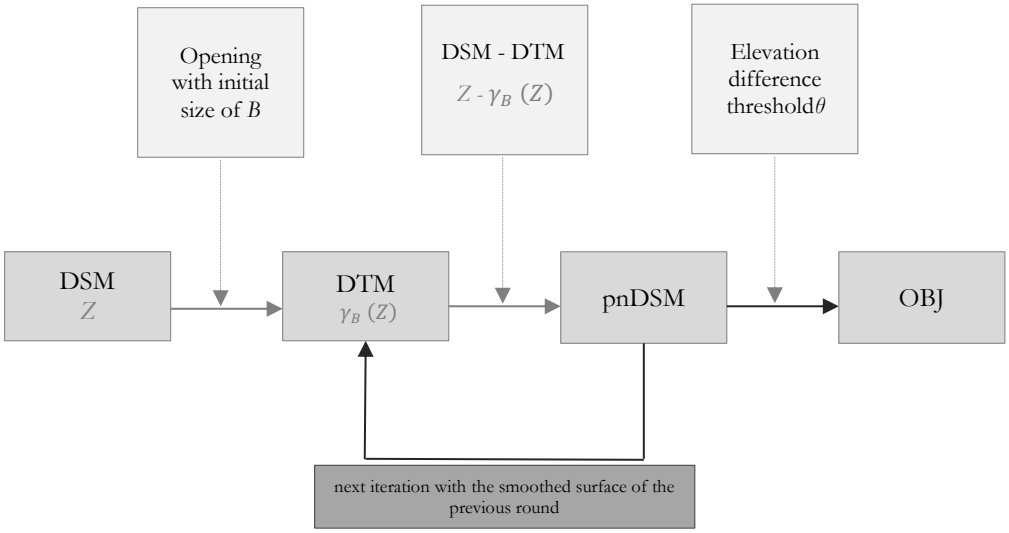

Figure 8: Schematic representation of the PMF (Progressive Morphological Filter) approach. In a progressive way OBJ pixels (nonground objects) get identified in a step by step procedure through adapting the SE *B* (structuring element) and the threshold *θ* to the size of features above ground. All unclassified pixels at the end (= iteration with maximum size of the SE *B* = SE calculated with d_{max}) will be considered as BE pixels (bare earth) and will be interpolated to a DTM (Digital Terrain Model; own Figure).

However, the spatial resolution of the TDX DSM prevents the usage of this progressive procedure. Even the smallest size of the SE *B* (= 3 x 3 pixels ≈ 12m x 12m in the TDX DSM: smallest possible SE with a center pixel) can easily exceed the size of a building. In consequence the advancement of a PMF approach cannot be utilised as in previous studies (e.g. Pingel et al. 2013; Chen et al. 2007; Zhang et al. 2003). Furthermore, similar to the MF the PMF shows a comparable good performance in flat terrains but is prone to errors in steep terrains. The occurring errors belong to two basic groups: *error of commission* (false positives), where pixels are mistakenly classified as BE, and *error of omission* (false negatives), where pixels are mistakenly classifies as OBJ. The influence of these mistakes on the final nDSM differs regarding terrain characteristics. In a perfectly flat terrain, a high omission error has no great influence on the quality of the nDSM. Only a few correct classified BE pixels can give an adequate representation of the ground. Whereas in steep terrains, where distinctive differences in the elevation with respect to surrounding areas are present, a high omission error leads to an overestimation of objects and their height in the final nDSM (Geiß et al. 2015c, 4350).

Region-Growing-Based Progressive Morphological Filtering with Selective Object-Based Voting

To overcome these problems especially associated with nonflat terrain, Geiß et al. (2015c) have developed a strategy to reduce omission errors. This approach has been developed specifically to allow for DTM generation from moderate resolution images like the TDX DSMs, as well. Therefore, this method is applied in the scope of this thesis. Figure 9 shows the process of the algorithm. It is composed of MF, PMF and further steps and will be explained in detail in the following.

The algorithm shown in Figure 9 can be separated into four main steps:

1) *Morphological Filter Operation with B_{max} (different depending on the region under investigation) and subsequently identification of BE pixels by applying an elevation difference threshold θ*
2) *Application of a Progressive Morphological Filter Operation based on region growing on the remaining pixels to identify OBJ pixels*
3) *Postclassification process to identify additional OBJ and BE pixels*
4) *Interpolation of all BE pixels from step 1) and BE pixels from step 3) to generate a DTM and finally calculate the nDSM*

Due to size issues in the software environment *eCognition*, which is used to apply step 1) to step 3) of the algorithm shown in Figure 9 to the TDX DSM of each city, the dataset of each urban area cannot be processed in one. Instead only one part of the data within the buffer-zone (100km for the USA; 40km for Germany), separated by the outline of the respective TDX DSM tile, is processed per *eCognition* run. An example for this separation process is given in Figure 10, representing Portland and the city's separate TDX DSM parts of processing. The results are mosaicked again after the BE extraction (Figure 9 step 3)) and before the DTM generation (Figure 9 step 4)).

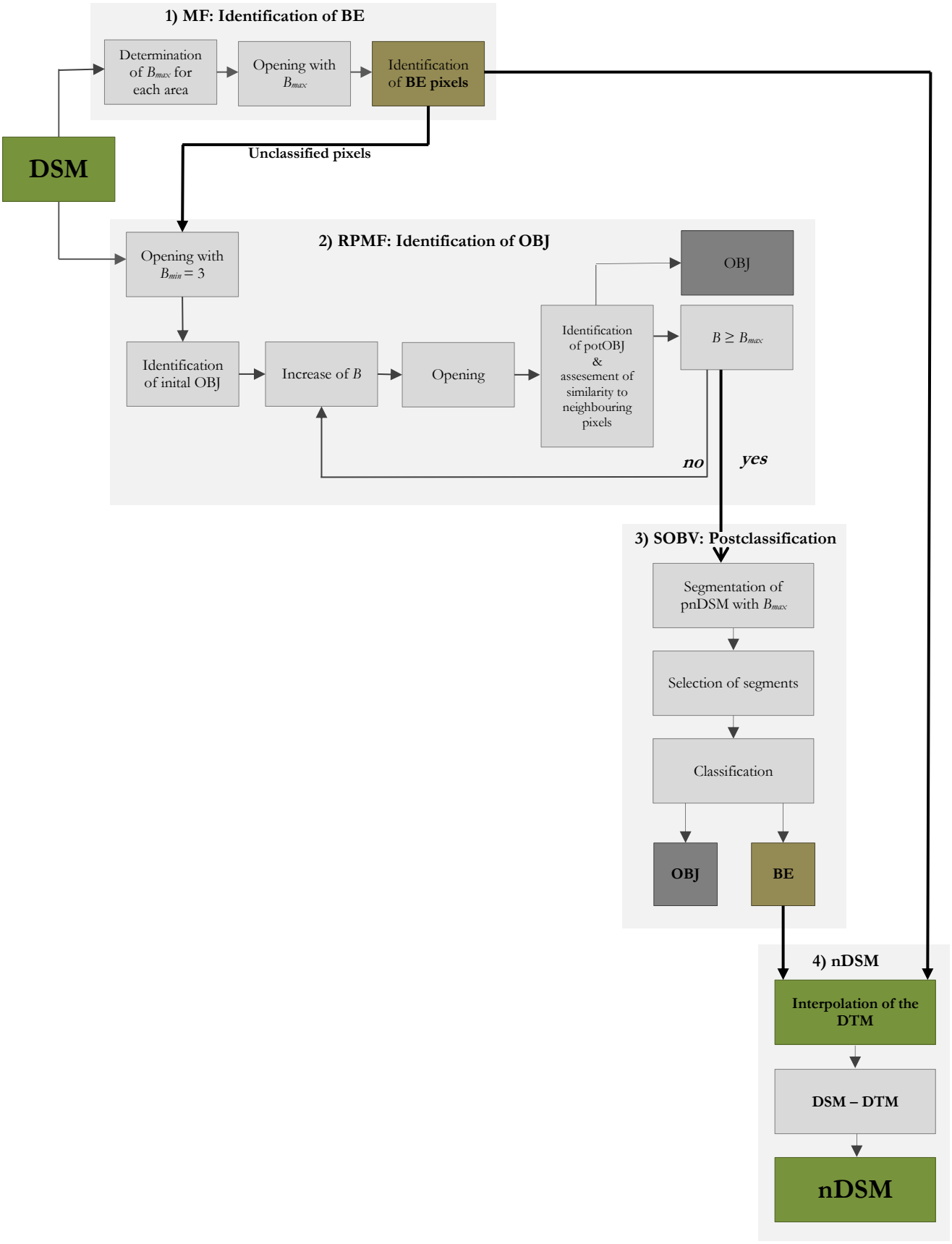

Figure 9: Flowchart of the RPMF (Region-Growing-Based Progressive Morphological Filter) approach with SOBV (Selective Object-Based Voting) used in this thesis to generate the nDSM (normalised Digital Surface Model) for each city under investigation. The method has been developed by Geiß et al. (2015c) and consists of four main steps: 1) identification of BE pixels (bare earth) with a MF (Morphological Filter), 2) identification of OBJ pixels (nonground objects) with a region growing PMF (Progressive Morphological Filter), 3) postclassification to select additional OBJ pixels and 4) interpolation of a DTM (Digital Terrain Model), which enables the calculation of an nDSM (own Figure after Geiß et al. 2015c, 4351).

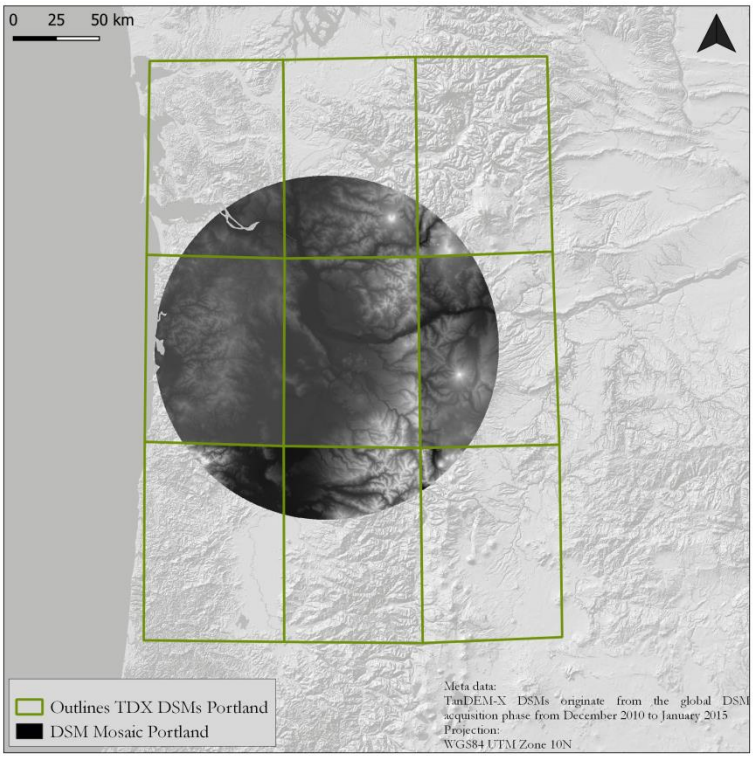

Figure 10: Mosaicked DSM (Digital Surface Model) of Portland corresponding to the area within a 100km radius around the city center. Due to size issues in *eCognition* the DSM cannot be processed in one run. It is separated into nine parts by the outlines of the respective TDX (TanDEM-X) DSM tile. Each part is processed separately (own Figure).

Step 1: Identification of BE pixels

Within step 1), Figure 9, a MF is applied to the TDX DSM. Therefore, the maximum size of the SE is calculated for each processing part in each urban region by determining d_{max} through visual inspection of optical satellite images in *Google Earth*. A separate d_{max} value is determined for each processing part of the respective urban region under investigation and subsequently one SE is calculated per processing part (e.g. in Portland, shown in Figure 10, nine separate d_{max} values are determined and thus nine separate SEs are calculated). As explained above, it is important that the SE always exceeds an object's outline to fully eliminate them. Exemplarily, the determined d_{max} values for the nine processing parts in Portland and their corresponding subsequent calculated SEs are listed in Table 5.

In contrast to a classic MF BE pixels get identified by applying an elevation difference threshold consecutively ($< \theta =$ BE). The threshold used in the scope of this thesis is 2.6m. With the threshold being quite small it is ensured that also small and low buildings get recognized. The value has been set by Geiß et al. (2015c), who tested different variations in order to identify the most fitting one to represent the lowest possible building height. For further explanations of the determination see Zhang et al. (2003) and Geiß et al. (2015c). BE pixels identified this way can be

regarded as reliable (low commission error), but at the same time not as complete (high omission error; Geiß et al. 2015c, 4350 & 4356f.).

Table 5: d_{max} values used in this thesis to calculate the SEs (structuring elements) for Portland: $B = 2 \times d_{max} + 1$. Identification of d_{max} through visual inspection of optical satellite images. The titles of the individual mosaic parts refer to the arrangement in Figure 10. In the case of the processing parts 'bottom right' and 'top right' the calculated SEs are smaller than the smallest possible SE (=3). In this case a SE with the size 3 (=B_{min}) is used (approach by Geiß et al. 2015c).

PORTLAND MOSAIC PART	D_{MAX} [PIXEL]	*SE [PIXEL]*
1) TOP LEFT	5.5722	12
2) TOP MIDDLE	8.2414	18
3) TOP RIGHT	0.9696	3
4) MIDDLE LEFT	5.0577	11
5) MIDDLE MIDDLE	10.8549	23
6) MIDDLE RIGHT	6.6369	14
7) BOTTOM LEFT	7.7808	17
8) BOTTOM MIDDLE	6.8159	15
9) BOTTOM RIGHT	0.7197	3

Step 2a: Identification of initial OBJ

Carrying on, all still unclassified pixels (≠ BE) from step one form the basis for the RPMF approach to progressively identify OBJ pixels (see Figure 9 step 2)), which leads to a further separation of BE pixels and objects above ground.

First, initial OBJ pixels get identified through a two-step procedure with a SE corresponding to B_{min} (= 3 x 3 pixel). As shown schematically in Figure 11 different strategies are used for objects smaller and objects larger than B_{min}. To identify buildings smaller than B_{min} (see Figure 11a) a PMF is applied to the surface to calculate a pnDSM (process described in Figure 8). Subsequently the elevation difference threshold (θ = 2.6m) is applied to identify OBJ pixel (> θ = OBJ; Geiß et al. 2015c, 4350).

For objects larger than the minimum size of the SE an alternative strategy (Figure 11b) is exercised. These features are fully preserved in the surface obtained with the opening operation for objects smaller than the SE (Figure 11a) and thus are not part of the pnDSM. By subtracting the result of the erosion (= first step of the opening) from the result of the opening operation the border pixels of an elevated object get identified (see Figure 11b middle image). To classify them ultimately as OBJ or non-OBJ a combination of an edge extraction filter (Lee-sigma) and contrast segmentation is applied on the resulting surface of the subtraction (Geiß et al. 2015c, 4350). The Lee-Sigma filter is a local smoothing scheme. It uses the sigma probability of the Gaussian distribution to smooth noise (any random clutter of three or less pixels) near edge areas. This is done by replacing these pixels values with the average of only those neighbourhood pixels values

which have their intensity within two standard deviations of the mean grey value of the pixel to be smoothed. Any pixel outside this range is most likely from a different population and should be excluded from the average. By doing so, edges get extracted. They ideally represent boarder pixels of building objects (Geiß et al. 2015c, 4351; Lee 1983, 255ff.). In the following the extracted pixels, most likely representing buildings, are getting finally classified as OBJ or non-OBJ (pixels stay unclassified) by deploying a contrast segmentation algorithm. It divides the filtered image into dark (here: non-elevated) and bright (here: elevated) pixels. To maximise this contrast the segmentation iteratively adapts a threshold, whereby different pixel values from low to high as well as intermediate values are considered as potential thresholds. The contrast between bright (b) and dark (d) to evaluate the threshold delivering the best outcome is calculated as follows (Geiß et al. 2015c, 4351; Wurm et al. 2011, 128f.):

$$contrast = \frac{b - d}{b + d}. \qquad \textbf{(Eq.6)}$$

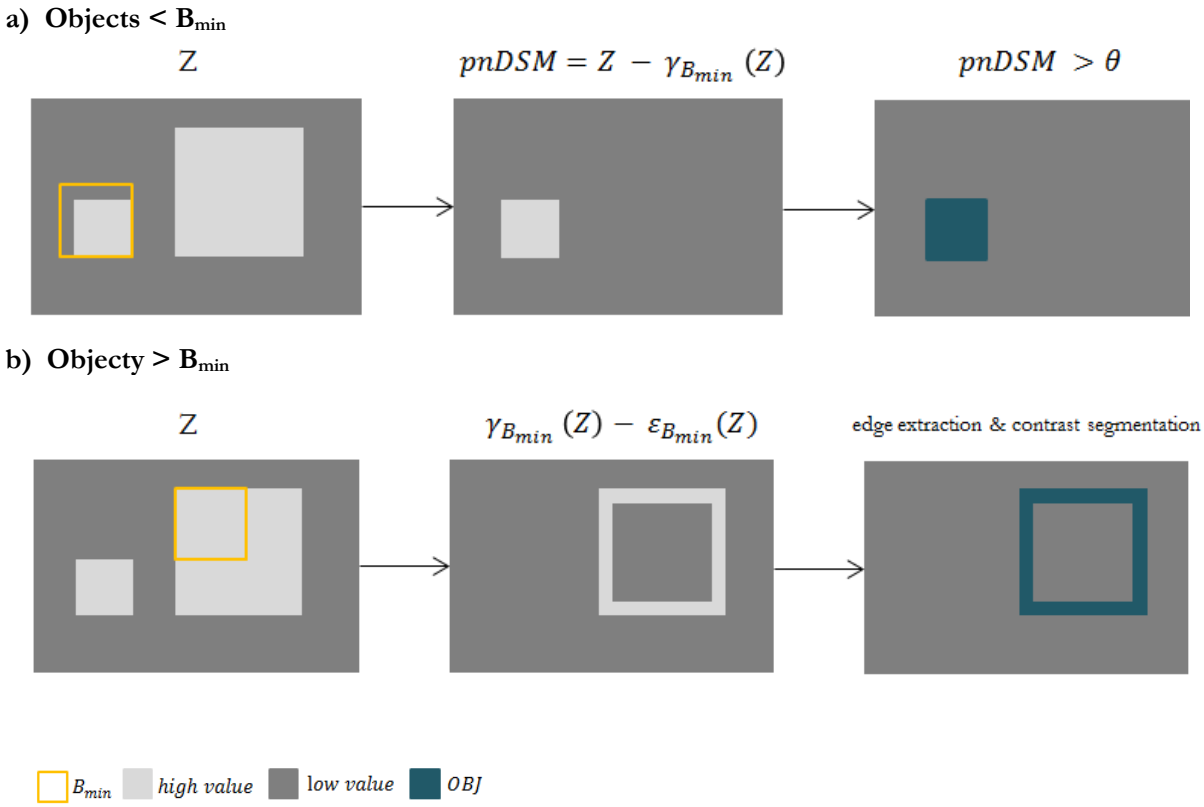

Figure 11: Schematically illustrated identification process of initial OBJ pixels (nonground object). They form the basis for the RPMF (Region-Growing-Based Progressive Morphological Filter) approach (see first part of step 2) in Figure 9). First, an opening operation is executed with the smallest possible SE *B* (structuring element; =3). In the case of objects being smaller than B_{min} (a) a pnDSM (preliminary normalised Digital Surface Model) is calculated after the opening and pixels get classified as OBJ by the elevation difference threshold (=2.6m) subsequently. In the case of objects being larger than B_{min} (b) the result of the erosion (= first part of the opening operation) is subtracted from the result of the opening operation. By this, border pixels of potential elevated objects are identified. Potential OBJ are finally classified as OBJ or BE (bare earth) by applying an edge extraction filter and a contrast segmentation (own Figure recreated after Geiß et al. 2015c, 4351).

Step 2b: Identification of OBJ

The filtered surface with initial OBJ pixels (= result Step 2a: *Identification of initial OBJ*) serves as input to identify additional OBJ pixels in Step 2b. A morphological opening procedure is applied (see Figure 9 step 2)), where the size of *B* is increased linearly by (Geiß et al. 2015c, 4351)

$$B_d = 2\ x\ d + 1 \qquad \textbf{(Eq.7)}$$

where d = 3, 5, 7,…., d_{max}, with d_{max} representing the largest number of pixels between an OBJ pixel and the next BE pixel (see Figure 7 for the derivation). Depending on d_{max} the parts of the urban regions under investigation undergo a different number of iterations, where the filtered surface from the previous opening process is subject to a next opening operation with an increased size of *B*. At each iteration a pnDSM gets calculated (see Figure 8 for this process) and the threshold (θ = 2.6m) gets applied to identify potential OBJ pixels (potOBJ; = pixels exceeding the threshold). To get classified as final OBJ pixel they then must fulfil a similarity constraint with respect to already classified neighbouring OBJ pixels, which share a common border. The similarity gets examined by (Geiß et al. 2015c, 4351)

$$sim(potOBJ, OBJ) = \begin{cases} 1, \left|\mu\left(\Delta Z_{OBJ}\right) - \Delta Z_{potOBJ}\right| \leq \eta \\ 0, else \end{cases} \qquad \textbf{(Eq.8)}$$

where ΔZ represents the pnDSM, μ the mean value of neighbouring pixels, and η a threshold separating OBJ from unclassified pixels. In this thesis, the threshold has been taken over from Geiß et al. (2015c) and is defined as the range [-10; +10]. This means that all pixels differing more than +/- 10 from the mean value of the neighbouring pixels stay unclassified and all pixels within this range get classified as OBJ. The process of assessing similarity gets repeated during each iteration until a stable situation is reached, where no more potOBJ get classified as OBJ pixels.

In a normal RMPF approach, all remaining unclassified pixels get labelled as BE pixels. But this method most likely delivers insufficient results. If building objects have irregular roof surfaces or local variations of elevation occur, the RPMF may not capture all OBJ pixels. This happens especially with low thresholds for the similarity constraint (equation 8), which leads to potOBJ not getting recognized as OBJ but instead getting classified as BE pixels (=error of commission). This outcome will lead to partially eliminated building features in the final nDSM (Geiß et al. 2015c, 4351ff.).

Step 3: Postclassification with selective object-based voting

To lower these errors Geiß et al. (2015) introduced a postclassification processing scheme based on the concept of object-based image analysis referred to as OBIA. This method builds on older segmentation, edge-extraction, feature extraction and classification concepts that have been used in image analysis based on remotely sensed data for decades (e.g. Ketting & Landgrebe 1976; Pal & Pal 1993; Baltsavias 2004). Instead of analysing the image pixel-by-pixel (as it is the case in step 1) and 2) of Figure 9), OBIA works with image segmentation, which provides the building blocks (possible are also fuzzy objects or fields). These segments are regions generated by one or more criteria of homogeneity. They have additional spectral information compared to single pixels (e.g. mean values per band) and additional spatial information for objects (Blaschke 2010, 2f.). Geiß et al. (2015c) refer to this concept as *RPMF with selective object-based voting* (RPMF-SOBV). The OBIA method is used as a postclassification procedure (Figure 9 step 3)) for the output of the RPMF (Figure 9 step 2); Geiß et al. 2015c, 4352).

The postclassification process is schematically shown in Figure 12. First the pnDSM generated with B_{max} (= resulting surface of the RPMF in step 2)) gets divided into homogeneous image segments. Out of these segments, only the ones containing OBJ and unclassified pixels are selected. Finally, all pixels in the selected segments get labelled according to the maximum class probability in the specific segment (Geiß et al. 2015c, 4352).

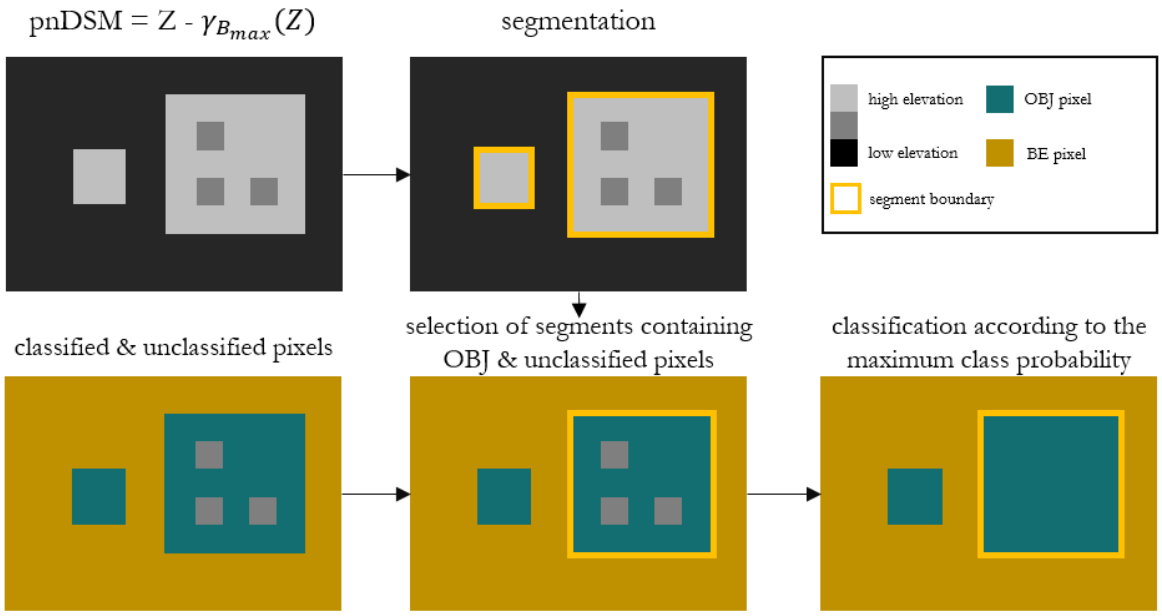

Figure 12: Schematic representation of the postclassification procedure. First step is the segmentation of the preliminary nDSM (normalised Digital Surface Model) into homogeneous segments. Consequently, only segments containing OBJ (nonground object) pixels and unclassified pixels are selected. According to the maximum class probability the unclassified pixels get classified as OBJ or BE (bare earth; own Figure recreated after Geiß et al. 2015c, 4352).

To ensure that all objects are included, the surface generated with B_{max} is used for the segmentation process (see step 1) in Figure 9: opening operation with B_{max} only excludes BE pixels). The goal of this procedure is the delineation of the building footprints, which are homogeneous regarding their response in the pnDSM surface. This analysis, a multiresolution segmentation algorithm implemented in the software environment *eCognition* is applied to the filtered surface to delineate the building footprints. Similar to many other region-growing algorithms, it is necessary to define control parameters. They are set by the user regarding spectral and geometrical characteristics to achieve maximum allowable heterogeneity between segments. Therefore, a scale factor, which is composed of grayscale-value and shape heterogeneity (shape consisting of smoothness and compactness of the segment boundaries), is utilised, with values between zero and one: $h_{colour} \in [0, ..., 1]$ and $h_{shape} \in [0, \ldots, 1]$, where $h_{shape} = 1 - h_{colour}$ consisting of h_{smooth} and $h_{cpmpact}$, where $h_{smooth} = 1 - h_{cpmpact}$ (Geiß et al. 2015c, 4352f.).

In this thesis, more emphasis is placed on shape heterogeneity when selecting the parameters (according to the recommendation of Geiß et al. 2015c). Man-made features like buildings show expressive shape and size properties compared to natural features. It is therefore necessary to define a higher weight for shape and thus a lower weight for grayscale-value: $h_{shape} = 1 - h_{colour}$ leads to $h_{shape} = 0.7$ when h_{colour} is set with 0.3. The higher the shape value, the lower the influence of colour on the segmentation. To maintain the influence of shape, $h_{compact}$ and h_{shape} both get set equal with 0.5 (Geiß et al. 2015c, 4353; Geiß & Taubenböck 2015, 2338). These parameters lead to a scale factor of 7.

Based on the previously defined threshold, the algorithm first compares neighbouring pixels and merges them, if similarity is found, into one segment. Iteratively, parts of the resulting areas are merged, as well (Geiß et al. 2015c, 4352f.; Espindola et al. 2006, 3).

In general, low values for this threshold lead to small segments because the fusion of adjacent pixels/segments is very strict with a small scale parameter. In contrast, larger values result in bigger segments because the merging is less restrictive (Geiß et al. 2015c, 4352f.; Espindola et al. 2006, 3). When developing this approach Geiß et al. (2015c) tested different scale factors and have identified *7* as the value leading to optimal segmentation. To determine this value, they applied the segmentation algorithm to the pnDSM with different scale parameters creating different segmentation layers. To identify the optimal segmentation layer, which maximizes intrasegment homogeneity and intersegment heterogeneity, an objective function recommended by Epindola et al. (2006) has been calculated based on the *intrasegment variance* σ^2 and *Moran's I*. The measure for internal homogeneity (= intrasegment variance σ^2) is defined as (Epindola et al. 2006, 3)

$$\sigma^2 = \frac{\sum_{i=1}^{n} a_i \sigma^2}{\sum_{i=1}^{n} a_i} \quad \textbf{(Eq.9)}$$

where a_i corresponds to area and $\sigma^2{}_i$ to the *intrasegment variance* of segment *i*. This measure represents the weighted average with the areas of each region being the weights. Low values for the *intrasegment variance* indicate homogeneity for each region. To measure the heterogeneity between segments *Moran's I* autocorrelation index has been utilised. Spatial autocorrelation, a property of spatial data, is represented in the data as similar values for a variable occur in nearby locations, which leads to spatial clusters. The algorithm calculates the mean gray value in each region and specifies all neighbouring regions. The index is defined as (Epindola et al. 2006, 3; Geiß et al. 2015c, 4353)

$$I = \frac{n \sum_{i=1}^{n} \sum_{j=1}^{n} w_{ij} \left(\mu_{seg}(\Delta Z)_i - \mu(\Delta Z)\right)\left(\mu_{seg}(\Delta Z)_j - \mu(\Delta Z)\right)}{\left(\sum_{i=1}^{n} \left(\mu_{seg}(\Delta Z)_i - \mu(\Delta Z)\right)^2\right)\left(\sum_i^n \sum_j^n w_{ij}\right)} \quad \textbf{(Eq.10)}$$

where n is the number of segments indexed by *i* and *j*, $\mu_{seg}(\Delta Z)$ represents the mean pnDSM value of one segment and $\mu(\Delta Z)$ the mean pnDSM value for all segments. Spatial adjacency between segment *i* and *j* gets measured by the weight w_{ij} : adjacent regions $w_{ij} = 1$, otherwise $w_{ij} = 0$. Small values for *Moran's I* suggest a low spatial autocorrelation, meaning the adjacent segments are statistically different and thus representing heterogeneity. Both parameters, *intrasegment variance* and *Moran's I*, have been combined in the objective function (Geiß et al. 2015c, 4353)

$$F(\sigma^2, I) = \frac{{\sigma^2}_{max} - \sigma^2}{{\sigma^2}_{max} - {\sigma^2}_{min}} + \frac{I_{max} - I}{I_{max} - I_{min}}, \quad \textbf{(Eq.11)}$$

which sums up normalized values of σ^2 and *I* to calculate the statistical indicator for optimal segmentation represented by the maximum value of *F* (Geiß et al. 2015c, 4353). Based on the calculations of Geiß et al. (2015c) the value for optimal segmentation is taken over in the context of this thesis for the segmentation of the pnDSM with B_{max}. Out of all segments, only those containing OBJ and unclassified pixels are selected for further classification (see Figure 12). In order to finally classify the former as OBJ or BE, a probability function is maximized (Geiß et al. 2015c, 4353):

$$L(p) = \arg\max_{v \in L}(P_{p,v}) \quad \textbf{(Eq.12)}$$

where *L* represents the labelling space for pixels either 'OBJ' or 'BE' and *L(p)* the final label of pixel *p*. $P_{p,v}$ returns the probability with which pixel *p* belongs to class *v*. This is based on the segment probability (Geiß et al. 2015c, 4353):

$$P_{s,v} = \frac{1}{N_s} \sum_{b \in s} \tau\,(C(b) = v) \qquad \textbf{(Eq.13)}$$

where τ acts as indicator representing the number of times that the pixels *b* within a segment *s* feature the class label *v*. N_s represents the number of pixels in the segment *s* (Geiß et al. 2015c, 4353). To conclude, depending on the probability of one segment determined by the number of pixels in the different classes (low elevation = BE, high elevation = OBJ), the unclassified pixels get categorized as OBJ or BE. All remaining unclassified pixels after the postclassification procedure get labelled as BE.

Step 4: Interpolation of the DTM and nDSM calculation

In the last step shown in Figure 9 the nDSM is created. In the first instance after the final classification in BE and OBJ pixels, all BE pixels (classified in step 1) and 3) in Figure 9) get extracted and all individual parts of each city are merged into a mosaic again in order to contain one coherent layer per urban region. Consequently, the interpolation of the DTM is carried out. Interpolation refers to the prediction of data values at locations where no samples are available (Burrough et al. 2015, 147). In this thesis, the aim is the prediction of the bare earth altitude for any pixel classified as OBJ. In order not to change the height values of the classified BE pixels, an interpolation method, which estimates a value that is equal to the actual value at a sampled location, is used. In addition, interpolation should only take place between values of sampled locations (Geiß et al. 2015c, 4352). For these reasons, the *inverse distance weighting* (IDW) is selected, a mechanical, deterministic interpolation method (Hengl 2009, 11). It assumes that the value of an unsampled point is a distance-weighted average of the data points within the neighbourhood of the point with unknown value (Burrough et al. 2015, 163). Thereby the value of a target variable *h* at a location s_0 (= unknown BE altitude values in a 100km radius around the city center for the USA and a 40km radius around the city center for Germany) is determined as the weighted average of the samples (= classified BE pixels) in the neighbourhood (Hengl 2009, 12):

$$h(s_0) = \sum_{i=1}^{n} \lambda_i\,(s_0) * h(s_i) \qquad \textbf{(Eq.14)}$$

where $h(s_0)$ is the unknown altitude value for the target variable, λ_i the weighting of a sampled variable (= known altitude value), $h(s_i)$ a known altitude value in the neighbourhood of s_0 and n represents the number of adjacent sampled variables (Hengl 2009, 12). The weighting λ_i for the neighbour *i* is determined by the following relationship (Webster & Oliver 2014, 40):

$$\lambda_i = \frac{1}{|s_i - s_0|^{\beta}} \quad \textbf{(Eq.15)}$$

where s_i is a known altitude value and s_0 an unknown altitude value. β is a coefficient for adjusting the weighting and is always larger than zero (Webster & Oliver 2014, 40). The name of the method is derived from this equation. The inverse distances from all known altitude values to new altitude values $(s_i\text{-}s_0)$ are of central importance for IDW. The coefficient is chosen arbitrarily and is used to adjust the weighting. Known height values close to the target value receive a higher weighting than those at a greater distance (Hengl 2009, 13; Webster & Oliver 2007, 40). A common value for β is '2', so that the data is inversely weighted over the square of the distance $s_i\text{-}s_0$ (Webster & Oliver 2007, 40). This value is also used in this thesis. The difference between smaller β values, e.g. '0.5', and larger β values, e.g. '10', is defined as the height of consideration of data points at a greater distance from the target variable, which is less pronounced with larger β values than with smaller β values (Hengl 2009, 13).

The result of the interpolation is the DTM, which is generated for each city under investigation. It shows the height of the bare earth without objects above ground. Subsequently the DTM is subtracted from the TDX DSM, which shows the height with objects above ground. The result is the final nDSM showing only the height of the objects above ground (see Figure 9 step 4)). Exemplarily the final nDSM is shown for Portland, Oregon (a) and Hanover (b) in Figure 13.

Figure 13: Final nDSM (normalised Digital Surface Model) of Portland (a) and Hanover (b). The nDSM solely reflects the height of objects above ground (own Figure).

2.3.3.2 Urban Mass Concentration generation

All methodological explanations under 2.3.3.2 refer to steps 2-5 in Figure 6, which follow the nDSM processing. After the final nDSMs are calculated (see chapter 2.3.3.1) for each study region, the next step is the intersection of the nDSM with the GUF (see Figure 6 step 2)). This is necessary to exclude all non-urban pixels. In the GUF-layer all non-urban pixels have the value '0' and all urban pixels the value '1'. A multiplication with this layer therefore leads to the desired exclusion. Figure 14 shows the result of this intersection exemplary for the cities of Portland (a) and Hanover (b). In comparison with Figure 13, it becomes clear that the approach led to the urban structures now being clearly recognisable.

After that, the urban structures, i.e. the nDSM masked with the GUF, are blended with the NDVI-layer to exclude urban vegetation (see Figure 6 step 3)). All pixels with an NDVI value above 0.3 (= threshold between active and non-active vegetation) are considered as zero in the further calculations. In addition, during this step the spatial resolution is reduced from originally 12m (depending on the position in the global TDX DSM coverage) to 10m. This can be explained by the spatial resolution of the Sentinel-2 images, the basic data for the index, which is 10m. By blending the two layers - nDSM-layer containing only urban structures and NDVI-layer - the pixel size is reduced to 10m. Therefore, the area of one pixel corresponds to $100m^2$ in the following steps. Figure 15 shows the intersection with the NDVI exemplarily for Portland (a) and Hanover (b). The vegetation areas are still included (grey background) to illustrate the effect of the NDVI-nDSM-masking. The chart reveals that many additional pixels get excluded.

The outcome is further overlaid with a grid of 1km x 1km size of the individual grid units (see Figure 6 step 4)). The single cells represent the units for the processing of the UMCs, as already explained in chapter 2.3.1. Figure 16 displays the grid coverage exemplarily for Portland (a) and Hanover (b).

Finally, the volume within each grid cell, which corresponds to the UMC, is calculated (see Figure 6 step 5)). In order to generate the volume per grid unit, the volume per pixel must be calculated in a previous step. This is done by multiplying the height of the nDSM [m] with the area of one pixel [m^2]. By summing up the volume of each pixel within a grid cell, the volume per grid cell is calculated subsequently. Thus, the result of this calculation corresponds to the UMCs per grid cell. They represent the outcome of the first part of this thesis and are presented in chapter 3.1.

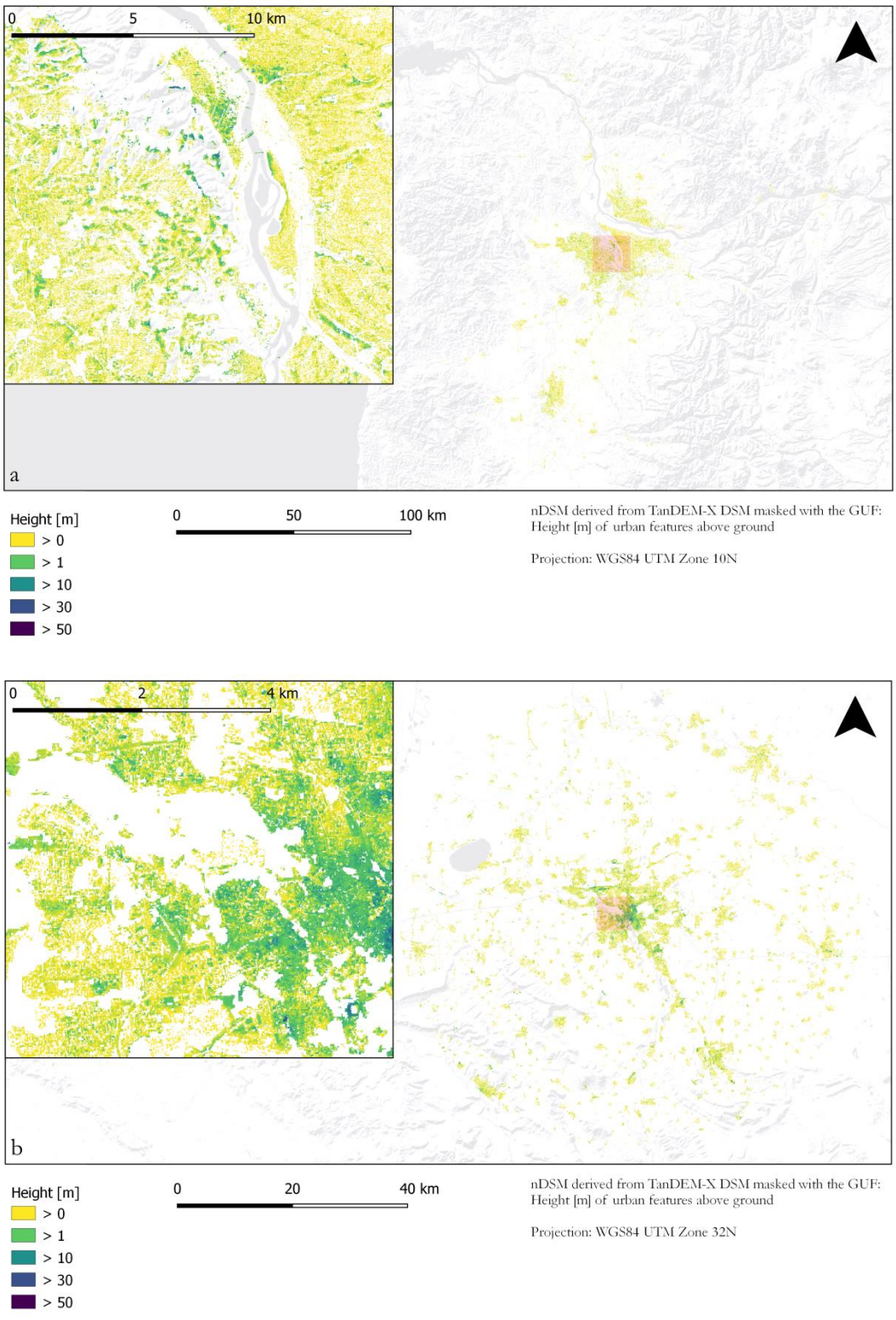

Figure 14: Result of the intersection of the nDSM (normalised Digital Surface Model) with the GUF-layer (Global Urban Footprint) displayed for Portland (a) and Hanover (b). Only urban structures are included (own Figure).

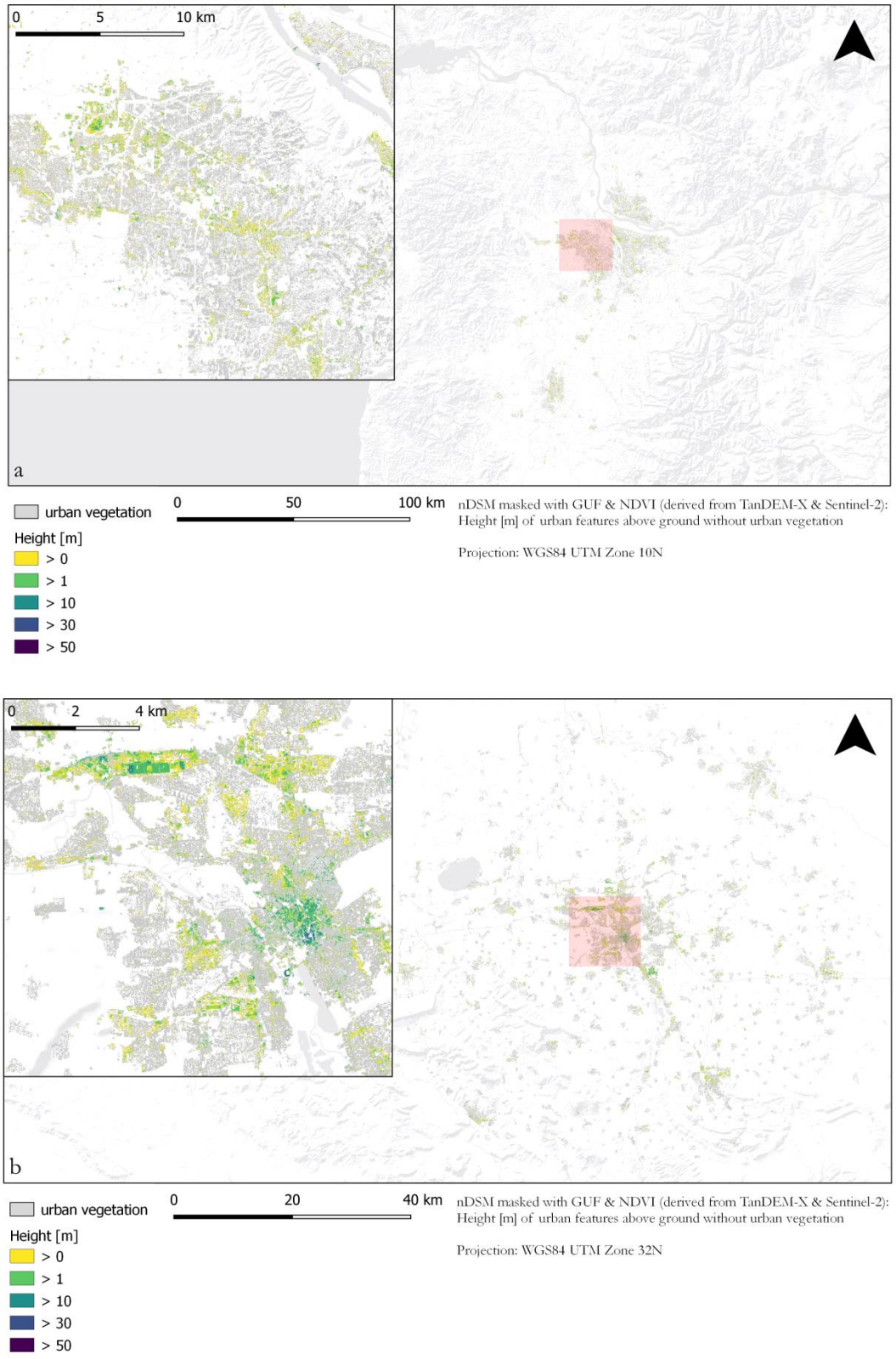

Figure 15: Result of the intersection of the nDSM (normalised Digital Surface Model), already only containing urban structures, with the NDVI. The outcome, here exemplarily shown for Portland (a) and Hanover (b), reveals that the NDVI-masking leads to the exclusion of many additional pixels compared to the GUF-masking (Global Urban Footprint) shown in Figure 14 (own Figure).

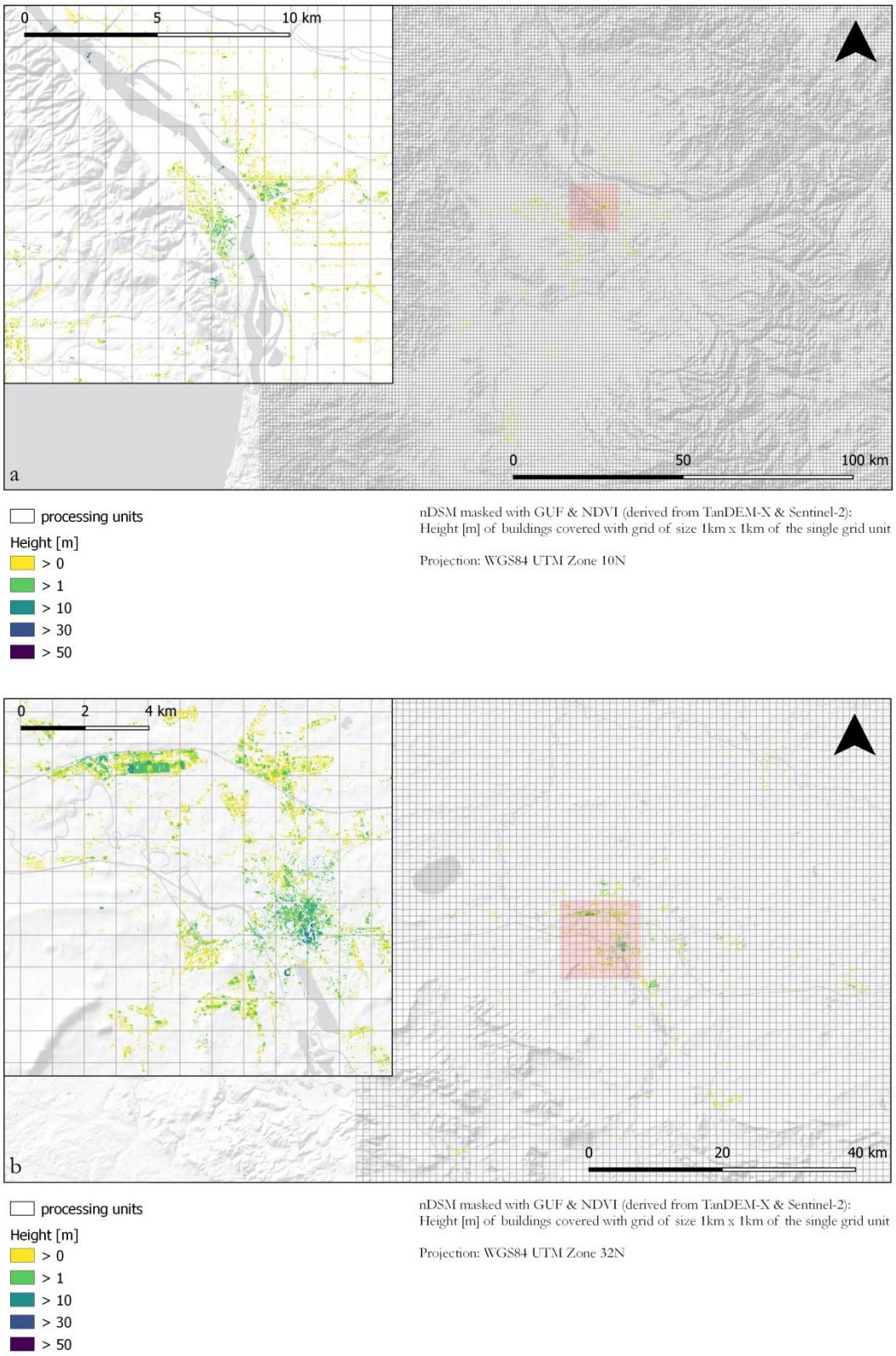

Figure 16: nDSM (normalised Digital Surface Model) containing only building features overlaid by the processing grid with a 1km x 1km size of the single grid unit. Here exemplarily shown for Portland (a) and Hanover (b; own Figure).

2.3.4 Validation

In order to validate the UMC estimates based on the TDX DSMs, the data is analysed spatially and non-spatially. First, a non-spatial simple linear regression is calculated to determine the functional relationship between the estimated UMCs and the validation data. In the following a validation approach with a spatial reference, in which the UMCs are examined more closely as a function of the distance to the city center, is carried out.

Before the individual validation steps can be carried out, the UMC based on the reference data, corresponding to the LoD1 building footprints, must be calculated. Unlike the volume calculation based on the TDX DSM data (see chapter 2.3.3.2), the generation of the UMCs based on the LoD1 building footprints (see chapter 2.3.2) uses the actual area of the building footprint polygons and not the size of the individual pixels. In addition, only those areas of the urban regions covered with reference data are validated. Therefore, only parts of the generated UMCs based on the TDX DSMs according to the described method in chapter 2.3.3.2 can be validated.

Simple linear regression

A simple linear regression analysis is a trend visualisation between two characteristics using a straight line, namely the *regression straight line*. By this, the functional relationship between a dependent variable (TDX DSM - UMC) and an independent variable (LoD1 - UMC) is described (Zimmermann-Janschitz 2014, 247f.; McKillup & Darby Dyar 2010, 205).

Regression is mathematically explained by the least squares method. The focus of this consideration is the sum of the distances between the data points and the searched straight line in the direction of the ordinate (y-axis). If the distances are minimized by squaring, the straight line adapts optimally to the data distribution and the relationship is represented in the best way possible. The distances between the straight line and the data points in the direction of the ordinate are regarded as errors, so-called residuals. According to this, the sum of all residuals is minimized by the least squares method (Zimmermann-Janschitz 2014, 248f.).

To describe the course of the regression straight line, only two statistics are needed. Parameter '*a*' is the value of the dependent variable *Y* when the independent variable $X = 0$ and parameter '*b*' presents the slope of the line (McKillup & Darby Dyar 2010, 205). In this process, the sum of the squared residuals serves as a measure of quality (Wollschläger 2017, 197). Formally the regression straight line is defined as (Zimmermann-Janschitz 2014, 252)

$$\mathrm{Y} = bX + a. \qquad \textbf{(Eq.16)}$$

With increasing slope, the relationship between the dependent and independent variable becomes stronger (Zimmermann-Janschitz 2014, 254).

On the basis of linear regression, it is not yet possible to assess the approximation quality, even if an optical assessment provides a first clue. Therefore, the quality criterion of linear regression, the *coefficient of determination* (R^2), is additionally used. It is defined as (Zimmermann-Janschitz 2014, 260f.)

$$R^2 = \frac{\frac{\sum_{i=1}^{n}(\hat{y}_i - \bar{y})^2}{n}}{\frac{\sum_{i=1}^{n}(y_i - \bar{y})^2}{n}} = \frac{s_{\hat{Y}}^2}{s_y^2} \qquad \textbf{(Eq.17)}$$

where *ŷ* represents a value *i* estimated by X (see equation 16), *y* is a dependent value *i* (= TDX DSM UMC at point *i*) and $\bar{y}$ constitutes the arithmetic mean. $s_{\hat{Y}}^2$ further represents the scattering of the estimated values *ŷ* (= explained variation) and s_y^2 the scattering of the dependent variable *y* (= total variation). By putting both variances in relation, the coefficient of determination is calculated, which functions as the quality of the linear regression (Zimmermann-Janschitz 2014, 261). If the estimated values correspond to the real values (here: TDX DSM UMCs), R^2 can assume a maximum value of one. The residuals then take the value zero. With increasing deviation of the data from the regression straight line, R^2 decreases. In the case of no linear relation between the dependent and independent variable, R^2 is zero (Zimmermann-Janschitz 2014, 261f.; McKillup & Darby Dyar 2010, 217).

Distance-based validation

In order to include the spatial location of the grid cells in the investigation, a *spatial distance-based approach* is applied in the second part of the validation. Instead of comparing individual grid cell values, as it is the case for simple linear regression, sum values of grid cells at a certain distance from the city center are used. The definition of the center is similar to chapter 2.3.1 (= center in open source GIS) and the volume values per grid cell are summed up at intervals of 1km around each city's midpoint. This allows the UMCs to be validated depending on their distance to the city center in the study area. By adding a spatial characteristic to the validation, a broader statement can be made about the quality of the estimated volumes based on the TDX DSM data.

2.3.5 Polycentricity Analysis

The polycentricity analysis in the framework of this thesis is based on an approach developed by Taubenböck et al. (2017a). In order to systematically identify hUMC (high urban mass concentrations), which are interpreted as (sub-)centers, the scientists have tested different threshold methods on underlying 3D building models derived from Cartosat-1 DSMs. The investigated possible threshold strategies are two *single-density threshold* approaches and one *distance-based, relative threshold* approach (Taubenböck et al. 2017a, 44f.)

For the single-density approaches, one cut-off value is used for all study areas (= *global threshold*) or one cut-off value is utilized per investigated urban region (= *region-specific threshold*). In the distance-based method, the thresholds for identifying hUMCs depend on the location of each grid cell within the urban area. A ring model around the city center with bandwidths of 1km is applied and each grid cell is assigned to an individual ring. This is done by calculating the centroids of the grid cells and assigning them to the respective rings. By this the UMC values get classified into different rings in dependence of their distance to the city center. Subsequently, one cut-off value is calculated for each ring (=*distance-based, relative threshold*). The bandwidth of 1km is chosen, because high spatial accuracy shall be achieved (Taubenböck et al. 2017a, 45).

The cut-off values separating UMCs from hUMCs are defined as a certain standard deviation (SD) above the mean of the UMC values used in the study. Taubenböck et al. (2017a) tested different thresholds on each approach by systematically applying various SDs (1.0 – 2.5; Taubenböck et al. 2017a, 45f. & 49).

The researchers found that the single-density approaches (global & region-specific) tend to overestimate the inner city area, while the distance-based approach often does not find hUMCs near the inner city area, but identifies hUMCs in the periphery not identifiable with the single-density approaches. Therefore Taubenböck et al. (2017a) applied a combination of methods in order to identify both, the hUMCs in the city center and in peripheral areas - namely the region-specific and the distance-based approach. The global approach would also be conceivable instead of the region-specific one, but the latter is conceptually more like the distance-based approach as it allows to weight the UMCs of the cities individually. By combining the methods, the disadvantages of the individual approaches can be avoided. Furthermore, the scientists found that a SD of 1.3 above the mean identifies a number of (sub-)centers which may come closest to reality (Taubenböck et al. 2017a, 47ff.).

In summary, (sub-)centers or hUMCs within the UMCs (= result of chapter 2.3.3) are identified in the scope of this thesis once via the region-specific approach with a SD of 1.3 above the mean and once via the distance-based approach with a SD of 1.3 above the mean. After that, the results

of both methods get combined. In addition, adjacent grid cells identified as hUMCs get merged, since it is assumed that they belong to one center (Taubenböck et al. 2017a, 50).

The identification of the (sub-)centers is followed by an analysis in order to assess the degree of polycentricity. This is especially important because it is not possible to extrapolate polycentricity solely based on the count of detected (sub-)centers (Taubenböck et al. 2017a, 53). Moreover, it is necessary in order to make comparisons between 1) the cities within the USA and Germany and 2) between the cities of the USA and Germany.

Therefore, in a first step a *rank-size distribution* is calculated for the area (2D) and the volume (3D) of the (sub-)centers of each city. All existing area/volume values (same values are only used once) are sorted hierarchically, with the first rank being assigned to the largest area/volume value and the last rank *n* to the smallest area/volume value occurring in the respective urban region. Through the graphical representation of these hierarchies it is possible to interpret the degree of polycentricity. The main indicator to be considered in this regard is the slope of the rank size distribution. Its degree expresses the hierarchy of the decreasing patch sizes. The more pronounced the hierarchy, represented by a steep slope, the more likely a low degree of polycentricity is predominant. Additionally, relatively high area and volume values at rank one (= largest patch with the highest volume/area value) are more likely an indicator for a lower degree of polycentricity, than lower values with less pronounced differences to other ranks (Taubenböck et al. 2017a, 47 & 53).

In a second step the *largest patch index* (LPI) is calculated. The index represents the dominance of the largest hUMC regarding its area and volume value in comparison to the complete area/volume of hUMCs. It is defined as (Taubenböck et al. 2017a, 47)

$$LPI = \frac{hUMC_{\ max}}{hUMC_{total}} * 100 \qquad \textbf{(Eq.18)}$$

where $hUMC_{max}$ represents either the largest (sub-)center area or volume value and $hUMC_{total}$ shows the total area or volume covered by detected hUMCs/(sub-)centers. The result of the division gets multiplied by 100 in order to describe the share of the largest area/largest volume in the total quantity of (sub-)centers in percent. The larger the share, the more dominant is a center compared to the other identified centers.

Furthermore, other *non-site specific measures* - the mean size, mean volume, total area of hUMCs and the total volume of hUMCs - which are calculated as well during the analysis process allow to draw conclusions about the degree of polycentricity.

In general, although it may not be regarded as an universal rule, it is assumed that higher values for the non-site specific measures mean size, mean volume and total volume of hUMCs and a high dominance of the traditional center (here: center with the largest area and the highest volume) indicate a low degree of polycentricity. Whereas lower values of the non-site specific measures and the LPI express a higher degree of polycentricity (Taubenböck et al. 2017a, 53). In this thesis, however, greater emphasis is placed on the LPI values than on the non-site specific measures. The LPI values refer directly to the rank-size distribution in regard to dominant characteristics of the largest patch with the highest volume/area value. Therefore, a greater correlation between the rank-size distribution and the LPI values is assumed. The non-site specific measures, nevertheless, serve as support for a more precise analysis.

The analysis of polycentricity within the two countries is carried out by evaluating the rank-size distribution, the LPI and the non-site specific measures inside the certain radius around the city center - 100km radius in the USA and 40km radius in Germany.

In order to compare the polycentricity between the two countries, the data is mutually adapted beforehand. This means, that only the area within a 40km radius of the city center is considered when comparing polycentricity between the cities in the USA and in Germany. To do so, the rank-size distribution, the LPI and the non-site specific measures for the USA are calculated additionally only for the (sub-)centers within a 40km radius around the city center. Due to its large size, Atlanta is only included in the comparison within the Urban Area, whereas the remaining US cities still have data across the UA.

3 Results

In this chapter the results of the applied methodology (see chapter 2) are presented. Reference is first made to the morphological characterization to show the generated UMCs/km^2 (see chapter 3.1). Subsequently the outcome of the validation is displayed (see chapter 3.2), before the final polycentricity analysis is reviewed (see chapter 3.3).

In order to present the outcomes clearly, only two US and two German cities are introduced and compared. Portland and Austin have the largest coverage of validation data. Therefore, it was decided to look at these cities within this chapter more closely. In Germany, Hamburg and Hanover are shown as they are an example for a large and a medium-sized city. The remaining four cities Atlanta, Philadelphia, Berlin and Nuremberg and their associated results are featured in Appendix I (reference to chapter 3.1), Appendix II (reference to chapter 3.2) and Appendix III (reference to chapter 3.3).

3.1 Morphological Characterization

Figures 17 and 18 show the results of the morphological characterization for Portland (17a), Austin (17b), Hamburg (18a) and Hanover (18b). The scaling, representing the different UMC - classes in the Figures, is kept equal for all cities. Therefore, a comparison can be made between the different considered urban regions.

Figure 17 shows that the urban structure, in terms of volume per grid unit (= UMC), differs significantly between Portland and Austin. Especially the inner part of the investigation area, depicted in the upper left corner in Figure 17a and 17b, demonstrates that Austin only has a few cells with a volume value higher than 512,000m³. Besides, they are all connected in a cluster of adjacent pixels. In Portland on the contrary, comparatively more pixels are part of this class. Moreover, they seem to be more distributed. Based on these observations the metro area (here: central area of the examined expanse) of Portland is denser than the one of Austin. It is also interesting that the metro area of Austin seems to have, to some degree, a radial/axial development from the densest area (dark blue pixels) to less dense areas (yellow pixels) in the surroundings. Portland does not show this kind of development. The highest volumes per grid units have no clear delimitation, although a tendency of decreasing volumes towards the edge of the central area can also be observed.

Differences can also be deducted when considering the entire study area. In Portland, the urban structures extend from north to south in a broad stripe-like formation with scattered higher volume clusters. This formation is delimited by the terrain in the east and west, where no significant urban structures can be detected. In Austin, on the other hand, tendencies of an axial

development with high volumes connected in a star-shaped pattern can be identified. A denser urban stripe, which extends to the southern end of the study area, stands out.

At first glance, Figure 18, showing Hamburg (a) and Hanover (b), procures a relatively similar urban structure in terms of volume per unit. First, parts of the inner area of the investigated regions are examined more closely, visible in the upper left corner. A comparison indicates that the metro area of Hamburg seems to have higher volume values than the one of Hanover. While in Hamburg many pixels having volume value of more than 512,000m³ (dark blue pixels) are densely located in a cluster, Hanover only shows a few pixels in this class. By including the entire generated area, it becomes obvious that high volumes (dark blue and purple coloured pixels) in Hamburg occupy a larger part of the entire area compared to Hanover. Moreover, the surrounding areas of the dense concentrations of urban masses in Hamburg and Hanover are characterized by less dense urban structures (orange and yellow coloured pixels). To conclude, the study area of Hamburg appears to be characterised by higher urbanity. But given that Hamburg is a city with much more inhabitants than Hanover, this is also expectable (see chapter 2.1).

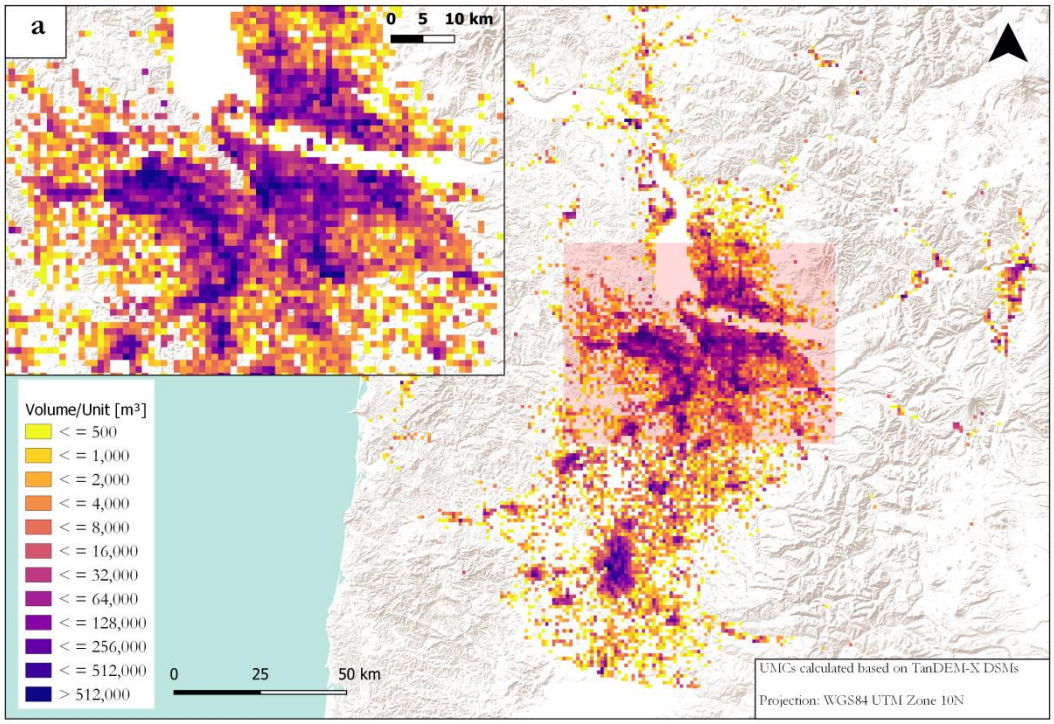

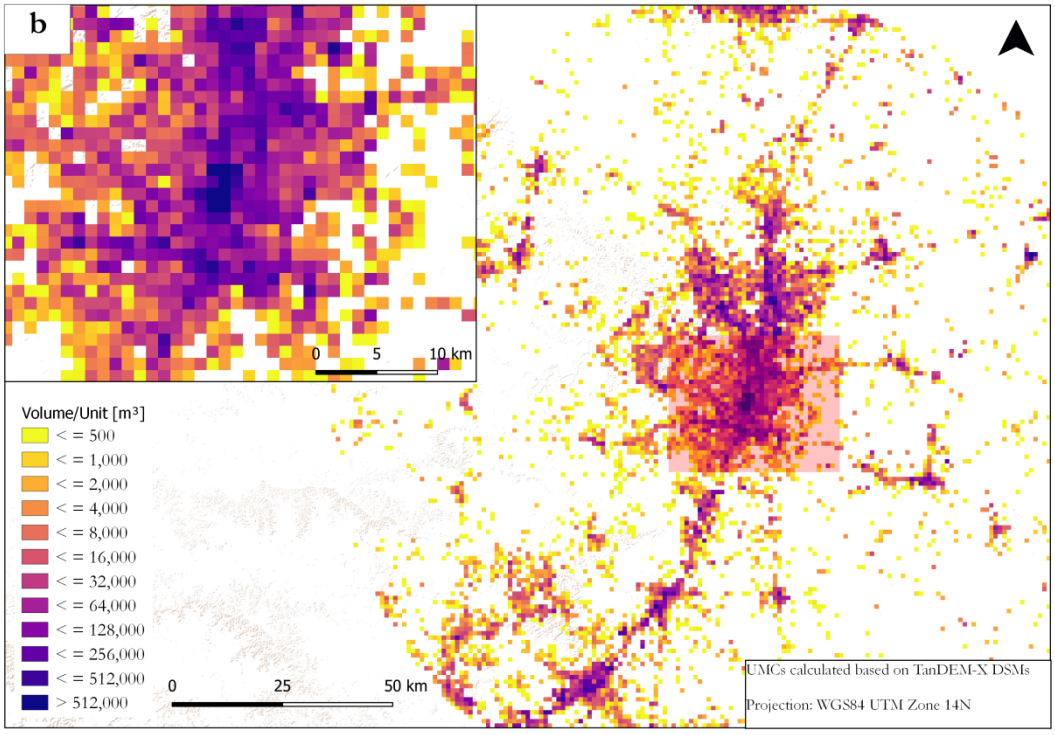

Figure 17: Generated UMC (urban mass concentration) in Portland (a) and Austin (b). The UMC corresponds to the volume per grid unit, which has a size of 1km x 1km (own Figure).

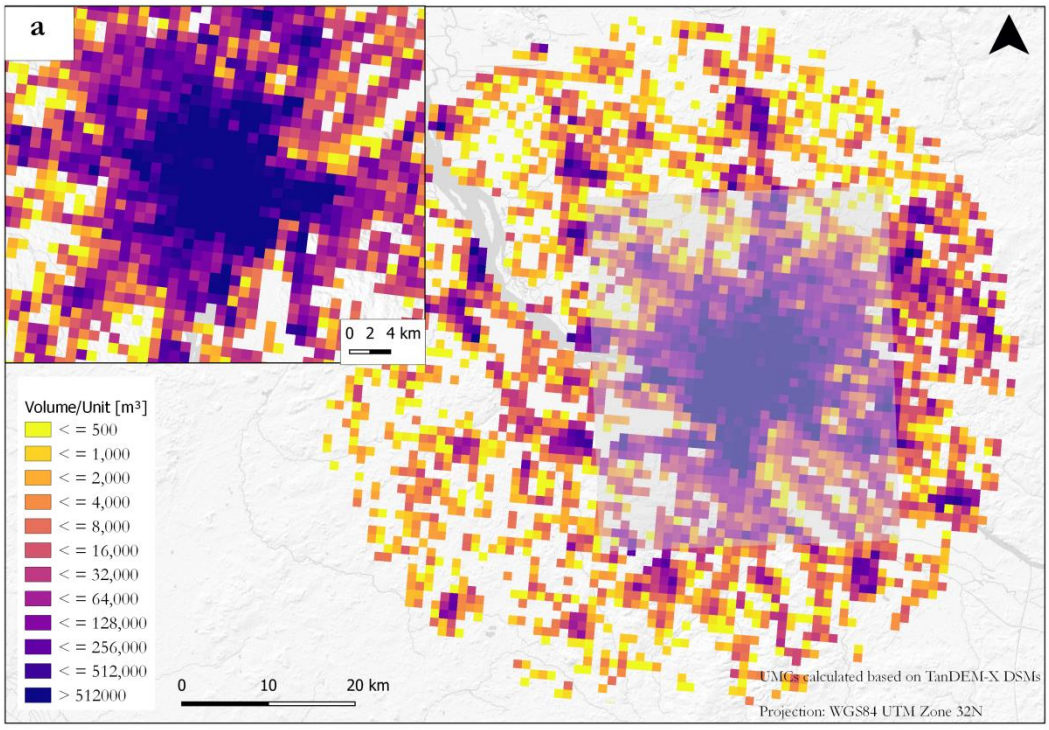

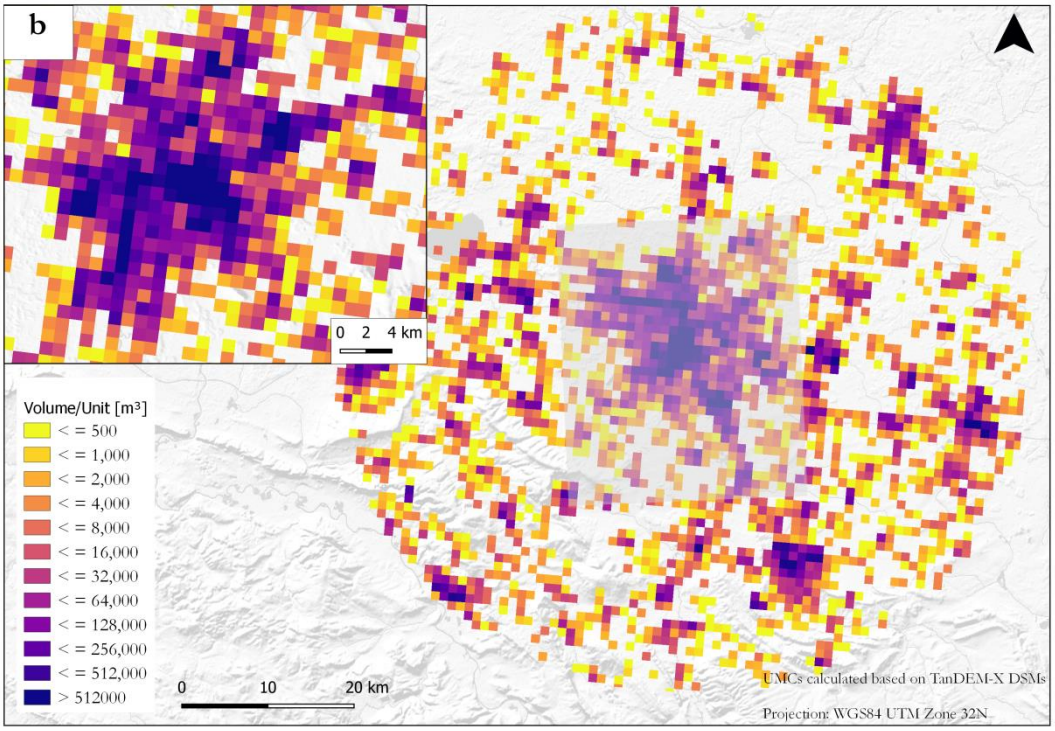

Figure 18: Generated UMC (urban mass concentration) in Hamburg (a) and Hanover (b). The UMC corresponds to the volume per grid unit, which has a size of 1km x 1km (own Figure).

3.2 Validation

Initially, the results of the simple linear regression are presented (additional overview of the following results are shown in Table 6). Subsequently the outcome of the distance-based validation approach is described.

As previously explained, it is pointed out once again that only the US cities are subjects for the validation. Moreover, validation is the only way to verify the quality of calculations and is therefore an important factor in any scientific work. Because of this, the simple linear regression results for Atlanta and Philadelphia are presented in addition to the ones of Portland and Austin to provide a larger scope.

Simple linear regression

Figure 19 shows the simple linear regression results for all four American cities. Based on the available validation data, different numbers of grid cells containing the UMCs are validated. The PBF (Portland Building Footprint) enables a simple linear regression with 2430 grid cells and their corresponding UMC values (Figure 19a). The highest UMC within the reference data, displayed on the x-axis, shows a value of over 2 million m³. Within the calculated UMCs based on the TDX DSM data the highest values are around 1.5 million m³. Furthermore, Figure 19a shows that the UMCs based on the LoD1 building footprints are mainly located in a cluster up to

1 million m³. In contrast, the values of the TDX DSM UMCs are primarily located up to 500,000m³. Overall, the TDX DSM UMCs are therefore below the UMCs shown by the validation data. The coefficient of determination has a value of 0.4589.

Austin, displayed in Figure 19b, has the largest coverage of validation data with the ABF (Austin Building Footprint). The validation is based on TDX DSM- and LoD1 building footprint-UMCs of 2807 grid cells. The highest UMCs of the reference data have values between 10 million m³ and 11.5 million m³ and the densest cluster is located up to approximately 4 million m³. In contrast, the highest UMCs based on the TDX DSM data have values between 800,000m³ and 850,000m³ and are most densely distributed up to 150,000m³. In summary, the volume difference between UMC values of LoD1 building footprint and TDX DSM data is more pronounced compared to Portland. However, the coefficient of determination is significantly higher than in Portland with a value of 0.6369.

Figure 19c presents the result of the regression for the city of Atlanta. With only 132 grid cells, the city has the scarcest coverage of validation data with the MBF (Microsoft Building Footprint). The highest UMC values of the MBF are situated around 13 million m³. However, they are only represented by a few grid cells. Most UMC values are located up to approximately 3 million m³. In the case of the calculated UMCs based on the TDX DSM data, the highest values lie between 7 million m³ and 8.5 million m³ and a cluster of values can be identified up to 2.5 million m³. In comparison to Portland and Austin, these identified volume values indicate a higher similarity between the TDX DSM UMCs and LoD1 building footprint UMCs. This trend is also reflected in the coefficient of determination, which is, with a value of 0.7233, higher than the ones calculated for Portland and Austin.

Philadelphia, shown in Figure 19d, is a special case. As can be seen in Appendix I 1, UMCs could only be calculated for about half of the area of the investigation expanse. The reason is an error in the raw data, i.e. the TDX DSMs underlying the area of examination. This error only became apparent in the course of the UMC generation. Although values are available, they are significantly below sea level and are thus incorrect. To confirm the error, the height values were compared with a SRTM (DSM data conducted by the *Shuttle Radar Topography Mission*) of the same area. Due to this limitation, only a small part of the originally available LoD1 building footprint data of the PHBF (Philadelphia Building Footprint) could be used. Nevertheless, with 272 grid cells a larger area compared to Atlanta could be validated. The highest volume values based on this data are located around 9.5 million m³. For the UMCs calculated with the TDX DSM data the highest values are situated around 1 million m³. A cluster of volume values, as it is the case for the other three US cities, cannot be identified in Philadelphia. This is also reflected in the coefficient of determination, which has a value of 0.3297. Therefore, in comparison to the other

three US cities, Philadelphia has the lowest value for the coefficient of determination.

To conclude, it can be stated that the TDX DSM UMCs are always below the volume values of the LoD1 building footprint data. This is also clearly shown by the mostly flat slopes of the regression lines.

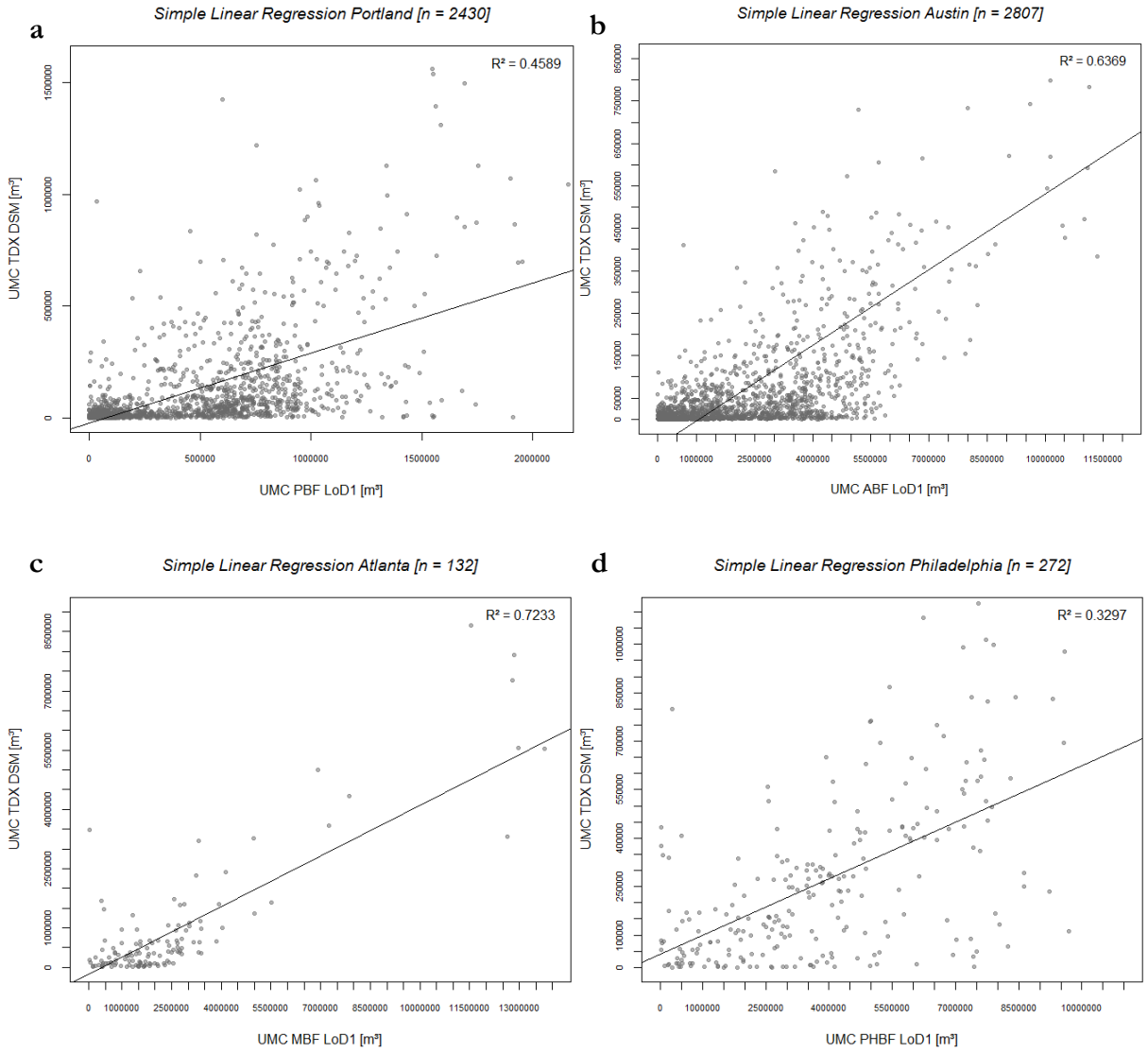

Figure 19: Representation of the simple linear regression for Portland (a), Austin (b), Atlanta (c) and Philadelphia (d). The x-axis shows the UMCs [m³] (urban mass concentrations) of the validation data and the y-axis the UMCs [m³] of the TanDEM-X DSM (Digital Surface Model) data. In addition, the coefficient of determination, making a statement about the quality of the regression, is indicated in each case (own Figure).

Table 6: Summary of the simple linear regression results calculated for the cities in the USA. The highest calculated UMCs (urban mass concentrations), the area, where most UMC values are located and the coefficient of determination are listed respectively per city and data source (own Table).

STUDY AREA	DATA	HIGHEST UMC [MILLION M³]	UMC CLUSTER [MILLION M³]	R^2
PORTLAND	PBF	2	up to 1	0.4589
	TDX DSM	1.5	up to 0.5	
AUSTIN	ABF	11.5	up to 4	0.6369
	TDX DSM	0.085	up to 0.15	
ATLANTA	MBF	13	up to 3	0.7233
	TDX DSM	8.5	up to 2.5	
PHILADELPHIA	PHBF	9.5	-	0.3297
	TDX DSM	1	-	

Distance-based validation

Figure 20 shows the UMCs (y-axis) within the coverage area with validation data as a function of distance to the city center (x-axis) for Portland (20a) and Austin (20b). The LoD1 building footprint data and their corresponding calculated UMCs, displayed in dark grey, and the TDX DSM data and their corresponding UMCs, displayed in light grey, indicate a significant difference regarding the height of the generated volumes. This again confirms the outcome of the simple linear regression. Atlanta and Philadelphia presented in Appendix II show similar results. However, if the summed-up volumes generated from the TDX DSMs and the LoD1 building footprint data are represented uniformly scaled in one diagram, the course of the TDX DSM UMCs cannot be interpreted correctly due to the occurring underestimation. For this reason, the TDX DSM UMCs are additionally displayed in the top right corner in the scale range determined by the volume range of these data. When comparing the progressions of the TDX DSM data, shown in the top right corner for each city, with those of the associated LoD1 building footprint data, it becomes apparent that the courses of the summed-up volumes resemble each other. In no case are the courses the same, but a similarity can be established.

In Portland, Figure 20a, it can be observed that the volumes first increase roughly and then decrease gradually with increasing distance to the city center. In Austin, Figure 20b, the course of the volumes based on the reference data is relatively uniform. Up to a distance of 28km from the center the sum volumes are above 100 million m³. A similar course can be identified for the TDX DSM data, where the total volume values are over 2 million m³ up to a distance of 28km. In both datasets low values can be observed starting from a distance of 34km compared to the areas closer to the city center. The similarity in the course of the TDX DSM and LoD1 building footprint data can also be seen in Atlanta and Philadelphia, Appendix II.

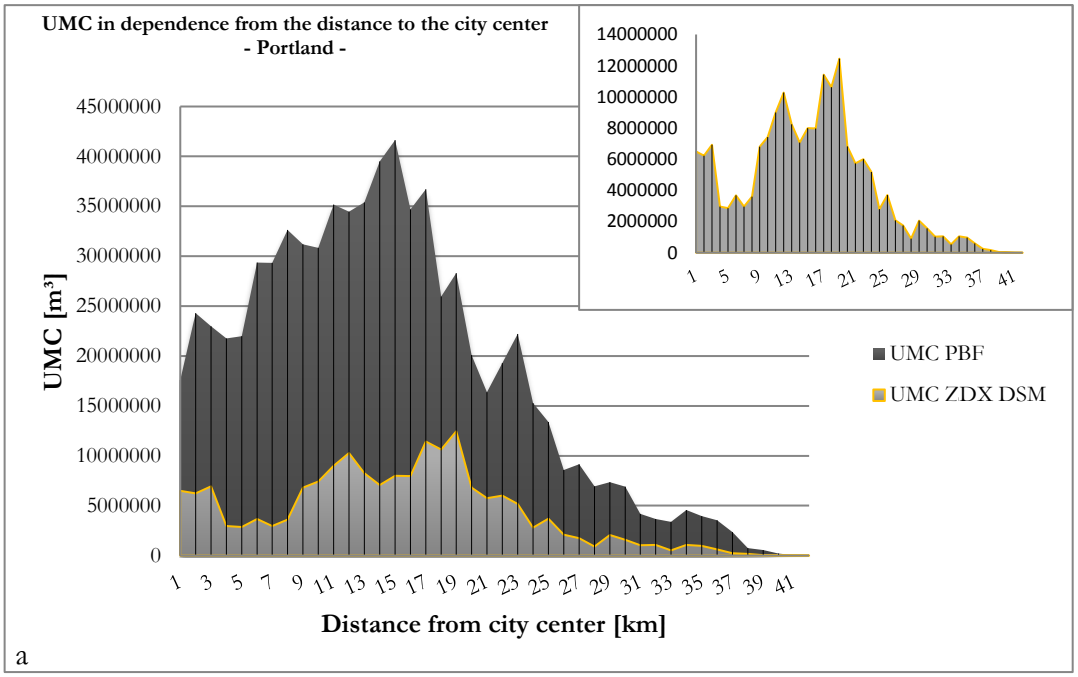

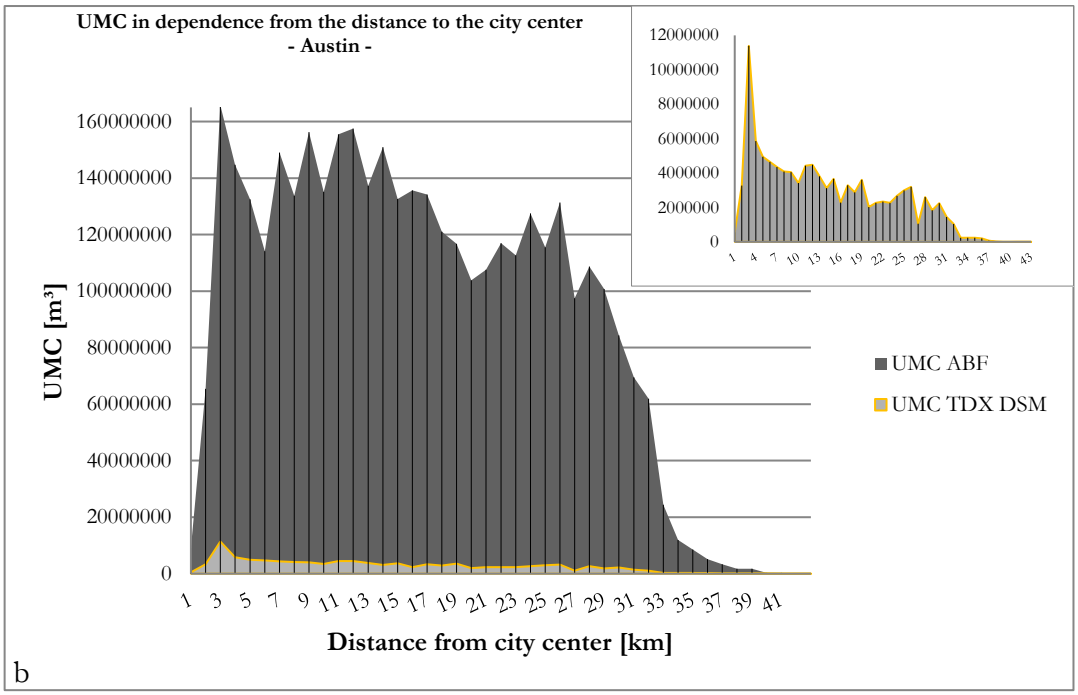

Figure 20: Representation of UMCs (urban mass concentrations) (x-axis) as a function of distance to the city center (y-axis) for Portland (a) and Austin (b). In intervals of one kilometre the volumes per grid cells are summed up. Therefore, the UMCs on the y-axis show the total volume per kilometre (own Figure).

3.3 Polycentricity Analysis

Within the scope of this chapter the results of the identification of the hUMCs (high urban mass concentrations), i.e. the (sub-)centers, are presented initially. Followed by this, the findings of the rank-size distribution and the calculation of the LPI (largest patch index) are displayed. As in the previous chapters (3.1, 3.2), only the output of the cities Portland, Austin, Hamburg and Hannover are introduced. The results of the remaining urban agglomerations are shown in Appendix III.

3.3.1 Detection of high urban mass concentrations

Figures 21, 22, 23 and 24 show the patterns of (sub-)centers for the city regions of Portland (21), Austin (22), Hamburg (23) and Hanover (24), which were detected using a combination of the region-specific and distance-based approach with UMCs exceeding a SD (standard deviation) of 1.3. At the top of each Figure the grid cells identified as hUMCs are shown with the classes region-specific (yellow), distance-based (red) or with a combination of both approaches (orange). In the lower part a holistic representation of the detected (sub-)centers is displayed. This visualisation allows a first assessment of the size ratio of the identified (sub-)centers (they are delimited by a boundary illustrated in black colour). In addition, the number of detected (sub-)centers is indicated in the upper right corner.

Figure 21 shows the city of Portland for which a total of 66 (sub-)centers were identified. With the region-specific approach, hUMCs could be detected mainly within the UA (Urban Area) near the city center. The distance-based approach, on the other hand, also identifies centers at a greater distance from the city center, which would remain hidden by applying solely the single-density threshold method. However, there are also many grid cells that were recognized by both approaches as hUMCs. In the bottom part of the Figure, in which the hUMCs are combined to (sub-)centers, it becomes clear that a large part of the UA was identified as a hUMC. A total of three comparatively large (sub-)centers were detected within the UA. Since the separation between the three runs along the course of the rivers Willamette and Columbia, a connection between these centers can be established as well. Because they are also close to the city center, it is assumed that these structures belong to the traditional center of the city. Outside the UA, the center structures are small to medium-sized and they occur mainly in the south of the UA. In comparison with an underlying optical satellite image in an open source GIS a significant correlation to major highways can be established.

Within Figure 22 the results of the center detection for the city of Austin are presented. With 68 detected (sub-)centers almost the same number as for Portland, could be identified in Austin. Furthermore, Austin also shows that the region-specific approach is mandatory to identify center

structures in a shorter distance to the city center, while numerous pixels in greater distance to the city center are only discovered by the distance-based approach. The majority of the identified hUMCs, however, except for the ones in close distance to the city center, were identified by both approaches. The bottom part shows, similar to Portland, that the largest detected (sub-)center corresponding to the dominant and traditional center is located within the UA. It extends from north to south through the UA in a rather longitudinal form. Moreover, a strip which spreads from the south-end of the UA, as a continuation of the dominant center, in a south-westerly direction to the end of the area under investigation is apparent. A correlation with a large highway connecting Austin with the even larger city of San Antonio can be established. In the case of Atlanta and Philadelphia, both shown in the Appendix (III 1 & III 2), 144 and 127 (sub-)centers could be identified. Thus, in these cities, more or less twice as many center structures could be detected in Atlanta and in Philadelphia, compared to the amount of centers identified in Austin and Portland.

In Atlanta a dominant center stands out from the other detected (sub-)centers. Within the UA it is located in a rather elongated shape from the southwest of the UA to the northeast of the UA. Nevertheless, compared to the other US cities, it covers only a comparatively small part of the UA. However, the UA of Atlanta in general is also much larger than the ones of Portland, Austin and Philadelphia. The comparison with an optical satellite images shows that the longitudinal form reproduces a large highway, with large building complexes (possible warehouses or production facilities) lined up at its edges. The well-known, large *Atlanta Hartsfield-Jackson International Airport* (City of Atlanta 2019) is also included in the dominant detected center at the southernmost end. In addition, numerous smaller center structures as well as some medium-sized ones were detected. Outside of the UA explicit one larger (sub-)center sticks out, which seems to be an extension of the dominant city center.

Due to the errors in the raw data, already described in chapter 3.2, hUMCs in Philadelphia were generated only for about half of the investigated area. The city center is also located in an area where no data is available. Therefore, the traditional center is not displayed correctly. Accordingly, it is not possible to describe it more precisely, let alone determine its dominance as it is the case for the other US cities. A few results, nevertheless, can be presented. Outside the UA in the north-western part of the study region some medium-sized center structures could be identified. These seem to be connected with the city center (even though only parts of it could be processed). The visual comparison shows that these are small cities (Reading, Allentown, Easton) connected by large highways to the city center of Philadelphia. Along these roads numerous smaller (sub-)centers are distributed.

The results for Hamburg and Hanover are similar to each other, as can be seen in Figures 23 and

24. The numbers of (sub-)centers detected are slightly lower than for Portland and Austin. In Hamburg 38 (sub-)centers could be identified and 49 in Hanover. This is also due to the fact that the processed area in Germany is smaller than in the USA. In these cities, too, the upper parts of the Figures show the importance of applying a regional-based approach in addition to the distance-based approach in order to detect the hUMCs near the city center. Furthermore, similar to the US cities, in the bottom part of the Figures 23 and 24 the dominance of a large (sub-)center within the UMZ (Urban Morphological Zone) can be established. Moreover, it is noticeable that the majority of (sub-)centers in Hamburg were identified north of the Elbe River and only with the distance-based approach. The direct assignment to a large road is more difficult than in the US cities. Correlations to road courses can be identified, but since Hamburg shows a higher level of infrastructural network (by comparison with an optical satellite image), there is no unambiguity as it is present in the two US cities. In Hanover, the (sub-)centers are distributed relatively evenly around the UMZ. Two medium-sized center structures stick out, besides the dominant, traditional center, in the southeast and northeast of the investigation area. The alignment with an underlying satellite image shows that they represent parts of the cities Hildesheim (southeast) and Celle (northeast). Particularly in Hildesheim, similarities with economic areas (large buildings, which could be warehouses or production facilities in terms of structure) can be found.

The number of detected (sub-)centers in Nuremberg and Berlin, shown in the Appendix (III 3 & III 4), is similar to the German cities Hamburg and Hanover. In Nuremberg 40 and in Berlin 43 center structures were identified. Berlin has a dominant center covering most of the UMZ. It is also noticeable that no center structures were detected in the northeast of the investigated area. But further medium-sized (sub-)centers are located in the southern, south-western and south-eastern part of the examined region. They mainly correspond with economic areas of smaller cities outside of Berlin (e.g. Mitterwalde or Ludwigsfelde). Parts of Potsdam were also detected as hUMC. Moreover, in contrast to the other cities investigated (except for Hamburg), it is striking that the (sub-)centers outside the UMZ could mainly only be identified using the distance-based approach. In Nuremberg almost the entire UMZ is classified as hUMC, which exemplifies the dominance of the traditional center. Further (sub-)centers were identified especially in the north of the UMZ, where an axial formation of center structures extends to the end of the investigated area. A correspondence with a large road can be established, on which parts of other cities in the region were detected (e.g. Erlangen, Fürth).

In summary, there is still a dominant center in every city investigated, regardless of the country, Germany or the USA. Portland is the only city, where more than one dominant center was identified. Due to the missing data this statement is not valid for Philadelphia.

Portland, Oregon, USA

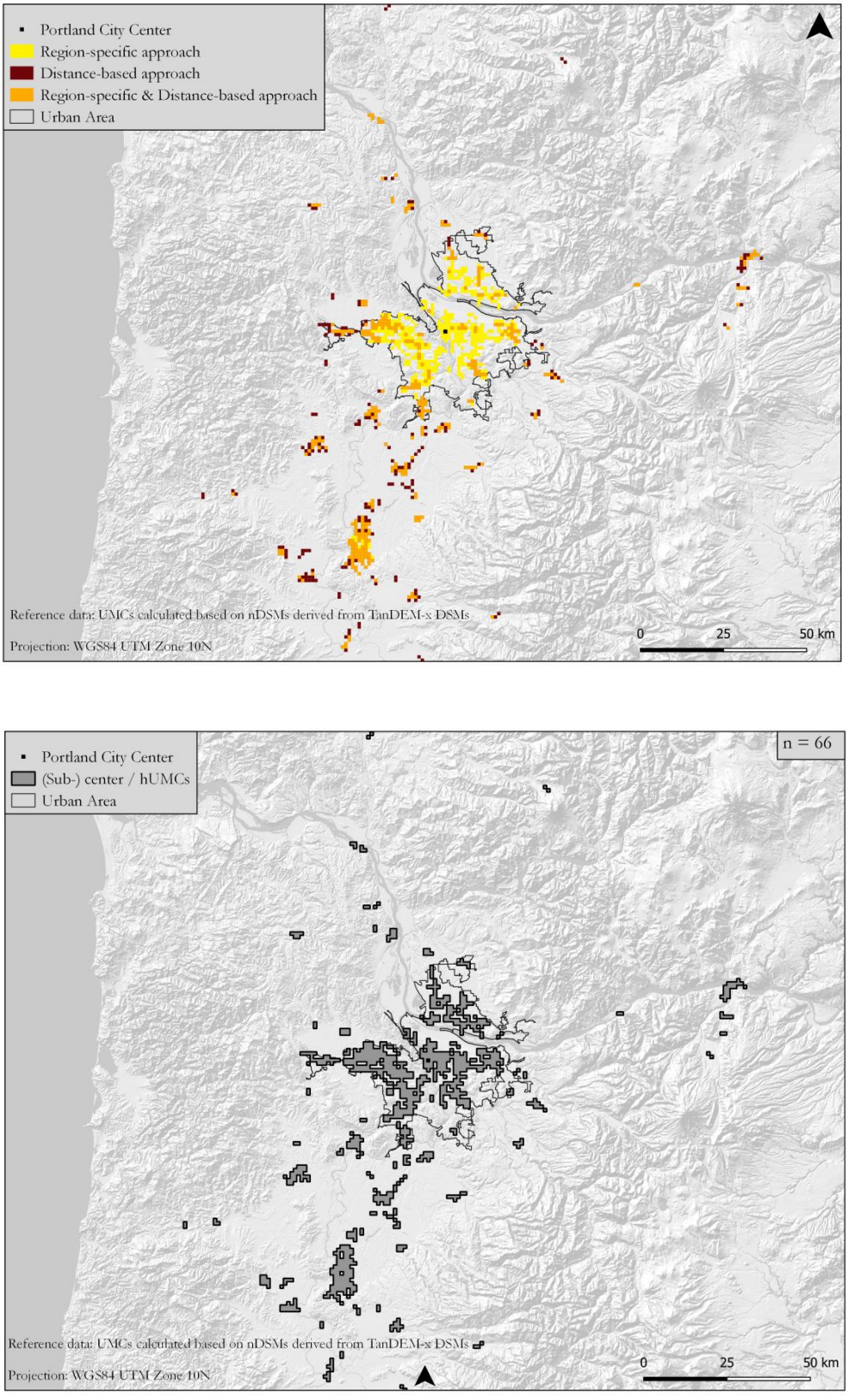

Figure 21: Detected (sub-)centers in Portland. Top: Representation of the hUMCs (high urban mass concentrations) assigned to the classes region-specific (yellow), distance-based (red) and region-specific & distance-based (orange), depending on the approach of detection. Bottom: Representation of all detected (sub-)centers. According to the definition, adjacent grid cells are merged (own Figure).

Austin, Texas, USA

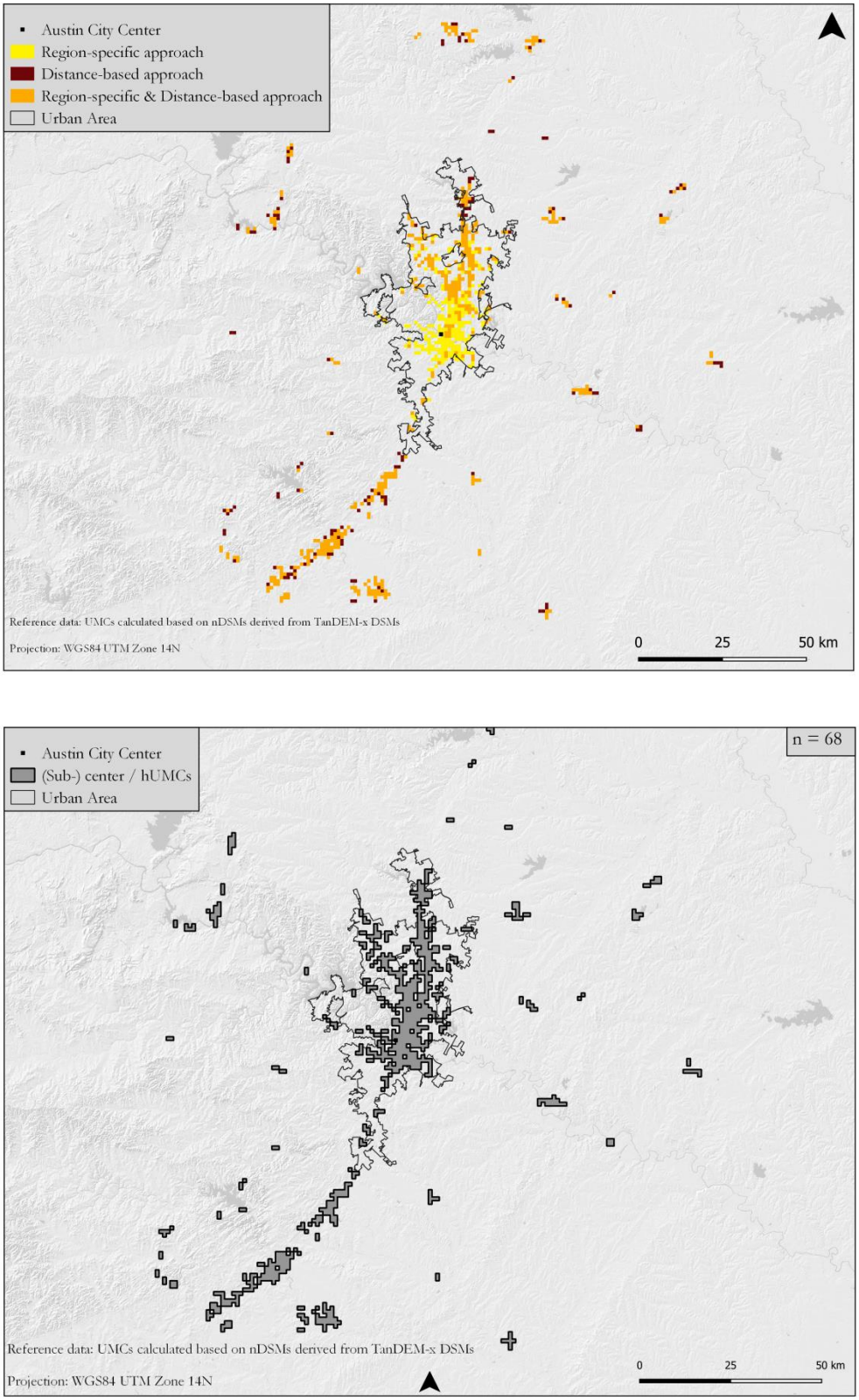

Figure 22: Detected (sub-)centers in Austin. Top: Representation of the hUMCs (high urban mass concentrations) assigned to the classes region-specific (yellow), distance-based (red) and region-specific & distance-based (orange), depending on the approach of detection. Bottom: Representation of all detected hUMCs. According to the definition, adjacent grid cells are merged (own Figure).

Hamburg, Germany

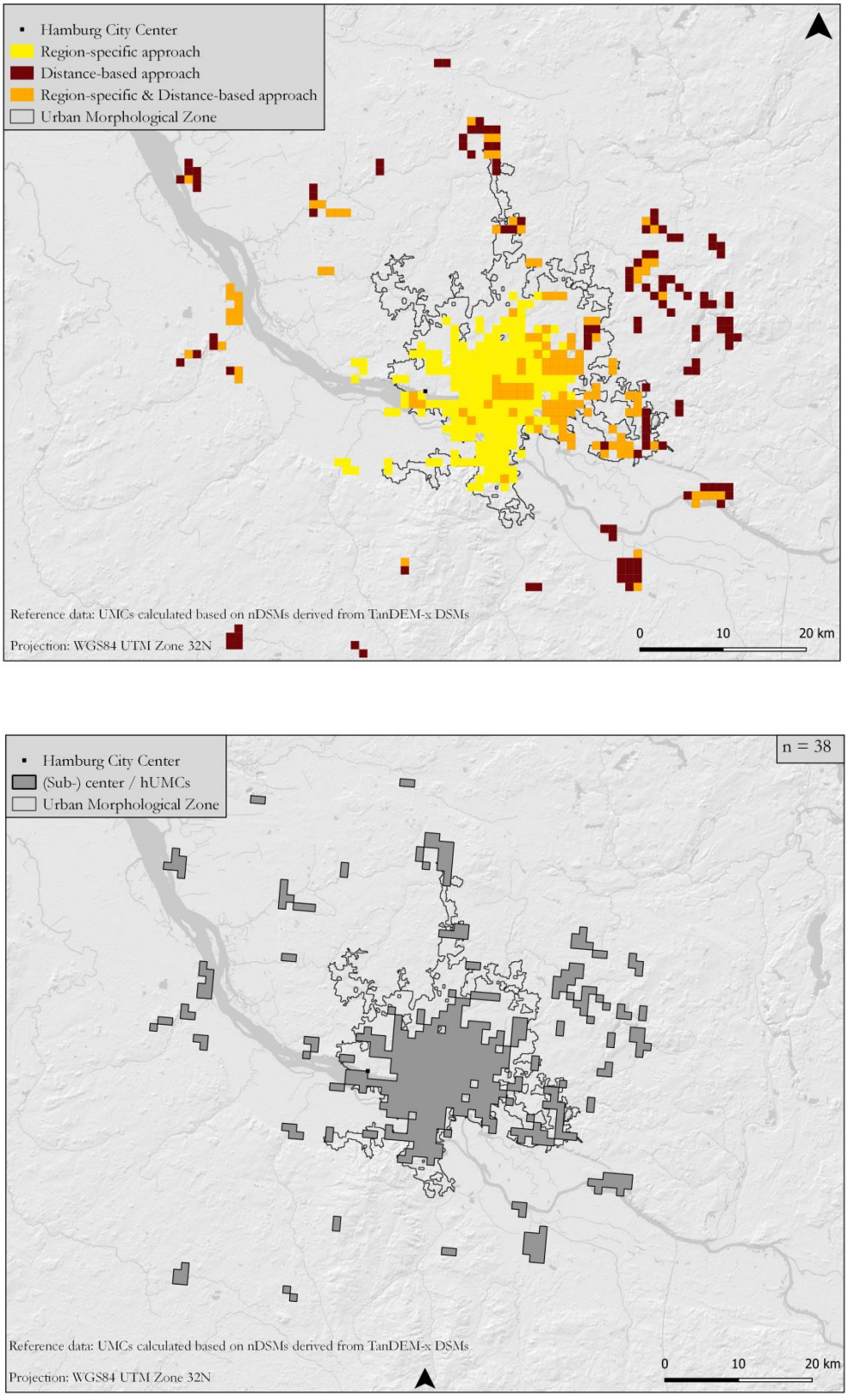

Figure 23: Detected (sub-)centers in Hamburg. Top: Representation of the hUMCs (high urban mass concentrations) assigned to the classes region-specific (yellow), distance-based (red) and region-specific & distance-based (orange), depending on the approach of detection. Bottom: Representation of all detected hUMCs. According to the definition, adjacent grid cells are merged (own Figure).

Hanover, Germany

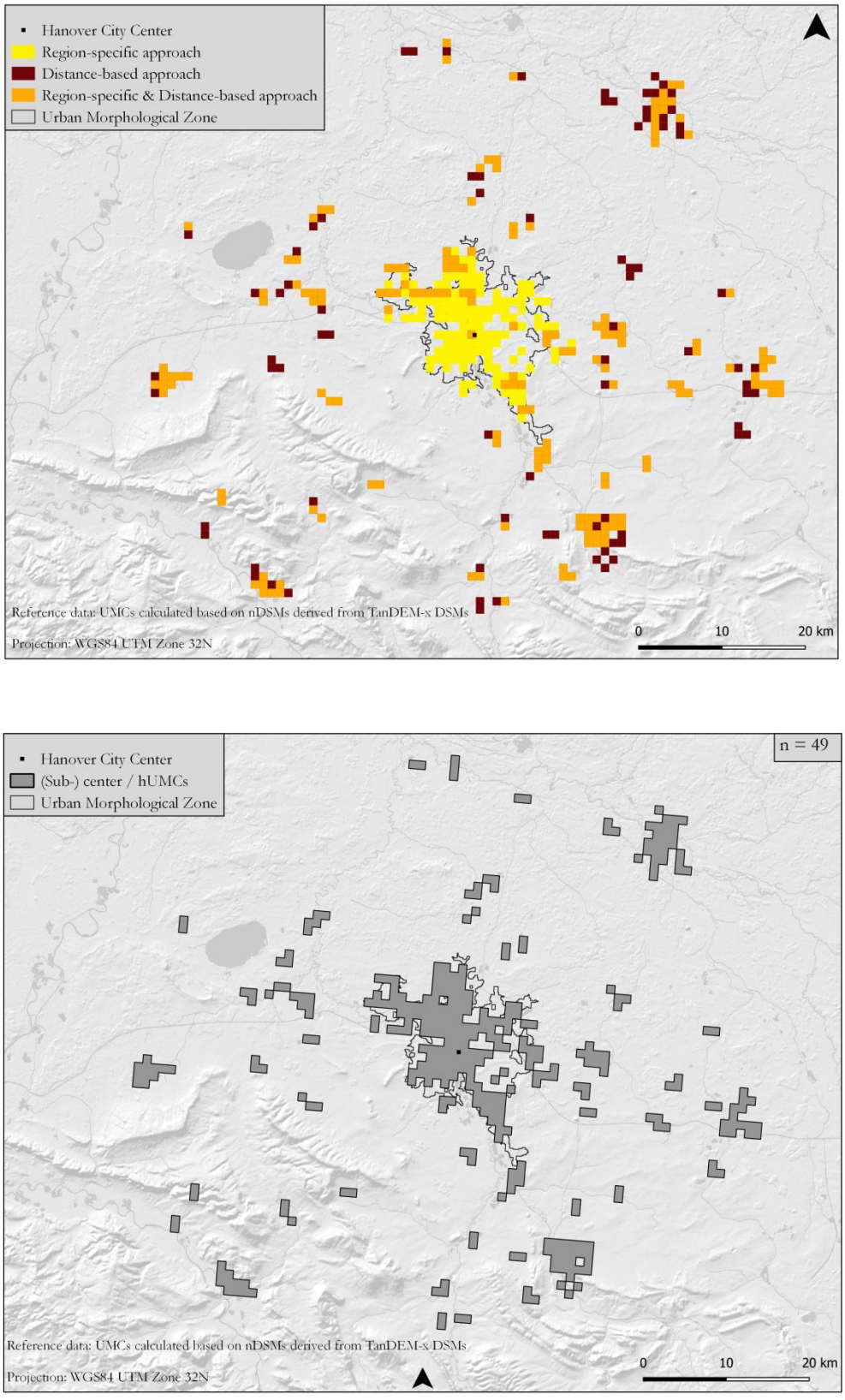

Figure 24: Detected (sub-)centers in Hanover. Top: Representation of the hUMCs (high urban mass concentrations) assigned to the classes region-specific (yellow), distance-based (red) and region-specific & distance-based (orange), depending on the approach of detection. Bottom: Representation of all detected hUMCs. According to the definition, adjacent grid cells are merged (own Figure).

3.3.2 Polycentricity in Germany

In this chapter the results of the rank-size distribution, the LPI and the non-site specific measures are introduced for Germany to analyse polycentricity in German cities.

Rank-size distribution

The outcome of the rank-size distribution is displayed in Figure 25. In the top row the distributions for the parameters *area* (left) and *volume* (right) are shown. In order to allow comparisons between cities, the area- and volume-values are presented with a logarithmic scaling since differences become more pronounced that way. In addition, the bottom row of Figure 25 shows the frequency of the occurring *area* ranks. For the parameter *volume* this representation is redundant because each volume value occurs only once. Therefore, the hierarchy of rank-sizes for the parameter *volume* (top right diagram) corresponds to the number of detected (sub-)centers in each city.

Considering the rank-sizes for the parameter *area* (top left), a heterogeneity of 13 (Hanover and Berlin) and 12 (Hamburg and Nuremberg) different sized centers could be identified. Furthermore, the *area* rank-size distribution also provides information about the actual 2D-size of the individual (sub-)centers. The diagram shows that rank one, which corresponds to the center structure with the highest area value and is seen as the traditional center, is in all four German cities larger than 100km². All (sub-)centers categorized between rank two and rank six have area values between 30km² and 10km². In rank seven and above area values less than 10km² are characteristic. This shows a distinctive hierarchy by decreasing patch sizes especially between rank one and rank two, which can be observed in all four German cities. This is an indicator of a strong dominance of the traditional center. Nevertheless, a ranking between the four German urban regions can be established regarding their degree of polycentricity. The most distinct hierarchy by decreasing patch sizes can be identified in Berlin and Hamburg. Even though, this represents only a slight difference to the hierarchy present in Nuremberg and Hanover. A similar statement can be made for the largest area values ranked on position one. The highest ranked areas are larger in Berlin and Hamburg compared to Hanover and Nuremberg, but the difference is not very pronounced. The inclusion of the rank-size distribution for the parameter *volume* provides additional information. Concerning the highest volume in each city, Hamburg, again, features the largest volume of one center with about 500,000,000m³. The largest center volume of Berlin, in contrast, is comparatively low with 10,000,000m³. This is striking because Hamburg and Berlin show a similar *area* rank-size distribution. Nuremberg owns the lowest volume value of a city center (maximum around 100,000m³). This is in line with the *area* ranking of the distinct hierarchy of the decreasing patch sizes explained before. Hanover shows equally large volume

values in the centers like Hamburg (maximum around 100,000,000m³). Based on this information gained from the rank-size distributions Hamburg has the lowest degree of polycentricity and Nuremberg the highest degree of polycentricity among the four cities surveyed in Germany. Moreover, the count of the *area* ranks (Figure 25 bottom left) illustrates that (sub-)centers with lower area values (= higher rank-size) occur more often than those with higher area values (= lower rank-size).

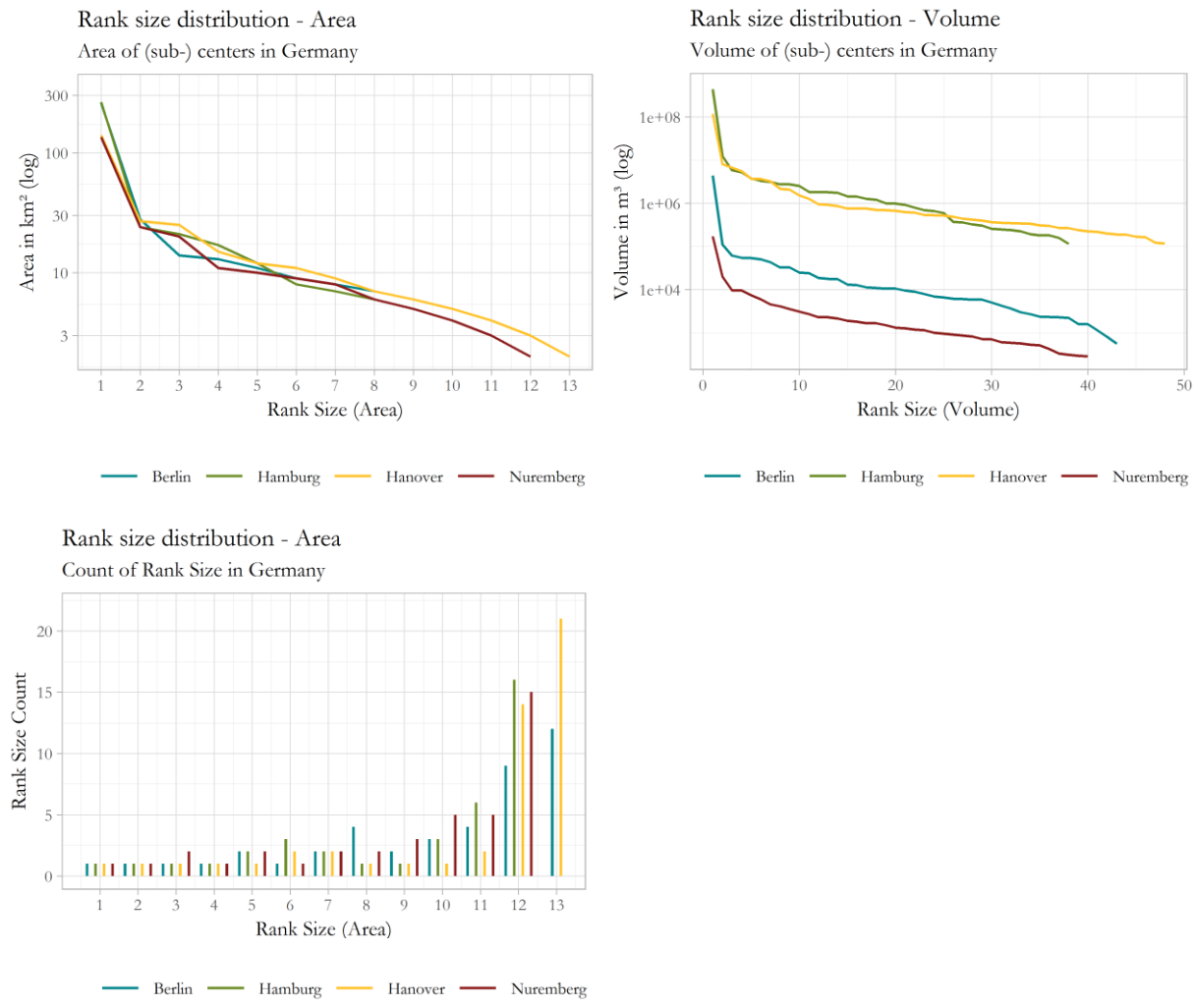

Figure 25: Results of the rank-size distribution for the parameters *area* (top left) and *volume* (top right) in Germany. Rank-size one represents the largest area/volume value in each case and rank-size *n* the smallest area/volume value. In addition, the frequency of the occurring area ranks is shown (bottom left; own Figure).

Largest patch index & non-site specific measures

Table 7 summarizes the results of the non-site specific measures and the LPI for each of the parameters *area* and *volume* in Germany. The LPI values are printed bold because they have a higher weighting compared to the non-site specific measures, as already described in the method (see chapter 2.3.5).

The LPI outcomes confirm the assignment of Hamburg to a low degree of polycentricity. The city has the highest LPI_{Area} (= 57.36%) among the German cities. This means that over 50% of the area of all detected center structures is concentrated in the traditional center. Moreover, 87% of the total volume categorized as hUMC belongs to this center (= LPI_{volume} of 87.43%). Therefore, its dominance is very pronounced. In comparison to the other German cities the measures mean size of (sub-)centers, mean volume of (sub-)centers and total volume of all detected (sub-)centers also confirm the allocation of Hamburg to a lower degree of polycentricity among the investigated German urban regions.

Berlin shows similar LPI values as Hamburg with a LPI_{Area} of 53.62% and a LPI_{volume} of 86.15%. Like Hamburg, Berlin concentrates over 50% of the total hUMC-area and over 80% of the total hUMC-volume in one center. Similarity between these two cities also appears through the mean size value for the centers, which is with 11.23km² just slightly below Hamburg (=12.16km²). However, the volume values (expressed by mean volume and total volume) are much lower. Based on these statements, Berlin is therefore also considered as a city with a rather low degree of polycentricity. Tendencies towards polycentricity, however, are already more present in Berlin compared to Hamburg because the LPI values as well as the mean size of the center structures are lower than the ones of Hamburg. Through the rank-size distribution Nuremberg has already been classified as a city with a higher degree of polycentricity among the four German investigated cities. The LPI results confirm this statement. In comparison to Berlin and Hamburg, only 39% of the total area characterized as hUMC and 63% of the total volume characterized as hUMC belong to the largest, traditional center. These values are still relatively high, especially the one of the LPI_{volume}. Nevertheless, Nuremberg tends to exhibit a more polycntric development compared to Hamburg and Berlin. The city shows, in addition, the lowest mean volume (= 6,804m³) and total volume (=272,167m³) values among the four German cities. Together with the, in comparison to Hamburg and Berlin, lower mean size value of 8,63km², Nuremberg clearly shows a higher degree of polycentricity.

Hanover could also be classified as more polycentric compared to Berlin and Hamburg due to the rank-size distribution. The value of the LPI_{Area} and the mean size, however, indicate an even higher degree of polycentricity than Nuremberg. The LPI_{Area} has a value of 37.94% and the mean size of (sub-)centers counts 7.53km². But the difference of these values compared to Nuremberg is quite small. The LPI_{Area} value shows only a one percent difference and the mean size less than one km² difference. The LPI_{Volume} is with 68.07% even higher than the one of Nuremberg. Based on these findings, Hanover gets categorized as the city with the second highest degree of polycentricity after Nuremberg (in relation to the four German cities under investigation). The

values of the mean volume and the total volume also justify this classification approach. The values are considerably higher compared to Nuremberg's volume values.

Table 7: Representation of the non-site specific dimensions and the LPI (largest patch index) for Germany; each for the parameter *area* and the parameter *volume* (own Table).

	LPI_{AREA} [%]	LPI_{VOLUME} [%]	MEAN SIZE [KM²]	TOTAL AREA [KM²]	MEAN VOLUME [M³]	TOTAL VOLUME [M³]
HAMBURG	**57.36**	**87.43**	12.16	462	13,126,684	498,814,000
HANOVER	**37.94**	**68.17**	7.53	369	3,507,094	171,847,600
BERLIN	**53.62**	**86.15**	11.23	483	118,224	5,083,651
NUREMBERG	**38.9**	**63.03**	8.68	347	6,804	272,167

In conclusion it can be stated, based on the approach used in this thesis, that Hamburg has the lowest degree of polycentricity among the four German cities under investigation. The city seems to be rather monocentric with a clear dominance of the traditional city center. This is followed by Berlin. The city also features a monocentric structure, although less pronounced than in Hamburg. Both Nuremberg and Hanover can be classified as cities with a higher degree of polycentricity compared to Hamburg and Berlin. Moreover, Nuremberg can be classified as even more polycentric than Hanover in regard to the rank-size distribution. In general, however, it is difficult to establish a ranking order for these two cities.

3.3.3 Polycentricity in the USA

In this chapter the results of the rank-size distribution, the LPI and the non-site specific measures for the USA are introduced and allow analysing polycentricity in US cities.

Rank-size distribution

The arrangement and the scaling of the diagrams in Figure 26 corresponds to that described in the previous chapter (3.2.2). Moreover, Philadelphia is included in the representation of results of the rank-size distribution within the USA despite the lack of data. However, the results must be related to the missing data, as especially the central city area is not correctly displayed. The surrounding areas of the study region, nevertheless, may still provide relevant information regarding the polycentric structure in Philadelphia.

The rank-sizes for the parameter *area* (top left) show a maximum of 25 (Atlanta) and a minimum of 17 (Austin). This means, a heterogeneity of 25 different sized area values could be detected in the USA. Furthermore, similar to Germany, the *area* rank-size distribution provides additional information about the actual 2D-size of the identified (sub-)centers. The center structure with the highest area value corresponding to the traditional center (= rank one) is larger than 300km² in

Atlanta and Austin. In Portland it is larger than 100km² and in Philadelphia the size is slightly below 100km². In Philadelphia, however, the largest detected center does not correspond to the traditional center. Due to the missing data, the traditional center is smaller and located at rank two. In the processed data in the scope of this thesis only a small part of this center structure is represented and not even the city center is contained (see Appendix III 2). Therefore, it must be assumed that the actual size of the traditional center exceeds the size of the highest area value detected in this thesis.

The *area* rank-size distribution between rank two and four shows (sub-)center sizes between 30km² and 100km² for Atlanta, Austin and Philadelphia. Especially in Austin and Atlanta the hierarchy between rank one and two is therefore very distinct. But from rank two onwards Atlanta shows a less distinct hierarchy. The slope is less pronounced in Philaldelphia because the largest detected center is already smaller than 100km². But is must be assumed that the actual hierarchy between rank one and two is more distinct due to the described characteristics. The distribution for Portland indicates the least pronounced hierarchy (in comparison to Austin and Atlanta). Rank two is located above 100km² and rank three just slightly below 100km².

A (sub-)center size of less than 10km² is only reached at rank ten in Austin, rank 13 in Portland, rank 15 in Philadelphia and rank 17 in Atlanta.

To conclude, the most distinct hierarchy by decreasing patch sizes between the largest, traditional center and the next smaller center can be observed in Austin and Atlanta. This indicates a dominance of the traditional center and a rather lower degree of polycentricity. In Atlanta, from rank two, however, a decreasing hierarchy can be determined. In comparison to the other US cities, Atlanta even shows the lowest hierarchy starting from rank five. Portland, having the least pronounced slope in the higher ranks, can be assigned to a higher degree of polycentricity with a less dominant traditional center compared to Austin and Atlanta. The degree of polycentricity in Philadelphia cannot be detected by using the information given by the highest rank. But the course of the distribution for the lower ranks indicates at least a higher degree of polycentricity as detected for Austin. The area values of rank one strengthen these assumptions. They are higher in Austin and Atlanta compared to Portland (Philadelphia's highest area value cannot be interpreted due to described reasons).

The *volume* rank-size distribution provides additional information. The volume values of Atlanta correspond with the observations seen in the distribution of the *area* rank-sizes. A distinct hierarchy by decreasing volume values can be identified, especially in the higher ranks. But it is striking that the volume values of Atlanta are below the ones of the other US cities, even the highest volume with about 10,000,000m³. The largest center volume of Portland, in contrast, is higher with about 100,000,000m³. Austin and Philadelphia also show a maximum volume value at

around 100,000,000m³. Regarding the hierarchy of decreasing (sub-)center volumes, the least distinct one can be assigned to Philadelphia, followed by Portland and Austin. For the two latter, this corresponds with the *area* ranking of the distinct hierarchy of the decreasing patch sizes explained before.

Based on the findings from the rank-size distributions for the parameters *area* and *volume*, Austin has the lowest degree of polycentricity and Portland the highest degree of polycentricity among the four examined US cities.

The count of the rank-sizes for the parameter *area* (Figure 26 bottom left) additionally reveals, that smaller center structures (= higher rank-size) occur more often than larger center structures (= lower rank-sizes).

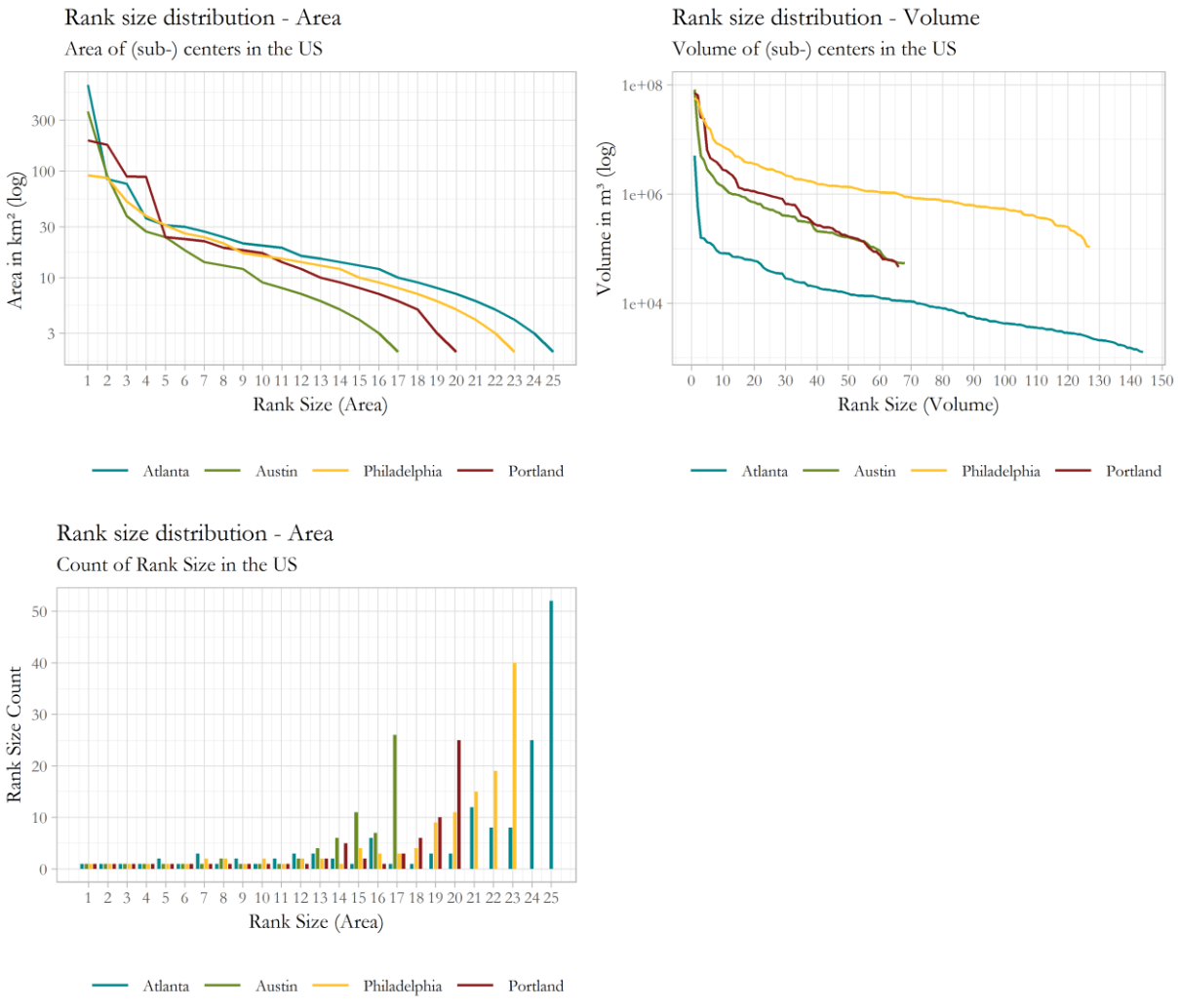

Figure 26: Results of the rank-size distribution for the parameters *area* (top left) and *volume* (top right) in the USA. Rank-size one represents the largest area/volume value in each case and rank-size *n* the smallest area/volume value. In addition, the frequency of the occurring area ranks is shown (bottom left; own Figure).

Largest patch index & non-site specific measures

Table 8 lists the results of the non-site specific measures and the LPI for each of the parameters *area* and *volume* in the USA. As in the corresponding table for Germany, the LPI values are printed bold due to their higher weighting compared to the non-site specific measures. Furthermore, the results for Philadelphia are shown in a different colour because they cannot be put into context with the other three US cities. The size of the traditional center and its volume are missing in the calculations for this city due to the lack of data. Since the dominance of this center is expressed by the LPI values, they are not correct for Philadelphia. But volume and size tendencies of the whole investigation area can be deduced based on the generated non-site specific measures of Philadelphia.

The highest LPI_{Area} value belongs to Austin with 44.66%. This means, about 45% of the total hUMC area is concentrated in the traditional center. In addition, about 60% of the total detected volume categorized as hUMC belongs to this center (LPI_{Volume} = 59.12%). These numbers confirm the assignment of Austin to a low degree of polycentricity conducted based on the rank-size distributions. The non-site specific measures calculated for Austin, in contrast, are not the highest compared to Portland and Atlanta. With 11.98 km² as the mean center size and a total (sub-)center area of 815km², Austin shows the lowest values. The values for mean volume and total volume are located in the middle between the ones of Portland and Atlanta.

Atlanta has a LPI_{Area} value of 37.22% and a LPI_{Volume} value of 58.32%. Therefore, they are below the LPI values of Austin. This corresponds with the hypothesis, that Atlanta has a higher degree of polycentricity than Austin, which was established through the rank-size distribution. Similar to Austin, it is difficult to associate the non-site specific measures with the degree of polycentricity. The mean size of the detected (sub-)centers is with 12.01 km² nearly similar to the one of Austin, whereas the volume values are significantly lower. This in turn, indeed, indicates a rather higher degree of polycentricity as well.

The highest degree of polycentricity was assigned to Portland by the rank-size distribution results. The LPI values also confirm this finding. With only 21% of the total hUMC area (LPI_{Area} = 21.27%) concentrated in the largest center, which holds only 29% of the total hUMC volume (LPI_{Volume} = 29.08%), the city shows a comparatively low dominance of the traditional center and therefore a lower degree of polycentricity. The non-site specific measures, again, do not correspond with this assumption. Portland has the highest mean size value with 13.82km², even though the difference is not very distinct compared to Austin and Atlanta. Moreover, the mean volume and total volume values are also the highest among these three US cities.

In the case of Philadelphia, the non-site specific measures as well as the LPI values cannot be interpreted in relation to the degree of polycentricity, but the total area value as well as the total

volume value provide additional information on the count and extent of (sub-)centers in this city. Only half of the investigation area could be processed in the context of this thesis (see Appendix III 2) and yet Philadelphia's identified (sub-)centers have the highest total volume and second highest total area value among the four US cities. This proofs, that this city holds the highest volume in regards to hUMCs. Moreover, it can be suspected that hUMCs in Philadelphia actually may cover an area larger than or nearly as high as detected for Atlanta, the city with the highest total area value.

Table 8: Representation of the non-site specific dimensions and the LPI (largest patch index) for the USA; each for the parameter *area* and the parameter *volume*. Philadelphia's values are presented in the colour grey because the values are not valid for the whole city due to errors in the underlying TanDEM-X data (own Table).

	LPI_{AREA} [%]	LPI_{VOLUME} [%]	MEAN SIZE [KM²]	TOTAL AREA [KM²]	MEAN VOLUME [M³]	TOTAL VOLUME [M³]
PORTLAND	**21.27**	**29.08**	13.82	912	3,699,271	244,151,900
AUSTIN	**44.66**	**59.12**	11.98	815	2,047,360	139,220,454
ATLANTA	**37.22**	**58.32**	12.01	1730	59,952	8,633,134
PHILADELPHIA	**9.39**	**29.08**	7.63	969	3,072,693	390,231,964

Regarding the sequence of degree of polycentricity, the rank-size distributions, the LPI values and the non-site specific measures for the USA allow to draw the following conclusions. Among the four investigated US cities Austin has the lowest degree of polyentricity. The city seems to be rather monocentric including a dominance of the traditional center. Atlanta as well shows a clear dominance of the traditional center. The surroundings, however, lean towards polycentric characteristics. Therefore, the city has a higher degree of polycentricity compared to Austin. Portland has the highest degree of polycentricity and the traditional center does not seem to be very dominant. Therefore, the city can be described as a city with a rather polycentric urban structure. The categorization of Philadelphia can only be done based on the rank-size distribution and without considering the degree of dominance of the traditional center. But the course of the area rank-size distribution suggests polycentric characteristics. Hence, the city gets ranked somewhere between Austin and Portland in regard to polycentricity.

3.3.4 Transcontinental comparison of polycentricity

As described in the method, polycentricity between Germany and the USA is compared within a radius of 40km around the city center based on the rank-size distribution for the parameters *area* and *volume* as well as on the LPI and the non-site specific measures. The rank-size distributions, shown in Figure 27 at the top and at the bottom, are displayed with a logarithmic scaling, similar

to the analysis within the countries, for a better representation of the differences between the cities under investigation. The LPI values and the non-site specific measures are listed in Table 9. Moreover, since the assessment of polycentricity for Philadelphia has only been possible to some extent within the USA, the city is excluded from the transcontinental comparison. Thus, the analysis of polycentricity between countries is based only on complete data.

The comparison of the *area* rank-size distribution between Germany (top left) and the USA (top right) provides first indications. Based on the slope of the distributions the German cities seem to have a higher distinct hierarchy by decreasing patch sizes than the US cities Atlanta and Portland. Austin, in contrast, indicates the most pronounced hierarchy among all German and US cities. Furthermore, except for Austin, the US cities show a slightly higher heterogeneity (13 & 15 rank sizes vs. 12 & 13 rank-sizes) in regard to different (sub-)center sizes, even though only 40km around the city center are included. Concerning the area value for rank one (= largest/traditional center), Atlanta and Austin have larger traditional centers (> 300km²) than Portland and the German cities (between 100km² and 300km²). In general, the actual 2D-sizes of the different ranks show that the German (sub-)centers are smaller than those in the USA, again except for Austin. Already from rank two the German (sub-)centers are smaller than 30km² and from rank six three out of the four German cities are smaller than 10km². Atlanta and Portland reach these area sizes only at higher ranks (< = 30km² at rank three and four, < = 10km² at rank ten and eight). Figure 28 (left side) shows these relations in an interrelated diagram, which displays the *area* rank-size distribution in a direct comparison between the USA and Germany. The representation in one diagram gives a clearer description of the indicators. Moreover, the count of the rank-sizes (Figure 27 middle) and the *volume* rank-size distribution (Figure 27 bottom) show that the German cities, in a radius of 40km around the city center, have more (sub-)centers than the US cities. Only Atlanta has a similar number with about 50 (sub-)centers. It is striking that Portland has less and Atlanta roughly the same amount of center structures, but still the hierarchy by decreasing patch sizes is less pronounced than in Germany. This can also be identified in the *volume* rank-size distribution for Atlanta and Portland, even though the less distinct hierarchy by decreasing volume values is only slightly recognizable. For the *volume* rank-size distribution Figure 28 (right side) also clarifies the relationships described in a direct comparison between the USA and Germany, without subdivision into the individual cities.

Figure 27: Results of the rank-size distribution for the parameters *area* (top) and *volume* (bottom). Rank-size one represents the largest area/volume value in each case and rank-size *n* the smallest area/volume value. In addition, the frequency of the occurring area ranks is shown in the middle. The outcome of the German cities is given on the left side and of the US cities on the right side of the Figure (own Figure).

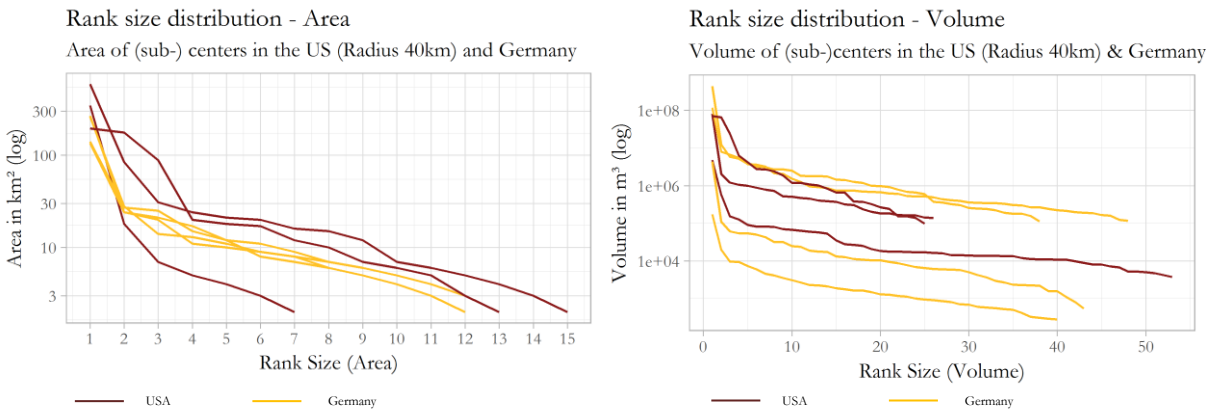

Figure 28: Results of the rank-size distribution for the parameters *area* (left) and *volume* (right) in a direct comparison between the USA and Germany. Rank-size one represents the largest area/volume value in each case and rank-size *n* the smallest area/volume value (own Figure).

The LPI values (Table 9) partly confirm these findings. Within a 40km radius around the city center Austin has a LPI_{Area} value of 77.03% and a LPI_{Volume} value of 86.04%. This indicates a very pronounced dominance of the traditional center in Austin. More than 75% of the total hUMC area and more than 85% of the total hUMC volume is concentrated in this center structure. Therefore, Austin shows the lowest degree of polycentricity among all German and US cities under investigation. Portland, in contrast, shows the highest degree of polycentricity among these cities. Only 32% of the total hUMC area (LPI_{Area} = 31.54%) and 37% of the total hUMC volume (LPI_{Volume} = 36.90%) is assigned to the traditional center. The classification of the remaining cities is more difficult. Atlanta has the second highest LPI_{Area} value (= 57.70%) after Austin. This finding is similar to the LPI_{Area} values shown by Hamburg and Berlin, cities that can be assigned to a lower degree of polycentricity in combination with their LPI_{Volume} values. But the LPI_{Volume} value (= 69.42%) of Atlanta resembles rather the LPI_{Volume} values of Hanover and Nuremberg, cities that can be assigned to a higher degree of polycentricity in combination with their LPI_{Area} values. Therefore, Atlanta takes a middle position between Hamburg and Berlin on one side and Nuremberg and Hanover on the other side in regard to the degree of polycentricity based on the LPI values. But it must be taken into account that not even the complete UA of Atlanta is included in the radius of 40km around the city center. Should the LPI values be overestimated, what may be suspected, Atlanta would have a higher degree of polycentricity than the German cities. This in turn would correspond to the results of the *area* ranks-size distribution. This characteristic of the data suspects that Atlanta, just like Portland, has a higher degree of polycentricity than the German cities, especially if the rank-size distribution is considered as well. Overall, it is difficult to pronounce a certain tendency of polycentricity between the USA and Germany based on the data within a 40km radius around the city center. This is further

complicated by the fact that the city with the lowest degree of polycentricity is located in the USA (Austin), as it is the city with the highest degree of polycentricity (Portland). Concerning the non-site specific measures (Table 9), the mean size of the (sub-)centers shows, like already identified through the rank-size distribution, that the center structures in Germany are smaller than in the USA. Moreover, a tendency can be established based on the total area and volume values. A larger 2D-area seems to be covered by hUMC within a 40km radius around the city center in the USA and these hUMC areas seem to hold a higher amount of 3D-urban masses. An exception is Hamburg, showing the highest total volume value of all cities under investigation.

Table 9: Representation of the none-site specific dimensions and the LPI (largest patch index) in Germany and the USA within a radius of 40km around the city center; each for the parameter *area* and the parameter *volume* (own Table).

	LPI_{AREA} [%]	LPI_{VOLUME} [%]	MEAN SIZE [KM²]	TOTAL AREA [KM²]	MEAN VOLUME [M³]	TOTAL VOLUME [M³]
PORTLAND	**31.54**	**36.90**	21.96	615	6,871,442	192,400,401
AUSTIN	**77.30**	**86.04**	17.11	445	3,593,951	93,442,749
ATLANTA	**57.70**	**69.42**	18.74	1012	127,965	6,910,116
HAMBURG	**57.36**	**87.43**	12.16	462	13,126,684	498,814,000
HANOVER	**37.94**	**68.17**	7.53	369	3,507,094	171,847,600
BERLIN	**53.62**	**86.15**	11.23	483	118,224	5,083,651
NUREMBERG	**38.9**	**63.03**	8.68	347	6,804	272,167

All in all, the transcontinental polycentricity comparison between Germany and the USA allows to draw the following conclusions. It is important to note that these are tendencies based on a comparison of seven cities and cannot be generalized. They apply to a radius of 40km around the city center of each urban region under investigation.

1) *More (sub-)centers in Germany than in the USA in terms of count*
2) *Smaller (sub-)centers in Germany than in the USA in terms of 2D-size*
3) *(Sub-)centers cover a larger area in the USA in terms of 2D-size*
4) *Slightly higher heterogeneity of (sub-)centers in the USA in terms of 2D-sizes*
5) *Slightly less distinct hierarchy be decreasing rank-sizes in the USA in terms of 2D- and 3D-sizes*

4 Discussion

In a first step this thesis applies an approach developed by Geiß et al. (2015c, 2017) for the first time in US cities to generate nDSMs and subsequently UMCs based on remotely sensed data. UMCs in Germany are calculated using the same procedure, but the method has already been validated by Geiß et al. (2015c, 2017) in this country. Secondly, UMCs in the USA are validated with LoD1 building footprint data. In a third and last step, a polycentricity analysis based on the generated UMCs is carried out between the cities within Germany and the USA and finally a transcontinental comparison is deployed between the two countries. Extraordinary about this comparison is the data basis: the UMCs are calculated with the same method - in Germany and in the USA. Until now there have always been solely transcontinental polycentricity analyses based on different data bases (see e.g. Krehl 2018). However, the generation of the UMCs, the validation of the UMCs in the USA and the subsequent polycentricity analysis revealed various characteristics that need to be discussed.

4.1 Urban mass concentration generation and validation

The validation results of the generated UMCs in the USA show that the TanDEM-X volume values are generally smaller than the LoD1 volume values in all four US cities (see chapter 3.2). This means that the nDSM might display a general underestimation. During the classification in BE and OBJ, too many OBJ pixels have possibly not been recognized as object above ground and thus have been categorized as BE. In consequence, an overestimation takes place in the DTM interpolation since too much height information of objects above ground is included. If the overestimated DTM is subsequently subtracted from the TDX DSM to generate the nDSM, an underestimation occurs. The validation outcome thus shows that the *error of commission* (= false positives) is very pronounced in all four US cities under investigation. Geiß et al. (2015c) also discussed this problem in their work. But by applying the postclassification algorithm SOBV (selective object-based voting) the researchers were able to compensate this error in Germany (Geiß et al. 2015c, 4359f.). In the USA, however, even under application of the SOBV algorithm after the RPMF (region growing Progressive Morphological Filter; see step 2) in Figure 9), the *error of commission* remains very high, as the validation results show. However, there are further possibilities that could lead to an underestimation of the nDSM. One of them is the chosen interpolation method used in the scope of this thesis to generate the DTM, namely the IDW (*inverse distance weighting*). But it must be considered that other interpolation methods are also just as suitable. Geiß et al. (2015c) for example also proposed *Ordinary Kriging* as possibility to generate the DTM (Geiß et al. 2015c, 4357). It is conceivable, that overestimation of the DTM may be less

pronounced if another interpolation method is applied and thus the underestimation of the nDSM heights would also be lower. Besides the technique, the methodological setup of the applied interpolation scheme is another source of error. The use of the IDW also includes the manual setting of a weighting factor. In the scope of this thesis the commonly used value '2' has been applied (see chapter 2.3.3.1 *Step 4*). But other values are possible as well. With increasing height of the weighting factor sample points (here: known height values) at a greater distance from the target variable (here: unknown height information) are given less consideration (Hengl 2009, 13). Different weighting factors therefore lead to different interpolation results. Hence, it is possible that a different weighting factor could achieve a better outcome, which would ultimately lead to a lower underestimation in the nDSM.

In addition, the TanDEM-X raw data itself are a possible source of error. This has already been clearly demonstrated in the course of this thesis in the extreme case of Philadelphia (see chapter 3.2 & 3.3.1). But also, the TDX DSMs showing less obvious errors or no errors at all can have a different quality regarding their height accuracy. All tiles come with information about their status - Approved, Limited Approval and Not Approved - specified in the Meta data. The state 'Approved' is applied to TDX DSM tiles if nothing special can be noted. The state 'Limited Approval' if e.g. cloud effects are visible or a height error due to the case that more than half of the land area in the tile is covered by forests or snow. 'Not Approved' is given if e.g. land coverage is missing and the affected area is larger than 1,000km² (Wessel 2018, 45ff.). In the scope of this thesis only tiles having the status 'Approved' or 'Limited Approval' have been used. But as the extreme case of Philadelphia has already shown, errors are nevertheless contained. Therefore, it would be conceivable to further develop the algorithm by only using tiles that are approved. Possible arising gaps could be compensated by further satellite data (e.g. Carotsat-1). This could potentially lead to better nDSM results. With regard to that, the relation between the state of approval and final nDSM quality must be examined more closely first, since it is not known to what extent the quality of the TDX DSMs influences the final product.

Another step that has affected the quality of the nDSM, is the setting of the SE (structuring element). The adjustment of the d_{max} value, which is needed to calculate the SE, has been done by visual inspection of underlying optical satellite images. Every city under investigation is covered by several TDX DSM tiles and within the buffer zone (100km radius in the USA; 40km radius in Germany) each tile has been processed separately with an optimized SE. Therefore, several d_{max} values have been determined for each urban region in dependence of the number of existing tiles (see chapter 2.3.3.1 *Classical Morphological Filtering* & *Step 1*). An alternative approach would have been to use a single SE per urban region. The final nDSM would then have a more uniform appearance, since the use of several SEs means that the intersections between the tiles can partly

also be seen in the final nDSM. An example is given in Appendix IV 1, where a transition zone from one SE to another is exemplarily shown in the nDSM of Atlanta. The Figure reveals that the height distribution changes depending on the underlying SE. Simultaneously, with one SE per urban region the local structures would not be preserved, as it is the case with several SEs. Further research is needed to determine whether the choice of the SE influences the height of the nDSM with regards to over- and underestimation or if the choice influences the nDSM, but not so far as significant under-or overestimation occurs.

Another possible source leading to an underestimation emerges after the nDSM processing. It must be taken into consideration that the masking with the NDVI may exclude too much building information. As a consequence, the volume values per processing unit are underestimated. In this thesis Sentinel-2 images between October and March (time span with low vegetational activity in the Global North) have been used to calculate the NDVI and thus exclude pixels from the subsequent UMC generation having a value above 0.3. But the comparison with optical satellite images displayed that this masking process also led to the exclusion of urban structures that might be residential areas. To minimize this error the time range of applied Sentinel-2 images could be reduced to November until February. In this season of the year the presence of active vegetation is comparatively lower than in the months October and March (at least in the Global North) and thus less pixels would show a NDVI value above 0.3. This change in the method could lead to a compensation of the underestimation seen in comparison with the validation data.

Nevertheless, it is also important to note that not only the presence of active vegetation might lead to an exclusion of too much building information. Different roofing materials must be taken into account as well when searching for errors leading to an underestimation in regard to the NDVI. Copper roofs for example can show NDVI values corresponding to active vegetation when they are exposed to a certain irradiation and direction of reflection (freiland Umweltconsulting ZT-GmbH 2010, 15f.). Therefore, it must be considered that an underestimation in the UMCs can also be intensified by the different reflection ratios of varying roof surface materials, since buildings can be mistakenly treated as vegetation.

The points mentioned above are potential sources of error which may influence the quality of the UMCs. But it is also possible that none of these points affected the height of the UMCs drastically. The latter case is conceivable, when the validation data is examined more closely. In general, the validation data is assumed to be true and the quality of the UMC calculations is measured based on this data. Moreover, since the MBF (Microsoft Building Footprint) covers parts of metro regions all over the USA, the LoD1 Microsoft data is also available for Portland, Austin and Philadelphia (and not only for Atlanta, where the MBF has been used for the

validation; OpenStreetMap Wiki 2018). In these cities the PBF (Portland Building Footprint), the ABF (Austin Building Footprint) and the PHBF (Philadelphia Building Footprint) have been used to validate the generated UMCs (see chapter 2.2 *validation*). Based on the assumption that the validation data reflects reality, the MBF data of the respective cities should therefore also be consistent with the ABF, the PBF and the PHBF (= correlation coefficient of '1' or close to '1'). The performance of a simple linear regression, exemplarily implemented for Portland and Austin (results in Appendix IV 2), between the MBF and the PBF/ABF in the respective areas covered by both data sources reveals something different. With correlation coefficients of 0.5786 (Austin) and 0.1026 (Portland) the data is neither identical nor correlated. This shows that even the validation data used in the scope of this thesis may not reflect reality and the occurring underestimation in the generated UMCs is therefore difficult to evaluate. It is even possible that the UMCs reflect reality better than the validation data.

All these factors suggest that there is a need for further research in the calculation of the nDSM and the subsequent UMC generation based on moderate resolution radar data. It is important to find out why underestimation occurs in the USA. However, the validation also proofed that the general distribution of the volumes in the city in relation from high to low in distance from the city center has been reflected more or less correctly (see chapter 3.2 Figure 20 & Appendix II).

4.2 Polycentricity analysis

As described in chapter 2.3.5, the identification of sub-(centers) is not based on the total volumes per grid cells, but on relative values greater than 1.3 SD (standard deviations) from the mean of all calculated volumes. Therefore, it is not the total height of the volumes that is decisive for the identification of the (sub-)centers. It is more important that densified areas have been identified at the correct location. Therefore, it can be assumed that even if the UMCs have been underestimated, the (sub-)centers have been identified correctly within the framework of the described definition.

This leads to the next discussion target. The approach to analyse polycentricity has been taken over from Taubenböck et al. (2017a) and they already claimed at the end of their work that there is not one truth and the identification of the hUMCs strongly depends on the method and the thresholds selected (Taubenböck et al. 2017a, 49f.). This means, that there is always the possibility that a different SD would have accomplished other maybe better results. Moreover Taubenböck et al. (2017a) additionally tested further conditions beside different SDs. They also implemented two more conditions, with whom their results got better. Next to a SD of 1.3, only grids with a larger built-up volume than 1000m³ and only identified hUMCs having an area larger than 2km² could be finally identified as (sub-)center (Taubenböck et al. 2017a, 52). As these cut-

off values are absolute values adjusted to the calculated UMCs of the cities under investigation, they could not simply be adopted to the underestimated UMCs in the USA. Nevertheless, such conditions could also improve the (sub-)center identification that has been conducted in the scope of this thesis.

Even though the analysis of polycentricity based on the morphological parameter built-up volume generated with moderate resolution DSMs makes it possible to carry out international comparisons as this thesis has proven, a realistic and correct characterization of spatial urban structures remains challenging. The scientific community is still far from a universally accepted measurement method due to the conceptual and analytical fuzziness of polycentricity. But an approach, which provides the possibility of application regardless of the area contributes to the understanding of polycentricity by providing a comprehensive view on this fuzzy concept (Taubenböck et al. 2017a, 54).

Similar to the characteristic of different methods and/or thresholds producing different results in regard to the number of identified (sub-)centers (Taubenböck et al. 2017a, 49) the results can differ in regard to the chosen processing units. In the scope of this thesis a grid with a 1km x 1km size of the single grid units has been chosen. Although this is a comparable and consistent spatial reference, the results are not protected from the MAUP (modifiable areal unit problem), which has been described in detail by Openshaw (1984). Thus, the chosen extents of the analysis units have an effect on the results. Even though the definition of spatial reference units is necessary, the outcome can vary depending on the underlying spatial structure (Madelin et al. 2009, 645f.).

Furthermore, it must be considered that there will always be the obstacle that the evaluation of functional polycentricity is not possible without additional socioeconomic data (Schneider et al. 2015, 46). A holistic picture of polycentricity in a city can never be given by morphology alone. The integration of remote sensing data can, however, be a supplement to empirically collected information dealing with functional polycentricity (de Sherbinin et al., 2002, 18). The combination of the potential of both, remote sensing and social science, has the ability to bear the desired result – to bring clarity and deepen the understanding of the concept of polycentricity.

5 Conclusion and Outlook

Conclusively the research questions, presented in chapter 1.3, will be answered.

Do the UMCs derived from TanDEM-X data by using the approach developed by Geiß et al. (2015c, 2017) render the urban morphology of cities in the USA?

The processing results of the morphological characterization (see chapter 3.1) demonstrate that the algorithm applied to the TDX DSMs enables to extract the urban structures. But there is a high chance that underestimation in terms of volumes occur as the validation indicated (see chapter 3.2). Nevertheless, the validation showed at the same time, that the location of urban structures was extracted more or less correctly. The algorithm has detected higher or lower volumes in the right locations. Therefore, it can be summarized that the approach developed by Geiß et al. (2015c, 2017) is able to render the urban morphology in US cities, although adjustments will have to be made in the future with regard to the underestimation.

Which differences and similarities in urban center distributions based on UMCs can be found between US and German cities?

The polycentricity analysis (see chapter 3) revealed that within a radius of 40km around the city center Germany has more hUMC structures than the USA. But they are comparatively smaller in terms of covered area size. Therefore, although Germany shows more (sub-)centers, hUMCs in the USA cover a larger area. It could also be discovered that, within a radius of 40km around the city center, the USA tends to show a less distinct hierarchy between the traditional center and further (sub-)centers, except for Austin. Therefore, monocentrism might be more pronounced in Germany than in the USA (statement applies to the cities under investigation) and the traditional center seems to have a higher weighting. However, independent of the country, Germany or the USA, a dominant center structure was identified in all cities under investigation and it is always located around the city center (except for Philadelphia, where the calculations are incorrect).

Can the assumptions about similar development of urban structures in US and German cities (see chapter 1.2) be confirmed?

This thesis can confirm that (sub-)centers exist in Germany and the USA. The aspect of the different sizes of these center structures could also be discovered. Likewise, the transcontinental analysis showed that cities with both, a higher degree as well as a lower degree in polycentricity, exist in both countries. Therefore, this thesis can confirm, that the urban development in Germany and the USA is similar or at least not significantly different. But only eight (seven) cities were examined in terms of their degree of polycentricity. Consequently, the assumption that a

polycentric development exists in both countries cannot be clearly confirmed nor contradicted. To make a statement like that, more cities need to be analysed.

This thesis was a first attempt to compare polycentricity transcontinental using a consistent data basis retrieved from remote sensing means. Nevertheless, the outcome is determined by the applied method, the threshold set and the underlying examination unit. This thesis proofed, however, that a transcontinental comparison of morphologic polycentricity is possible. But the discussion (see chapter 4) demonstrated, that during the processing of the UMCs and the subsequent polycentricity analysis, many points appeared that need to be looked at more closely in future work. Especially with regards to the applied method it would be profitable to further differentiate the parameters of (sub-)center identification. Moreover, a comparison of more cities in addition to the ones investigated in the context of this thesis could show, if Austin, the city with the lowest degree of polycentricity, is just an exception or if more cities with the same characteristics exist in the USA. Future work also needs to concentrate on the influence of the examination unit (keyword MAUP). The spatial conditions of cities in Germany and the USA complicated the transcontinental comparison. Therefore, it would be worth it to find a way that does justice to the spatial extent of US cities and at the same time the spatial extent of German cities in order to depict (sub-)centers as realistically as possible.

To conclude, the method applied in this thesis to generate the UMCs and the method used to identify (sub-)centers produce reasonable results, which give a first impression about the polycentric development in terms of morphology in Germany and the USA. Based on these findings it is now necessary to further develop the applied approaches. The inclusion of further socioeconomic data could also be useful in order to improve the (sub-)center identification procedure.

References

Print

Agarwal A., Giuliano G., Redfearn C.L. (2012): Strangers in our midst: the usefulness of exploring polycentricity. In: The Annals of Regional Science 48(2), 433-450.

AIRBUS (2015): TerraSAR-X Image Product Guide. Basic and Enhanced Radar Satellite Imagery. In: Airbus Defence and Space Issue 2.1, 1-24.

Alatorre L.C. & Begueria S. (2010): Analysis of spatial and temporal evolution of the NDVI on vegetated and degraded areas in the central Spanish Pyrenees. In: Wagner W., Székely B. (eds.): ISPRS TC VII Symposium - 100 Years ISPRS, Vienna, Austria, July 5-7, 2010, ISPRS, XXXVIII (7A), 7-12.

Amalorpavam G., Harish Naik T., Jyoti K., Suresha M. (2013): Analysis of Digital Images using Morphological Operations. In: International Journal of Computer Science & Information Technology 5(1), 145-159.

Anas A., Arnott R., Small K.A. (1998): Urban spatial structure. In: Journal of Economic Literature 36, 1426-11464.

Anas A. & Kim I. (1996): General Equilibrium Models of Polycentric Urban Land Use with Endogenous Congestion and Job Agglomeration. In: Journal of Urban Economics 40(0031), 232-256.

Anderson N.B. & Bogart W.T. (2001): Identifying and Characterizing Employment Centers in Polycentric Metropolitan Areas. In: American Journal of Economics and Sociology 60(1), 147-169.

Anthony J. (2004): Do state growth management regulations reduce sprawl? In: Urban Affairs Review 39(3), 376-397.

Astinus A.D. (2016): Die neun größten Städte Europas: Was du über diese Metropolen schon immer wissen wolltest. Neobooks.

Baltsavias E.P. (2004): Object extraction and revision by image analysis using existing geodata and knowledge: current status and steps towards operational systems. In: ISPRS Journal of Photogrammetry and Remote Sensing 58(3-4), 129-151.

Bengston D.N. & Youn Y.-C. (2006): Urban Containment Policies and the Protection of Natural Areas: The Case of Seoul's Greenbelt. In: Ecology and Society 11(1), 3.

Blaschke T. (2010): Object based image analysis for remote sensing. In: ISPRS Journal of Photogrammetry and Remote Sensing 65, 2-16.

Bruegmann R. (2005): Sprawl: A Compact History. University of Chicago Press, Chicago.

Burger M. & Meijers E. (2011): Form Follows Function? Linking Morphological and Functional Polycentricity. In: Urban Studies 49, 1127-1149.

Burrough P.A., McDonnell R.A., Lloyd C.D. (2015): Principles of Geographical Information Systems. Oxford University Press, 3rd ed., Oxford and New York.

Chen Q., Gong P., Baldocchi D., Xie G. (2007): Filtering Airborne Laser Scanning Data with Morphological Methods. In: Photogrammetric Engineering & Remote Sensing 73(2), 175-185.

Craig S.G. & Ng P.T. (2001): Using Quantile Smoothing Splines to Identify Employment Subcenters in a Multicentric Urban Area. In: Journal of Urban Economics 49, 100-120.

De Paul O.V. (2007): Remote Sensing: New Applications for Urban Areas. In: Proceedings of the IEEE 95(12), 2267-2268.

De Sherbinin A., Balk D., Yager K., Jaiteh M., Pozzi F., Giri C., Wannebo A. (2002): A CIESIN Thematic Guide to Social Science Applications of Remote Sensing. Palisades, NY.

Deutsches Zentrum für Luft- und Raumfahrt e.V. (2009): TanDEM-X. Die Erde in drei Dimensionen. Köln.

Dieleman F.M., Dijst M.J., Spit T. (1999): Planning the compact city: The Randstad Holland experience. In: European Planning Studies 7(5), 605-621.

Duranton G. & Puga D. (2015): Urban land use. In: Duranton G., Henderson J.V. & Strange W.C. (eds.): Handbook of regional and urban economics 5, Amsterdam, 467-560.

Duranton G. & Puga D. (2014): The growth of cities. In: Philippe A. & Durlauf S.N. (eds.): Handbook of Economic Growth 2B, Amsterdam, 781-853.

Ehlers M. (2006): New Developments and Trends for Urban Remote Sensing. In: Weng Q. & Quattrochi D.A. (eds.): Urban Remote Sensing. CRC Press Taylor & Francis Group, Boca Raton, London, New York, 357-375.

Erhardt A. (2008): Einführung in die Digitale Bildverarbeitung. Grundlagen, Systeme und Anwendungen. Vieweg & Teubner, 1st ed., Wiesbaden.

Esch T., Marconcini M., Felbier A., Roth A., Heldens W., Huber M., Schwinger M., Taubenböck H., Müller A., Dech S. (2013): Urban Footprint Processor – Fully Automated Processing Chain Generating Settlement Masks from Global Data of the TanDEM-X Mission. In: IEEE Geoscience and Remote Sensing Letters 10(6), 1617-1621.

Fauvel M., Chanussot J., Benediktsson J.A., Sveinsson J.R. (2007): Spectral and Spatial Classification of Hyperspectral Data Using SVMs and Morphological Profiles. In: IEEE Transactions on Geoscience and Remote Sensing 46(11), 3804-3814.

freiland Umweltconsulting ZT-GmbH (2010): Grünraumanalyse Wien. Dachbegrünung. Wien.

Gamba P. & Houshmand B. (2000): Digital surface models and building extraction: A comparison of IFSAR and LIDAR data. In: IEEE Transactions on Geoscience and Remote Sensing 38(4), 1959-1968.

Garcia-López M.-Á. & Muñiz I. (2010): Employment Decentralisation: Polycentricity or Scatteration? The case of Barcelona. In: Urban Studies 47(14), 3035-3056.

Gaschet F. (2002): The new intra-urban dynamics: Suburbanisation and functional specialisation in French cities. In: Papers in Regional Science 81, 63-81.

Gascon F., Cadau E., Colin O., Hoersch B., Isola C., López Fernández B., Martimort P. (2014): Copernicus Sentinel.2 Mission: Products, Algorithms and Cal/Val. Conference Paper in Proceedings of SPIE – The International Society for Optical Engineering, 1-9.

Geiß C., Wurm M., Taubenböck H. (2017): Towards Large-Area Morphologic Characterization of Urban Environments Using the TanDEM-X Mission and Sentinel-2. In: 2017 Joint Urban Remote Sensing Event (JURSE), Dubai, United Arab Emirates, 1-4.

Geiß C., Jilge M., Lakes T., Taubenböck H. (2016): Estimation of Seismic Vulnerability Levels of Urban Structures with Multisensor Remote Sensing. In: IEEE JSTARS 9(5), 1913-1936.

Geiß C., Aravena Pelizari P., Marconicini M., Sengara W., Edwards M., Lakes T., Taubenböck H. (2015a): Estimation of seismic building structural types using multi-sensor remote sensing and machine learning techniques. In: ISPRS Journal of Photogrammetry and Remote Sensing 104, 175-188.

Geiß C., Aravena Pelizari P., Taubenböck H. (2015b): Stadt in Gefahr – Erdbeobachtung zur Abschätzung der Folgen von Naturgefahren. In: Taubenböck H., Wurm M., Esch T., Dech S. (Hrsg.): Globale Urbanisierung. Perspektive aus dem All, Springer Spektrum, Berlin, Heidelberg.

Geiß C., Wurm M., Breunig M., Felbier A., Taubenböck H. (2015c): Normalization of TanDEM-X DSM Data in Urban Environments with Morphological Filters. In: IEEE Transactions on Geoscience and Remote Sensing 53(8), 4348-4362.

Giuliano G., Redfearn C., Agarwal A., Li C., Zhuang D. (2007): Employment concentration in Los Angeles, 1980-2000. In: Environment and Planning A 39, 2935-2957.

Giuliano G. & Small K.A. (1991): Subcenters in the Los Angeles region. In: Regional Science and Urban Economics 21, 163-182.

Gordon P. & Cox W. (2012): Cities in Western Europe and the United States: do policy differences matter? In: The Annals of Regional Science 48, 565-594.

Gordon P., Richardson H.W., Wong H.L. (1986): The distribution of population and employment in a polycentric city: the case of Los Angeles. In: Environment and Planning A 18, 161-173.

Greene D.L. (1980): Urban Subcenters. Recent Trends in Urban Spatial Structure. In: Growth and Change 11(1), 29-40.

Guillain R. & Le Gallo J. (2010): Agglomeration and dispersion of economic activities in and around Paris: an exploratory spatial data analysis. In: Environment and Planning B: Planning and Design 37, 961-981.

Hall P. & Pain K. (2006): The Polycentric Metropolis. Learning from mega-city regions in Europe. Earthscan, London and Sterling, VA.

Harlick R.M., Sternberg S.R., Zhuang X. (1987): Image Analysis Using Mathematical Morphology. In: IEEE Transactions on Pattern Analysis and Machine Intelligence PAMI-9(4), 532-550.

Heiden U., Heldens W., Roessner S., Segl K., Esch T., Mueller A. (2012): Urban structure type characterization using hyperspectral remote sensing and height information. In: Landscape and Urban Planning 105(4), 361-375.

Heiden U., Segl K., Roessner S., Kaufmann H. (2007): Determination of robust spectral features for identification of urban surface materials in hyperspectral remote sensing data. In: Remote Sensing of Environment 111, 537-552.

Heldens W., Heiden U., Esch T., Stein E., Müller A. (2011): Can the Future EnMAP Mission Contribute to Urban Applications? A Literature Survey. In: Remote Sensing 3, 1817-1846.

Hengl T. (2009): A Practical Guide to Geostatistical Mapping. Office for Official Publications of the European Communities, 2nd ed., Luxembourg.

Ketting R.L. & Landgrebe A. (1976): Classification of Multispectral Image Data by Extraction and Classification of Homogeneous Objects. In: IEEE Transactions on Geoscience Electronics 14(1), 19-26.

Kim J.I., Yeo C.H., Kwon J. (2014): Spatial change in urban employment distribution in Seoul metropolitan city: Clustering, dispersion and general dispersion. In: International Journal of Urban Sciences 18, 355-372.

Kim S. (2007): Changes in the nature of urban spatial structure in the United States, 1890-2000. In: Journal of Regional Science 47(2), 273-287.

Kloosterman R.C. & Lambregts B. (2001): Clustering of Economic Activities in Polycentric urban Regions: The Case of the Randstad. In: Urban Studies 38(4), 717-732.

Klotz M., Kemper T., Geiß C., Esch T., Taubenböck H. (2016): How good is the map? A multi-scale cross-comparison framework for global settlement layers: Evidence from Central Europe. In: Remote Sensing of Environment 178, 191-212.

Klotz M., Wurm M., Taubenböck H. (2015): Der Werkzeugkasten der urbanen Fernerkundung – Daten und Produkte. In: Taubenböck H., Wurm M., Esch T., Dech S. (eds.): Globale Urbanisierung. Perspektive aus dem All, Springer Spektrum, Berlin, Heidelberg.

Knapp W. & Volgmann K. (2011): Neue ökonomische Kerne in nordrhein-westfälischen Stadtregionen: Postsuburbanisierung und Restrukturierung kernstädtischer Räume. In: Raumforschung und Raumordnung 69(5), 303-317.

Krehl A. (2018): Urban subcentres in German city regions: Identification, understanding, comparison. In: Papers in Regional Science 97, 79-105.

Krehl A., Siedentop S., Taubenböck H., Wurm M. (2016a): A Comprehensive View on Urban Spatial Structure: Urban Density Patterns of Germany City Regions. In: ISPRS International Journal of Geo-Information 5(76), 1-21.

Krehl A., Münter A., Siedentop S. (2016b): Polyzentralität – ein facettenreiches raumwissenschaftliches Konzept. In: ILS(Institut für Landes- und Stadtentwicklungsforschung) - Trends 2(2016), 1-8.

Krehl A. (2015a): Urban spatial structure: an interaction between employment and built-up volumes. In: Regional Studies, Regional Science 2(1), 290-308.

Krehl A. (2015b): Polyzentralität in deutschen Stadtregionen – eine integrierte Bestandsaufnahme. In: Taubenböck H., Wurm M., Esch T., Dech S. (Hrsg.): Globale Urbanisierung. Perspektive aus dem All. Springer-Verlag, Berlin, Heidelberg.

Krieger G., Fiedler H., Zink M., Hajnsek I., Younis M., Huber S., Bachmann M., Hueso Gonzales J., Werner M., Moreira A. (2007): TanDEM-X: A satellite formation for high-resolution SAR interferometry. In: IEEE Trans. Geosci. Remote Sens. 45(11), 3317-3341.

Landis J.D. (2006): Growth Management Revisited. In: Journal of the American Planning Association 72(4), 411-430.

Lee B. (2007): 'Edge' or 'Edgeless Cities'? Urban Spatial Structure in US Metropolitan Areas, 1980 to 2000. In. Journal of Regional Science 47(3), 479-515.

Lee J.-S. (1983): Digital Image Smoothing and the Sigma Filter. In: Computer Vision, Graphics and Image Processing 24, 255-269.

Louis J. (2017): Sentinel-2. S2 MPC. L2A Product Definition Document. S2-PDGS-MPC-L2A-PDD. Issue 4.6, 1-36.

Lv Y., Zheng X., Zhou L., Zhang L. (2017): Decentralization and Polycentricity: Spatial Changes of Employment in Beijing Metropolitan Area, China. In: Sustainability 9(1880), 1-17.

Madelin M., Grasland C., Mathian H., Sanders L., Vincent J.-M. (2009): Das "MAUP": Modifiable Areal Unit – Problem oder Fortschritt? In: Informtionen zur Raumentwicklung 10/11, 645-660.

Maguya A. S., Junttila V., Kauranne T. (2013): Adaptive algorithm for large scale DTM interpolation from LiDAR data for forestry applications in steep forested terrain. In: ISPRS Journal of Photogrammetry and Remote Sensing 85, 74-83.

Maktav D., Erbek F.S., Jürgens C. (2005): Remote sensing of urban areas. In: International Journal of Remote Sensing 26(4), 655-659.

Markusen A. (1999): Fuzzy Concepts, Scanty Evidence, Policiy Distance: The Case for Rigour and Policy Relevance in Critical Regional Studies. In: Regional Studies 33(9), 869-884.

McDonald J.F. & Prather P.J. (1994): Suburban Employment Centres: The Case of Chicago. In: Urban Studies 31(2), 201-218.

McDonald J.F. & McMillen D.P. (1990): Employment subcenters and land values in a polycentric urban area: The case of Chicago. In: Environment and Planning A 22, 1561-1574.

McDonald J.F. (1987): The Identification of Urban Employment Subcenters. In: Journal of Urban Economics 21, 242-258.

McKillup S. & Darby Dyar M. (2010): Geostatistics Explained. An Introductory Guide for Earth Scientists. Cambridge University Press, Cambridge, UK.

McMillen D.P. (2001): Nonparametric Employment Subcenter Identification. In: Journal of Urban Economics 50, 448-473.

Meera Ghandi G., Parthiban S., Thummalu N., Christy A. (2015): Ndvi: Vegetation change detection using remote sensing and gis – A case study of Vellore District. In: Procedia Computer Science 57, 1199-1210.

Meng X., Currit N., Zhao K. (2010): Ground filtering algorithms for airborne LiDAR data: A review of critical issues. In: Remote Sensing 2(3), 833-860.

Nivola P.S. (1999): Laws of the landscape: how policies shape cities in Europe and America. The Brookings Institution, Washington DC.

Nivola P.S: (1998): Fat City: Understanding American Urban Form from a Transatlantic Perspective. In: The Brookings Review 16(4), 17-19.

Openshaw S. (1984): The Modifiable Areal Unit Problem. In: Concepts and Techniques in Modern Geography No. 38. Geo Books. Norwick.

Pal N.R. & Pal S.K. (1993): A review of image segmentation techniques. In: Pattern Recognition 26(9), 1277-1294.

Pingel T.J., Clarke K.C., McBride W.A. (2013): An improved simple morphological filter for the terrain classification of airborne LIDAR data. In: ISPRS Journal of Photogrammetry and Remote Sensing 77, 21-30.

Portland State University, Northwest Economic Research Center & Potiowsky T. (2018): Portland MSA Economic & Population Outlook April 2018. Northwest Economic Research Center Publications and Reports 31.

Ravi S. & Khan A.M. (2013): Morphological Operations for Image Processing: Understanding and its Applications. In: NCVSComs-13 Conference Proceedings. National Conference on VLSI, Signal processing & Communications. Vignan's University, Department of ECE, 17-19.

Redfearn C.L. (2007): The topography of metropolitan employment: Identifying centers of employment in a polycentric urban area. In: Journal of urban Economics 61, 519-541.

Richardson H.W. & Bae C.-H. C. (2016): Urban Sprawl in Western Europe and the United States. Routledge, 2nd ed., London & New York.

Riguelle F., Thomas I. (†), Verhetsel A. (2007): Measuring urban polycentrism: a European case study and ist implications. In: Journal of Economic Geography 7, 193-215.

Roca Cladera J., Marmolejo Duarte C.R., Moix M. (2009): Urban Structure and Polycentrism: Towards a Redefinition of the Sub-centre Concept. In: Urban Studies 46(13), 2841-2868.

Rosentreter J., Hagensieker R., Okujeni A., Roscher R., Wagner P., Waske B. (2017): Subpixel Mapping of Urban Areas Using EnMAP Data and Multioutput Support Vector Regression. In: IEEE Journal of Selected Topics in Applied Earth Observations and Remote Sensing 10(5), 1938-1948.

Rouse J.W.; Haas R.H., Deering D.W., Schell J.A. (1973): Monitoring the Vernal Advancement and Retrogradation (Green Wave Effect) of Natural Vegetation. NASA/GSFC Type II Report for Period April 1973-September 1973, Greenbelt, Maryland.

Schneider A., Chang C., Paulsen K. (2015): The changing spatial form of cities in Western China. In: Landscape and Urban Planning 135, 40-61.

Shafri H.Z.M., Taherzadeh E., Mansor S., Ashurov R. (2012): Hyperspectral Remote Sensing of Urban Areas: An Overview of Techniques and Applications. In: Research Journal of Applied Sciences, Engineering and Technology 4(11), 1557-1565.

Shearmur R. & Coffey W.J. (2002): A tale of four cities: intrametropolitan employment distribution in Toronto, Montreal, Vancouver, and Ottawa –Hull, 1981-1996. In: Environment and Planning A 34, 575-598.

Siedentop S., Fina S., Krehl A. (2016): Greenbelts in Germany's regional plans – An effective growth management policy? In: Landscape and Urban Planning 145, 71- 82.

Sirmacek B., Taubenböck H., Reinartz P., Ehlers M. (2012): Performance Evaluation for 3-D City Model Generation of Six Different DSMs from Air- and Spaceborne Sensors. In: IEEE Journal of Selected Topics in Applied Earth Observations and Remote Sensing 5(1), 59-70.

Sithole G. (2001): Filtering of Laser Altimetry Data using a Slope Adaptive Filter. In: IAPRS International Archives of Photogrammetry and Remote Sensing XXXIV-3/W4, 203-210.

Soille P. (2004): Morphological Image Analysis. Springer-Verlag, 2nd ed., Berlin, Heidelberg, New York.

Taubenböck H., Standfuß I., Wurm M., Krehl A., Siedentop S. (2017a): Measuring morphological polycentricity – A comparative analysis of urban mass concentrations using remote sensing data. In: Computers, Environment and Urban Systems 64, 42-56.

Taubenböck H., Ferstl J., Dech S. (2017b): Regions Set in Stone – Delimiting and Categorizing Regions in Europe by Settlement Patterns Derived from EO-Data. In: ISPRS International Journal of Geo-Information 6(55), 1-27.

Taubenböck H., Klotz M., Wurm M., Schmieder J., Wagner B., Wosster M., Esch T. (2013): Central Business Districts: Delineation in mega city regions using remotely sensed data. In: Remote Sensing of Environment 136, 386-401.

Taubenböck H., Esch T., Felbier A., Roth A., Dech S. (2011): Pattern-Based Accuracy Assessment of an Urban Footprint Classification Using TerraSAR-X Data. In: IEEE Geoscience and Remote Sensing Letters 8(2), 278-282.

Vasanen A. (2012): Functional Polycentricity: Examining Metropolitan Spatial Structure through the Connectivity of Urban Sub-centres. In: Urban Studies 49(16), 3627-3644.

Veneri P. & Burgalassi D. (2012): Questioning Polycentric Development and ist Effects. Issues of Definition and Measurement for the Italian NUTS-2 Regions. In: European Planning Studies 20(6), 1017-1037.

Vosselman G. (2000): Slope based Filtering of Laser Altimetry Data. In: IAPRS International Archives of Photogrammetry and Remote Sensing XXXIII, 958-964.

Webster R. & Oliver M.A. (2007): Geostatistics for Environmental Scientists. John Wiley & Sons Ltd., 2nd ed., West Sussex.

Weidner U. & Förstner W. (1995): Towards automatic building extraction from high resolution digital elevation models. In: ISPRS Journal of Photogrammetry and Remote Sensing 50(4), 38-49.

Wessel B. (2018): TanDEM-X Ground Segment – DEM Products Specification Document. EOC, DLR, Oberpfaffenhofen, Germany, Public Document TD-GS-PS-0021, Issue 3.2, 1-49.

Wollschläger D. (2017): Grundlagen der Datenanalyse mit R. Eine anwendungsorientierte Einführung. Springer Spektrum, 4th revised ed., Berlin.

Woo M. & Guldmann J.-M. (2014): Urban Containment Policies and Urban Growth. In: International Journal of Urban Sciences 18(3), 309-326.

Wurm M., Schmitt A., Taubenböck H. (2016): Building Types‘ Classification Using Shape-Based Features and Linear Discriminant Functions. In: IEEE JSTARS 9(5), 1901-1912.

Wurm M., d’Angelo P., Reinartz P., Taubenböck H. (2014): Investigating the Applicability of Cartosat-1 DEMs and Topographic Maps to Localize Large-Area Urban Mass Concentrations. In: IEEE Journal of Selected Topics in Applied Earth Observations and Remote Sensing 7(10), 4138-4152.

Wurm M., Taubenböck H., Schardt M., Esch T., Dech S. (2011): Objectbased image information fusion using multisensor Earth observation data over urban areas. In: International Journal of Image and Data Fusion 2(2), 121-147.

Yue W., Liu Y., Fan P. (2010): Polycentric urban development: the case of Huangzhou. In: Environment and Planning A 42, 563-577.

Zhang K., Chen S.-C., Whitman D., Shyu M.-L., Yan J., Zhang C. (2003): A Progressive Morphological Filter for Removing Nonground Measurements from Airborne LIDAR Data. In: IEEE Transactions on Geoscience and Remote Sensing 41(4), 872-882.

Zhong C., Schläpfer M., Müller Arisona S., Batty M. Ratti C., Schmitt C. (2015): Revealing Centrality in the Spatial Structure of Cities from Human Activity Patterns. In: Urban Studies 54(2), 437-455.

Zimmermann-Janschitz S. (2014): Statistik in der Geographie. Eine Exkursion durch die deskriptive Statistik. Springer-Verlag, Berlin, Heidelberg.

Zink M., Bachmann M., Bräutigam B., Fritz T., Hajnsek I., Krieger G., Moreira A., Wessel B. (2014): TanDEM-X: The New Global DEM Takes Shape. In: IEEE Geoscience and Remote Sensing Magazine, 8-23.

Online

Advameg, Inc. (2019a): Portland: Geography and Climate. URL: http://www.city-data.com/us-cities/The-West/Portland-Geography-and-Climate.html (23.02.2019).

Advameg, Inc. (2019b): Austin: Geography and Climate. URL: http://www.city-data.com/us-cities/The-South/Austin-Geography-and-Climate.html (02.03.2019).

Advameg, Inc. (2019c): Austin: Introduction. URL: http://www.city-data.com/us-cities/The-South/Austin-Introduction.html (02.03.2019).

Advameg, Inc. (2019d): Atlanta: Geography and Climate. URL: http://www.city-data.com/us-cities/The-South/Atlanta-Geography-and-Climate.html (02.03.2019).

Advameg, Inc. (2019e): Atlanta: Introduction. URL: http://www.city-data.com/us-cities/The-South/Atlanta-Introduction.html (02.03.2019).

Advameg, Inc. (2019f): Philadelphia: Geography and Climate. URL: http://www.city-data.com/us-cities/The-Northeast/Philadelphia-Geography-and-Climate.html (03.03.2019).

Advameg, Inc. (2019g): Philadelphia: Introduction. URL: http://www.city-data.com/us-cities/The-Northeast/Philadelphia-Introduction.html (03.03.2019).

Amt für Statistik Berlin-Brandenburg (2019a): Auf einen Blick. URL: https://www.statistik-berlin-brandenburg.de/ (14.03.2019).

Amt für Statistik Berlin-Brandenburg (2019b): Bevölkerungsstand. Zeitreihen. URL: https://www.statistik-berlin-brandenburg.de/BasisZeitreiheGrafik/Zeit-Bevoelkerungsstand.asp?Ptyp=400&Sageb=12015&creg=BBB&anzwer=6 (13.03.2019).

Bayerisches Landesamt für Umwelt (2011): Entwurf einer kulturlandschaftlichen Gliederung. Nr.21: Ballungsraum Nürnberg-Fürth-Erlangen. URL: https://www.lfu.bayern.de/natur/kulturlandschaft/entwurf_gliederung/index.htm (13.03.2019).

Berlinstadtservice (2019): Geographische Lage von Berlin. URL: https://www.berlinstadtservice.de/xinh/Berlin_Geographie.html (13.03.2019).

Catcomm Kommunikation (2018): Wirtschaftswachstum: Nürnberg im Aufwind. URL: http://www.zaronews.world/wirtschaft/wirtschaftswachstum-nuernberg-im-aufwind/ (11.03.2019).

City of Atlanta (2019): Hartsfield-Jackson Atlanta International Airport. URL: https://www.atl.com/ (22.03.2019).

City of Austin (2019): Building Footprints Year 2013. URL: https://data.austintexas.gov/Locations-and-Maps/Building-Footprints-Year-2013/7bns-7teg (18.02.2019).

Climate Data (2019): Climate Berlin-Germany. URL: https://www.climatedata.eu/climate.php?loc=gmxx0007&lang=en (13.03.2019).

Climate-Data.org (2019a): Klima Nürnberg. URL: https://de.climate-data.org/europa/deutschland/bayern/nuernberg-6203/ (11.03.2019).

Climate-Data.org (2019b): Klima Berlin. URL: https://de.climate-data.org/europa/deutschland/berlin/berlin-2138 (13.03.2019).

Climate-Data.org (2019c): Klima Hannover. URL: https://de.climate-data.org/europa/deutschland/niedersachsen/hannover-6333/ (14.03.2019).

Climate-Data.org (2019d): Klima Hamburg. URL: https://de.climate-data.org/europa/deutschland/hamburg/hamburg-69/ (15.03.2019).

Deutsche Forschungsgemeinschaft - DFG (2019): Where are the jobs? Stadtregionale Zentrenstrukturen im internationalen Vergleich. URL: http://gepris.dfg.de/gepris/projekt/398024191 (23.02.2019).

Deutsches Zentrum für Luft- und Raumfahrt e.V. (DLR) (2019): EnMAP – der deutsche Hyperspektralsatellit zur Erdbeobachtung. URL: https://www.dlr.de/dlr/desktopdefault.aspx/tabid-10379/567_read-421/#/gallery/2671 (15.03.2019).

Dumrath & Fassnacht KG GmbH & Co. (2019): Die wirtschaftliche Entwicklung Hamburgs. URL: https://www.hamburg-magazin.de/service/wirtschaft/artikel/detail/hamburg-wirtschaft-entwicklung.html (15.03.2019).

Encyclopaedia Britannica (2019): Hamburg. URL: https://www.britannica.com/place/Hamburg-Germany (17.03.2019).

European Space Agency (ESA; 2019a): Science Toolbox Exploitation Platform. URL: http://step.esa.int/main/ (29.01.2019).

European Space Agency (ESA; 2019b): Sen2Cor. URL: http://step.esa.int/main/third-party-plugins-2/sen2cor/ (29.01.2019).

European Space Agency (ESA; 2019c): Sentinel-2. URL: https://sentinel.esa.int/web/sentinel/missions/sentinel-2 (06.02.2019).

European Space Agency (ESA; 2019d): Introducing Sentinel-2. URL: https://www.esa.int/Our_Activities/Observing_the_Earth/Copernicus/Sentinel-2/Introducing_Sentinel-2 (06.02.2019).

European Space Agency (ESA; 2019e): Mission Objectives. URL: https://sentinel.esa.int/web/sentinel/missions/sentinel-2/mission-objectives (06.02.2019).

European Environment Agency (2018): Urban morphological zones 2006. URL: https://www.eea.europa.eu/data-and-maps/data/urban-morphological-zones-2006-1#tab-figures-produced (09.02.2019).

Hamburg.de GmbH & Co.KG (2019): Hamburg in Zahlen. URL: https://www.hamburg.de/info/3277402/hamburg-in-zahlen/ (17.03.2019).

Handelskammer Hamburg (2019): Bevölkerung. URL: https://www.hk24.de/produktmarken/beratung-service/konjunktur-statistik/hamburger-wirtschaft-zahlen/bevoelkerung/3676958 (15.03.2019).

Hannover.de (2019a): Der Standort Hannover: Daten & Fakten im Überblick. URL: https://www.hannover.de/Service/Presse-Medien/Presseservice-Marke%C2%ADting,-Tourismus,-Wirtschaft/Allgemeine-Tex%C2%ADte-Hannover-im-%C3%9Cberblick/Der-Standort-Hannover-Daten-Fakten-im-%C3%9Cberblick (14.03.2019).

Hannover.de (2019b): Hannover in Zahlen. Stadtgebiet. Die Stadtfläche der Landeshauptstadt Hannover in Zahlen (Stand. 1. Januar 2019). URL: https://www.hannover.de/Leben-in-der-Region-Hannover/Politik/Wahlen-Statistik/Statistikstellen-von-Stadt-und-Region/Statistikstelle-der-Landeshauptstadt-Hannover/Hannover-in-Zahlen/Stadtgebiet (14.03.2019).

Hannover.de (2019c): Hannover in Zahlen. Einwohner. Hannovers Bevölkerung in Zahlen. URL: https://www.hannover.de/Leben-in-der-Region-Hannover/Politik/Wahlen-Statistik/Statistikstellen-von-Stadt-und-Region/Statistikstelle-der-Landeshauptstadt-Hannover/Hannover-in-Zahlen/Einwohner (14.03.2019).

Hannover.de (2019d): Hannover in Zahlen. Wirtschaft. Hannovers Wirtschaft in Zahlen. URL: https://www.hannover.de/Leben-in-der-Region-Hannover/Politik/Wahlen-Statistik/Statistikstellen-von-Stadt-und-Region/Statistikstelle-der-Landeshauptstadt-Hannover/Hannover-in-Zahlen/Wirtschaft (14.03.2019).

Hannover.de (2016): Wirtschaftsreport 2016 für die Region Hannover. Wirtschaftliche Entwicklung 2005 bis 2015. URL: https://www.hannover.de/Wirtschaft-Wissenschaft/Wirtschaftsf%C3%B6rderung/Standort/Wirtschaftsstandort/Wirtschaftsreport (14.03.2019).

Klimatabelle.Info (2019): Klimatabelle Portland. URL: https://www.klimatabelle.info/nordamerika/usa/portland (21.03.2019).

Koordinates (2019): Portland, Oregon Building Footprints. URL: https://koordinates.com/layer/96789-portland-oregon-building-footprints/ (18.02.2019).

Landeshauptstadt Hannover (2018): Einwohnerstand der LH Hannover Ende 2017 und Einwohnerentwicklung im Jahr 2017. Baudezernat, Fachbereich Planen und Stadtentwicklung, Bereich Stadtentwicklung. URL: https://www.hannover.de/Leben-in-der-Region-Hannover/Verwaltungen-Kommunen/Die-Verwaltung-der-Landeshauptstadt-Hannover/Dezernate-und-Fachbereiche-der-LHH/Baudezernat/Fachbereich-Planen-und-Stadtentwicklung/Stadtentwicklung/Bev%C3%B6lkerungsentwicklung-und-demografischer-Wandel (14.03.2019).

Marketingverein der Europäischen Metropolregion Nürnberg e.V. (2019): Europäische Metropolregionen in Bayern (03/2018). URL: https://www.metropolregionnuernberg.de/downloads/publikationen/publikationen-und-praesentationen.html#c9648 (11.03.2019).

McCann A. (2018): Fastest-Growing Cities in America. URL: https://wallethub.com/edu/fastest-growing-cities/7010/#overall (02.03.2019).

Microsoft (2018): USBuildingFootprints. URL: https://github.com/Microsoft/USBuildingFootprints (17.02.2019).

Naturpark Barnim (2019): Landschaftsentstehung. URL: https://www.barnim-naturpark.de/naturpark/natur-landschaft/landschaftsentstehung/ (13.03.2019).

OpenDataPhilly (2019): Building Footprints. URL: https://www.opendataphilly.org/dataset/buildings (03.03.2019).

OpenStreetMap Wiki (2018): Bibliographic details for Microsoft Building Footprint Data. URL: https://wiki.openstreetmap.org/w/index.php?title=Microsoft_Building_Footprint_Data&oldid=1695026 (17.02.2019).

Patch Media (2019): Austin is America's Fastest-Growing City: Report. URL: https://patch.com/texas/downtownaustin/austin-americas-fastest-growing-city-report (02.03.2019).

Reinthaler W. (2019): Hamburg-Geographie. URL: https://www.bilderreisen.at/ham/hamburg-landeskunde-geografie.php (17.03.2019).

Salazar D. (2018): Austin adding jobs faster than any other big U.S. city, except Orlando. URL: https://www.bizjournals.com/austin/news/2018/11/20/austin-adding-jobs-faster-than-any-other-big-u-s.html (03.03.2019).

Senatsverwaltung für Wirtschaft, Energie und Betriebe (2019): Wirtschaftsleistung. Entwicklung des Bruttoinlandsprodukts (BIP) in Berlin. URL: https://www.berlin.de/sen/wirtschaft/wirtschaft/konjunktur-und-statistik/wirtschaftsdaten/wirtschaftsleistung/ (13.03.2019).

Socrata (2019a): Portland Geographic. URL: https://www.opendatanetwork.com/entity/1600000US4159000/Portland_OR/geographic.population.density?year=2017 (23.02.2019).

Sperling's Best Place (2019): Atlanta, Georgia. Economy in Atlanta, Georgia. URL: https://www.bestplaces.net/economy/city/georgia/atlanta (02.03.2019).

Stadt Nürnberg (2019a): Nürnberg in Zahlen: Daten und Fakten. URL: https://www.nuernberg.de/internet/stadtportal/daten_und_fakten.html (11.03.2019).

Stadt Nürnberg (2019b): Bevölkerungsstand. URL: https://online-service2.nuernberg.de/aswn/ASW.exe?aw=BBSE_J05 (11.03.2019).

Stadt Nürnberg (2019c): Arbeitslose. URL: https://online-service2.nuernberg.de/aswn/ASW.exe?aw=M_MN02 (13.03.2019).

Statista GmbH (2019a): Statistiken zu Hamburg. URL: https://de.statista.com/themen/1440/hamburg/ (15.03.2019).

Statista GmbH (2019b): Bruttoinlandsprodukt von Hamburg bis 2017. URL: https://de.statista.com/statistik/daten/studie/5014/umfrage/entwicklung-des-bruttoinlandsprodukts-von-hamburg-seit-1970/ (15.03.2019).

Statistisches Bundesamt (2019): Deutsche Wirtschaft ist im Jahr 2018 um 1,5% gewachsen. URL: https://www.destatis.de/DE/PresseService/Presse/Pressemitteilungen/2019/01/PD19_018_811.html (11.03.2019).

Texas Parks & Wildlife Foundation (2019): Texas Ecoregions. URL: https://tpwd.texas.gov/education/hunter-education/online-course/wildlife-conservation/texas-ecoregions (02.03.2019).

United States Census Bureau (2018): Urban Areas. URL: https://www.census.gov/cgi-bin/geo/shapefiles/index.php?year=2018&layergroup=Urban+Areas (09.02.2019).

U.S. Bureau of Labor Statistics (2019): Philadelphia Area Employment – November 2018. URL: https://www.bls.gov/regions/mid-atlantic/news-release/areaemployment_philadelphia.htm (03.03.2019).

US Climate Data (2019a): Climate Portland-Oregon. URL: https://www.usclimatedata.com/climate/portland/oregon/united-states/usor0275 (17.03.2019).

US Climate Data (2019b): Climate Austin-Texas. URL: https://www.usclimatedata.com/climate/austin/texas/united-states/ustx2742 (17.03.2019).

US Climate Data (2019c): Climate Atlanta-Georgia. URL: https://www.usclimatedata.com/climate/atlanta/georgia/united-states/usga1761 (17.03.2019).

US Climate Data (2019d): Climate Philadelphia-Pennsylvania. URL: https://www.usclimatedata.com/climate/philadelphia/pennsylvania/united-states/uspa1276 (17.03.2019).

Wetter.de (2019): Klima und Wetter in Nürnberg. URL: https://www.wetter.de/klima/europa/deutschland/nuernberg-s107630.html (11.03.2019).

World Population Review (2018a): US City Populations 2019. ULR: http://worldpopulationreview.com/us-cities/ (23.02.2019).

World Population Review (2018b): Population of Cities in Oregon (2019). URL: http://worldpopulationreview.com/states/oregon-population/cities/ (23.02.2019).

World Population Review (2018c): Population of Cities in Texas (2019). URL: http://worldpopulationreview.com/states/texas-population/cities/ (02.03.2019).

World Population Review (2018d): Population of Cities in Pennsylvania (2019). URL: http://worldpopulationreview.com/states/pennsylvania-population/cities/ (03.03.2019).

Appendix

Appendix I: Urban mass concentrations

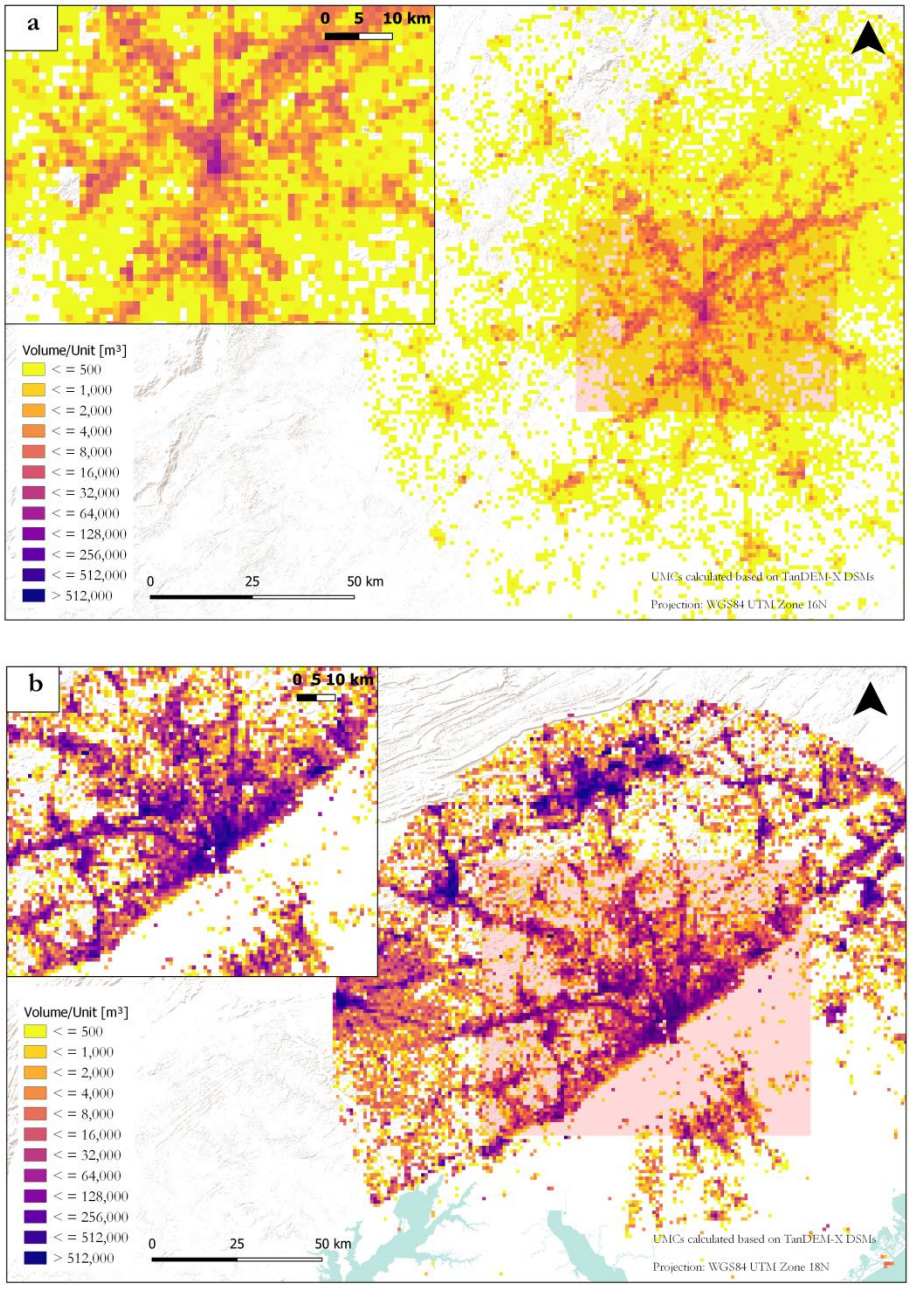

Appendix I 1: Generated UMC (urban mass concentration) in Atlanta (a) and Philadelphia (b). The UMC corresponds to the volume per unit having an area size of 1km x 1km. Due to errors in the raw data, only for about half of the investigation area the UMCs could be calculated in Philadelphia (own Figure).

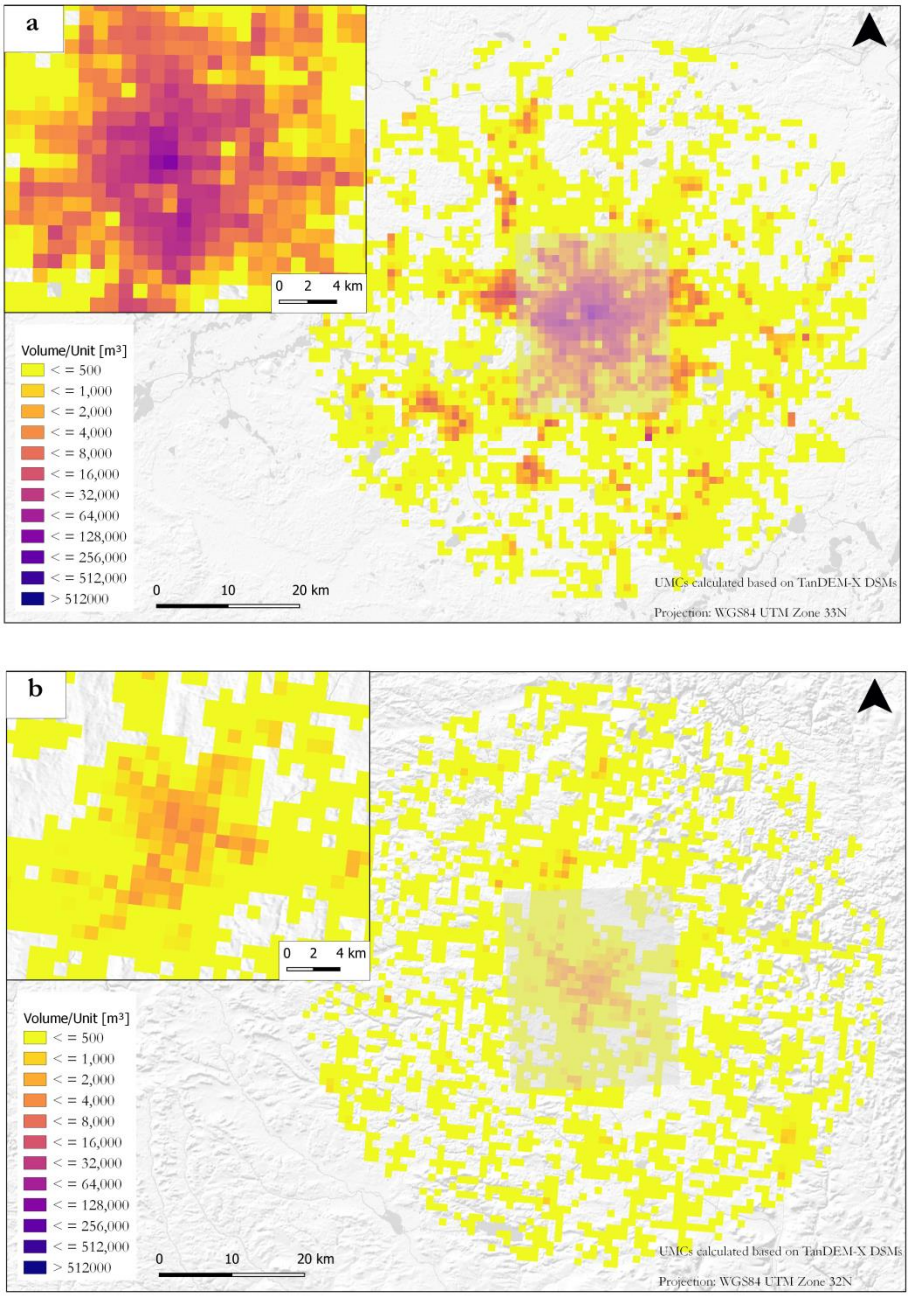

Appendix I 2: Generated UMC (urban mass concentration) in Berlin (a) and Nuremberg (b). The UMC corresponds to the volume per unit having an area size of 1km x 1km (own Figure).

Appendix II: Urban mass concentrations in distance to the city center

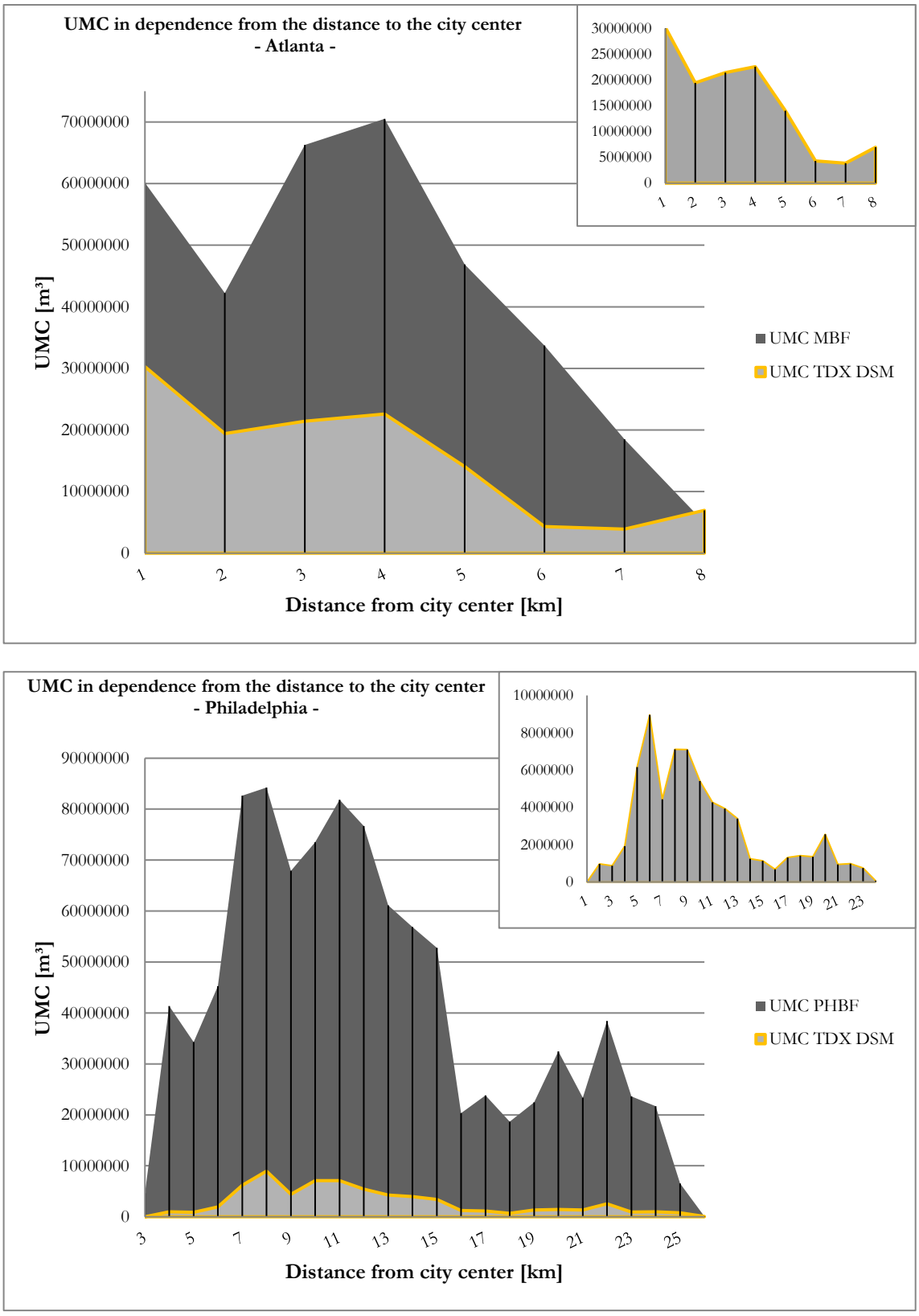

Appendix II: Representation of UMCs (urban mass concentrations) (x-axis) as a function of distance to the city center (y-axis) for Atlanta (a) and Philadelphia (b). In intervals of one kilometre the volumes per grid cells are summed up. The UMCs on the y-axis therefore show the total volume per kilometre (own Figure).

Appendix III: High urban mass concentrations

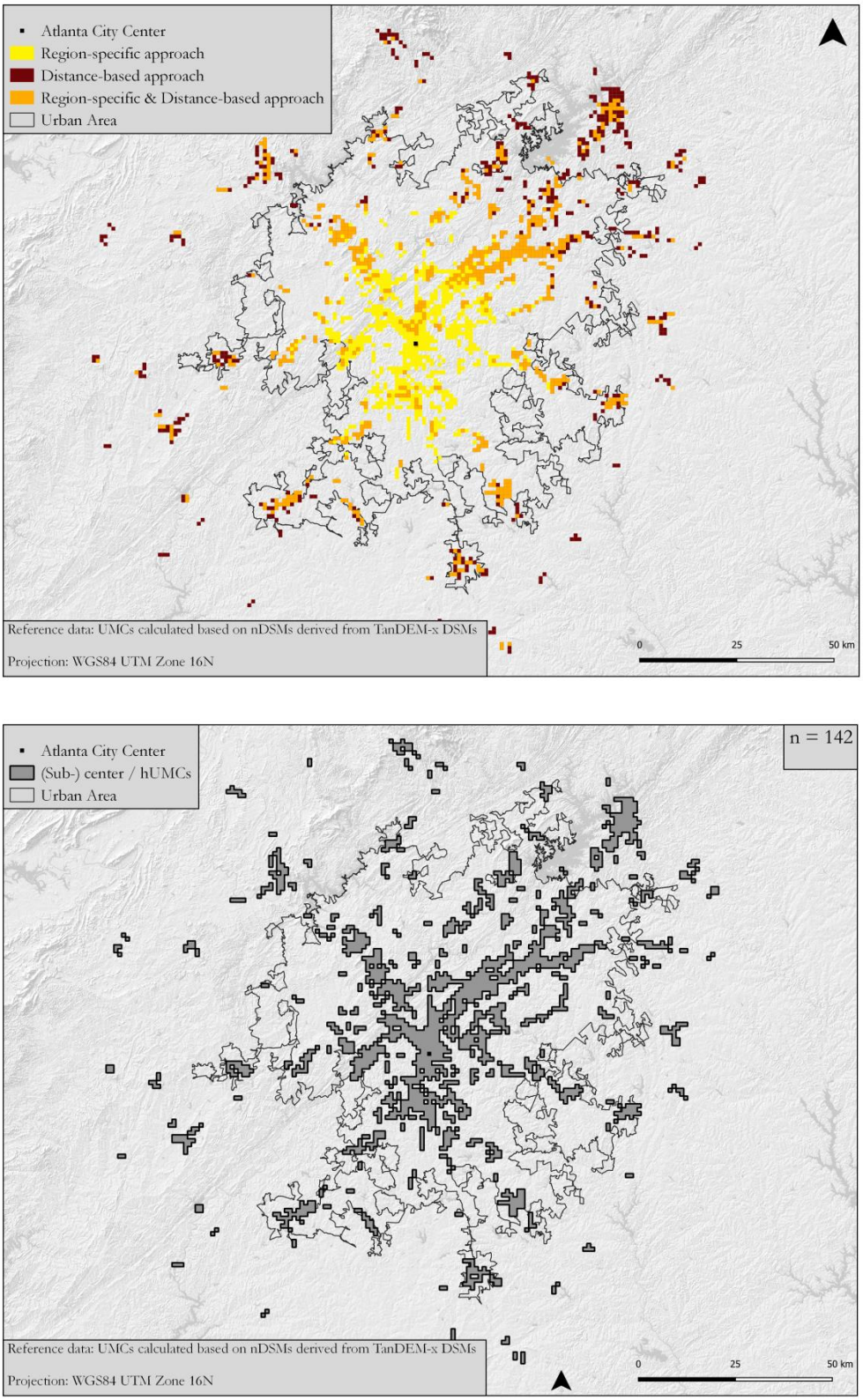

Appendix III 1: Detected (sub-)centers in Atlanta. Top: Representation of the hUMCs (high urban mass concentrations) assigned to the classes region-specific (yellow), distance-based (red) and region-specific & distance-based (orange), depending on the approach of detection. Bottom: Representation of all detected hUMCs (own Figure).

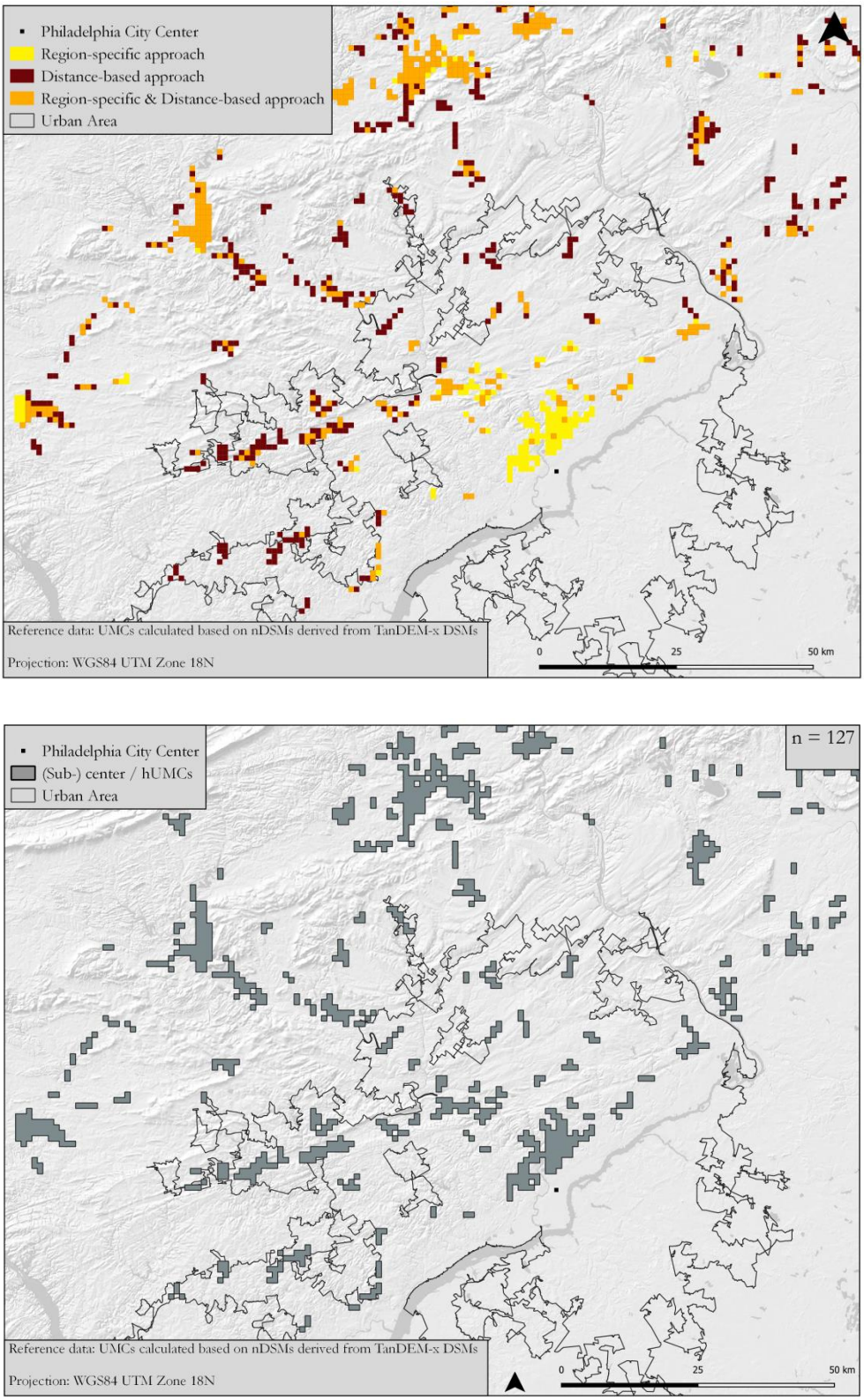

Appendix III 2: Detected (sub-)centers in Philadelphia. Top: Representation of the hUMCs (high urban mass concentrations) assigned to the classes region-specific (yellow), distance-based (red) and region-specific & distance-based (orange), depending on the approach of detection. Bottom: Representation of all detected hUMCs. Due to errors in the raw data, only half of the investigation area could be processed (own Figure).

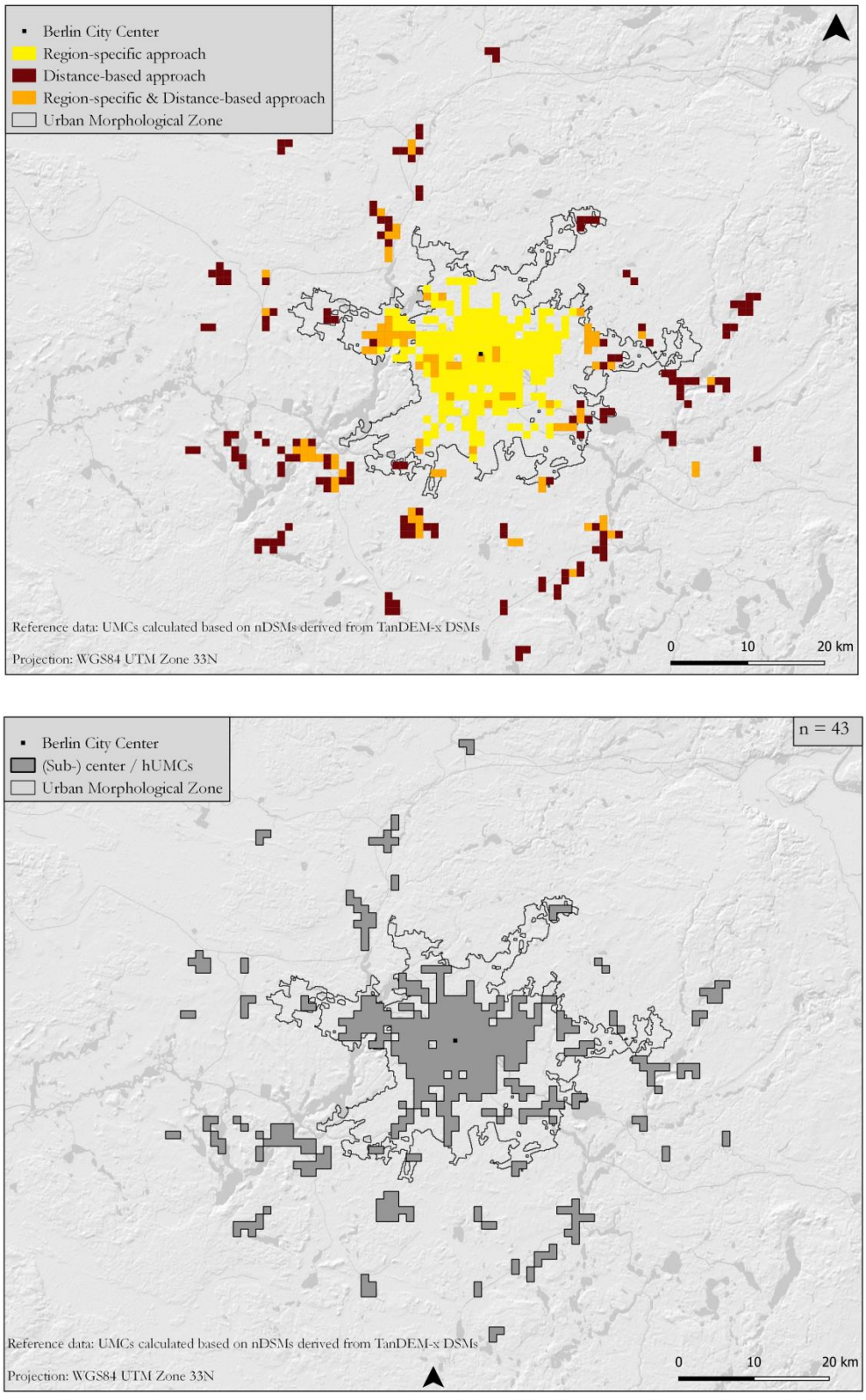

Appendix III 3: Detected (sub-)centers in Berlin. Top: Representation of the hUMCs (high urban mass concentrations) assigned to the classes region-specific (yellow), distance-based (red) and region-specific & distance-based (orange), depending on the approach of detection. Bottom: Representation of all detected hUMCs (own Figure).

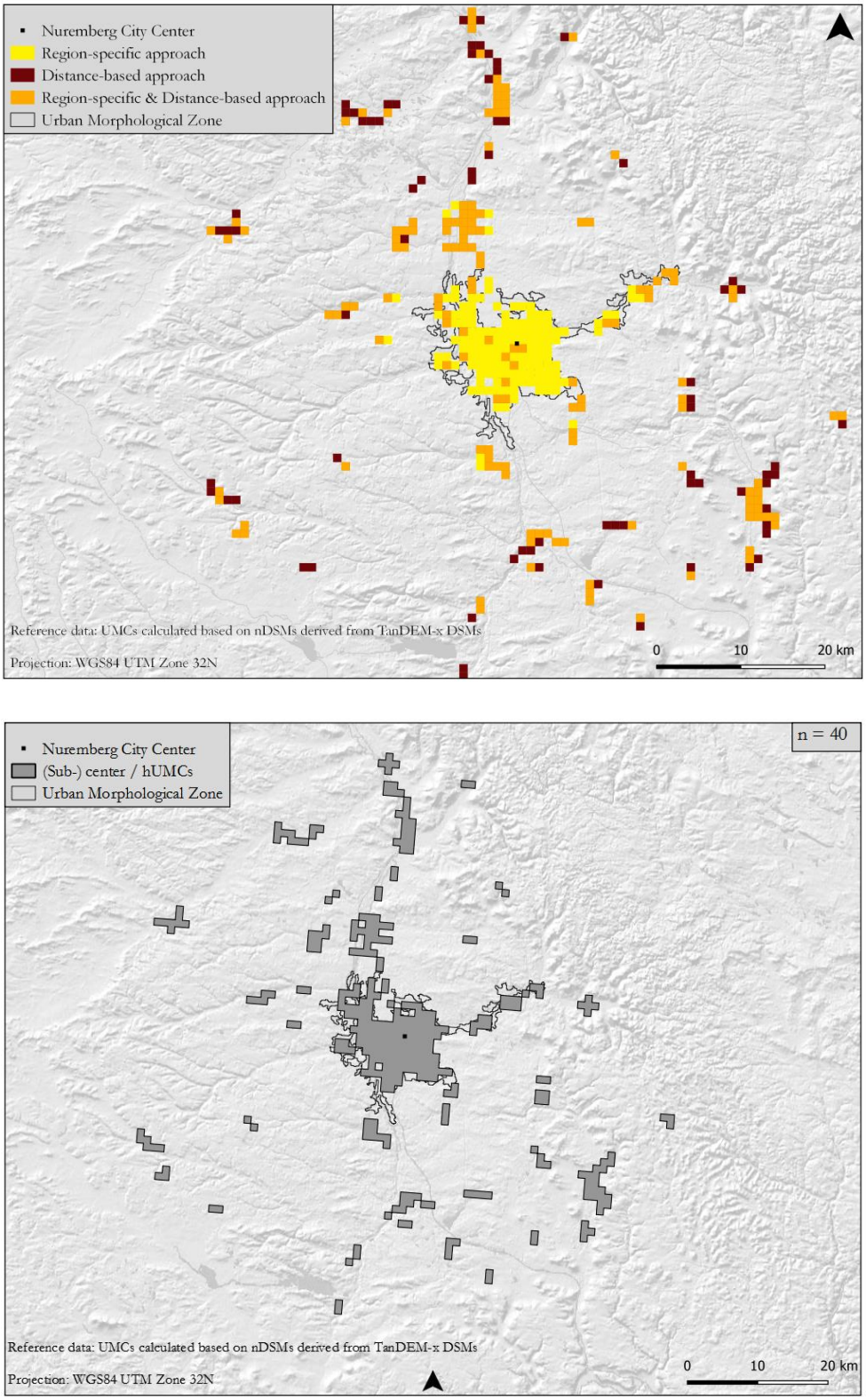

Appendix III 4: Detected (sub-)centers in Nuremberg. Top: Representation of the hUMCs (high urban mass concentrations) assigned to the classes region-specific (yellow), distance-based (red) and region-specific & distance-based (orange), depending on the approach of detection. Bottom: Representation of all detected hUMCs (own Figure).

Appendix IV: Figures with reference to the Discussion

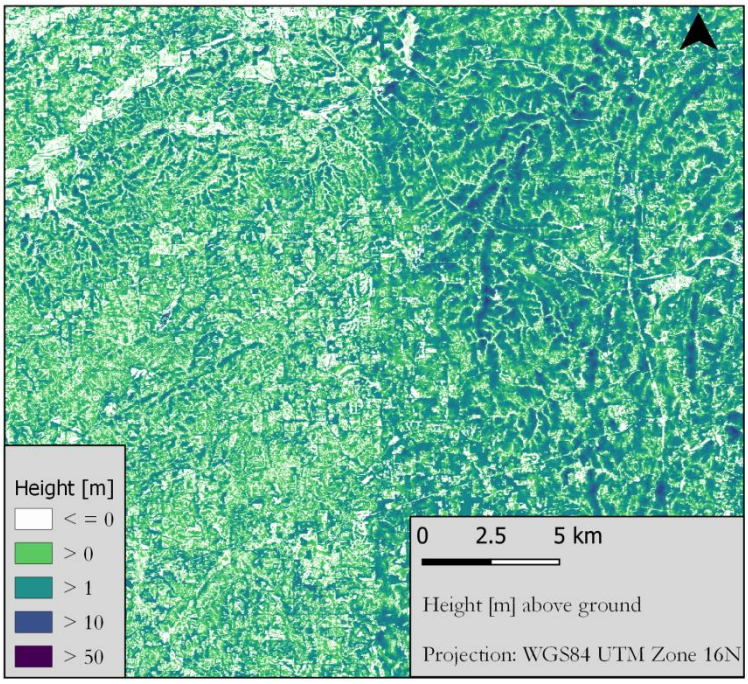

Appendix IV 1: Representation of the influence of the SE (structuring element) on the nDSM (normalized Digital Surface Model). Exemplarily shown for a small part of the area under investigation in Atlanta (own Figure).

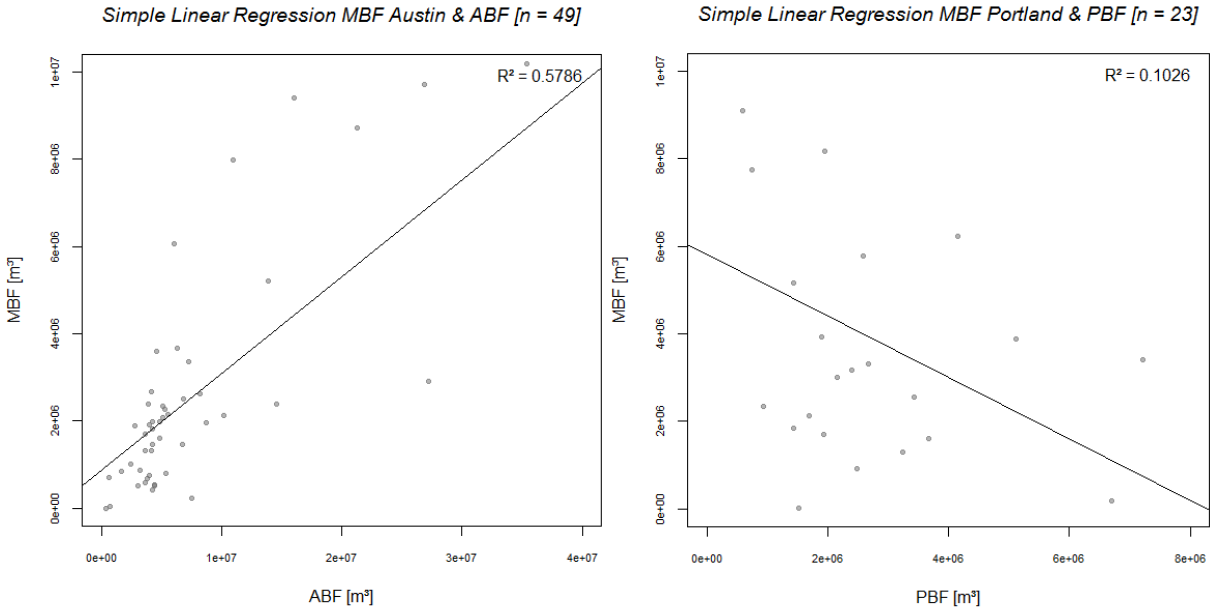

Appendix IV 2: Simple linear regression of a) the Microsoft Building Footprint of Austin and the Austin Building Footprint and b) the Microsoft Building Footprint of Portland and the Portland Building Footprint. The coefficient of correlation is in each case shown in the upper right corner (own Figure).

Eidesstattliche Erklärung

Ich versichere, dass ich die vorliegende Arbeit ohne fremde Hilfe und ohne Benutzung anderer als der angegebenen Quellen angefertigt habe, und dass die Arbeit in gleicher oder ähnlicher Form noch keiner anderen Prüfungsbehörde vorgelegen hat. Alle Ausführungen der Arbeit, die wörtlich oder sinngemäß übernommen wurden, sind als solche gekennzeichnet.

Kühnl, Marlene

München, 04.04.2019